High-precision Spectroscopy Using Rydberg Atoms

by

Kaitlin Rose Moore

A dissertation submitted in partial fulfillment
of the requirements for the degree of
Doctor of Philosophy
(Applied Physics)
in the University of Michigan
2017

Doctoral Committee:

Professor Georg A. Raithel, Chair
Professor Steven Cundiff
Associate Professor Hui Deng
Adjunct Professor Vladimir Malinovsky, Stevens Institute of Technology
Professor Duncan Steel

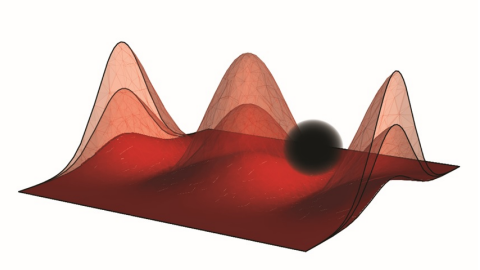

Illustration of Rydberg atoms in an

amplitude-modulated ponderomotive optical lattice.

Kaitlin R. Moore

kaimoore@umich.edu

ORCID iD: 0000-0003-4782-3525

For my wonderfully supportive family, especially my parents Susan and Tim, my brother Ben, and my husband Justin

ACKNOWLEDGEMENTS

I would first like to acknowledge my advisor, Georg Raithel, whose guidance has made this work possible. Georg has taught me an uncountable number of new skills in the course of performing cold-atom research. He possesses excellence both intellectually and technically and is ever willing to share his knowledge with his students. Georg has, at times, allowed me to take my own direction with a research topic or design idea, which has been invaluable to me in building confidence as a researcher. He has been cheerfully willing to spend as much time as is needed, even in the evenings and on weekends, to discuss a manuscript, review data, or even pipe-solder with me (and we have done a lot of pipe-soldering). Georg's amicable nature is a characteristic taken on by the research group he leads, making his group a pleasant and intellectually-stimulating environment in which to perform research.

Thank you to Professor Duncan Steel, Associate Professor Hui Deng, Professor Steven Cundiff, and Adjunct Professor Vladimir Malinovsky (from the Stevens Institute of Technology) for serving on my dissertation committee. I would especially like to thank Vlad for all the kind feedback and many collaborative Skype meetings over the past two years. I would also like to thank Stephanie Miller for proofreading this thesis and for her thoughtful feedback.

The other members of the Raithel lab whose work has overlapped with mine have all been a good-natured group, forever willing to share equipment and lend a hand with a project. In particular, I am grateful to Stephanie Miller, Nithiwadee 'Pound' Thaicharoen, Sarah Anderson, Andira Ramos, Jamie MacLennan, Robert

Powel, Yun-Jhih Chen, David Anderson, Andrew Schwarzkopf, Rachel Sapiro, Eric Paradis, Lu Ma, Michael Viray, and Stephen DiLorio. Sarah, thank you for all of the advice you shared with me when I first joined the Raithel group. The training I received from you early on gave me the best possible start on the 'cryoMOT' system (may it rest in peace). Stephanie, thank you for always providing a sounding board, sage advice, and a person to share inside jokes with throughout the years. Graduate school would not have been the same without you. Pound, your positive attitude is amazing, as is your technical proficiency, and you always provide the best pick-me-ups (and also make sure that I don't forget to eat!) I will always remember that we celebrated an eve-of-Christmas-eve in the lab together. Andira, Jamie, and Robert, it has been my pleasure to collaborate with each of you at different times over the years, and I look forward to seeing what you will accomplish! Andira, take care of the 'babies'.

I would like to thank my first research advisor, Aaron Leanhardt, for introducing me to AMO physics. Aaron allowed me to work in his lab for two years after I graduated from the University of Michigan (the first time), which provided me with invaluable lab skills, knowledge of AMO physics, and an insight into what graduate school would be like. I credit Aaron for offering the advice and support that helped me begin my graduate school career.

The members of the Society of Women in Physics, especially Jenna, Julia, Stephanie, and Veronica, have been an uplifting source of comradery, entertainment, and support throughout (and prior to) my years in graduate school. I will always remember our annual early mornings at Slauson, and that, despite classes, teaching, weddings, and research, we all still found time to come together to put on a conference! Jenna, Julia, and Stephanie, I will miss our early years when we were all a part of the Randall "Laborary" sub-basement crew.

Finally, the support and investment that I have received from my family began

long before I entered graduate school, and I certainly would not be where I am without their consistent encouragement and care. I hardly know where to begin to express my gratitude, especially to my parents Susan and Tim, my brother Ben, and my husband Justin. Thank you Mom and Dad for your unwavering love and support for me, including celebrating holidays with me via Skype while I was in the lab. Thank you Ben, for always engaging with my nerdiness now and when we were growing up (and for introducing me to my favorite Star Trek podcast, which has gotten me through many long nights of research). Finally, thank you Justin for buying me food, doing my laundry, celebrating New Year's Eve with me in the lab, and otherwise dealing with my research zeal with eternal patience and love. You have all enabled me to accomplish what I have, and it is to you that I dedicate this work.

TABLE OF CONTENTS

LIST OF FIGURES

Figure

LIST OF TABLES

Table

LIST OF APPENDICES

Appendix

ABSTRACT

High-precision spectroscopy using Rydberg atoms

by

Kaitlin R. Moore

Chair: Georg Raithel

Using cold atoms, I probe the energy-level intervals between Rydberg states to high spectroscopic precision. The focus of this work is to lay the groundwork for an updated, highly-controlled measurement of the Rydberg constant using circular-state Rydberg atoms, needed to resolve a recent conflict in proton-radius values that arose in 2010 (the so-called 'proton radius puzzle'). Toward this end, I have demonstrated a fundamentally-new mechanism with which to drive atomic (Rydberg-Rydberg) transitions, utilizing an inelastic (state-changing) ponderomotive interaction. Until now, the multipole-field interaction has been the sole mechanism on which spectroscopy of atomic transitions has been based. In this work, the state-changing ponderomotive interaction ('ponderomotive spectroscopy') is demonstrated by amplitude-modulating an optical standing wave at a transition resonance of a Rydberg atom. At the core of this new spectroscopic technique is the requirement that the light intensity must be modulated in space within the atomic volume, and in time at the desired atomic transition frequency. A Rydberg atom in a modulated optical lattice is very well-suited for a demonstration of this novel type of spectroscopy.

Magic-wavelength conditions of this interaction are also identified, as well as a

method to drive transitions at harmonics of the modulation. Both of these features of ponderomotive spectroscopy will be utilized to simultaneously trap and probe Rydberg atoms to perform the Rydberg constant measurement.

I also present a high-precision measurement of the quantum defect of a high-angular-momentum state of rubidium, the atomic species that will be used in the Rydberg constant measurement. The quantum defects of high-angular-momentum states are needed to determine the effect of the rubidium core polarizability on the Rydberg constant measurement, which is anticipated to be a leading uncertainty.

Finally, I present the background and design work for a measurement of the Rydberg constant specifically tailored to help resolve the proton radius puzzle, thereby completing the major preliminary work needed for the performance of that high-precision measurement.

CHAPTER I

Introduction

1.1 Background and motivation

Precision spectroscopy is a well-established, powerful tool in science for characterizing microscopic systems. Fields of science that use this tool range from precision metrology [1] (development of frequency standards [2] and high-precision sensing, such as gravitometry [3]) to trace analysis [4] and chemical sensing [5]. Characterizing and manipulating particles using light is also the foundation of modern fields such as quantum optics [6], quantum computing [7, 8], and quantum information processing [1, 9]. In order to push the boundaries of measurement science using spectroscopy, scientists must meet the present-day challenge of exploring microscopic systems in entirely novel ways or with ever-increasing precision. These are challenges I strive to meet throughout this dissertation.

Within the past decade, one exciting result within the precision-measurement community that has been said to "surprise" the physics world [10] has been the emergence of conflicting measurements of the proton radius [11–13], which has stimulated a flurry of experimental [14, 15] and theoretical [16–18] work. One possible cause for the conflict is an inaccurate Rydberg constant, the value responsible for relating atomic energy level intervals with spectral observations. My graduate work is centered around experimental efforts that lay the groundwork for a new, highly-controlled

measurement of the Rydberg constant tailored to resolve the proton radius question, with long-term plans to perform a future, advanced experiment in micro-gravity.

1.1.1 Thesis framework

This dissertation reports on three related topics of study that each perform precision spectroscopy using cold Rydberg atoms (atoms featuring a highly-excited electron). Together, these studies lay the groundwork for a future measurement of the Rydberg constant. Throughout, I focus on driving difficult-to-access transitions between Rydberg states either as proof-of-principle demonstrations of novel phenomena (Chapter III and Chapter IV) or for high-precision measurement (Chapter VII and Chapter VIII).

In the remainder of Chapter I, I review atomic theory that is relevant across multiple studies in this dissertation. Theory that is relevant to only a single study is reviewed in the corresponding chapter. In Chapter II, I describe the general schemes of preparing and detecting cold Rydberg atoms common to all my experiments. In Chapter III and Chapter IV, I outline a series of experiments I have performed to demonstrate for the first time the novel phenomenon of driving an atomic state transition using the ponderomotive interaction, via an amplitude-modulated ponderomotive optical lattice (called "ponderomotive spectroscopy"). This is a fundamentally-new state-changing atom-field interaction, possessing specific advantages over the atom-field interaction that has, until now, been traditionally used in spectroscopy. In Chapter V, I report the results of a theoretical study analyzing the effects of atomic center-of-mass motion in ponderomotive spectroscopy, using a semi-classical model. I demonstrate that the ponderomotive-spectroscopy selection rules are more flexible than theory based on stationary atoms would indicate. Overall, this work positions ponderomotive spectroscopy to be used to both trap and probe Rydberg atoms in the Rydberg constant measurement experiment.

Next, I shift focus and present my design and implementation of a new ultra-high vacuum-chamber system, as well as a subsequent precision-measurement experiment performed in this system using microwaves (Chapter VI and Chapter VII). In this experiment, I measure the quantum defect of a rubidium (Rb) Rydberg angular momentum state influenced solely by the core polarization interaction, with a precision one order of magnitude higher than the most recent measurement [19]. When uncertainty due to the ponderomotive trap is set aside, the core polarization quantum defect is predicted to be the most dominant systematic uncertainty in the proposed Rydberg constant measurement. Therefore, it is important to study this topic.

Finally, in Chapter VIII and Chapter IX, I present my design for the new ultra-high vacuum-chamber system for the Rydberg constant measurement and the future outlook of that project.

1.1.2 Rydberg atoms and precision spectroscopy

Rydberg atoms are well-suited for precision spectroscopy. In these atoms, the valence electron is far-removed from the positive ionic core of the atom, making the overall atom quite large (on the order of a micron). This property allows cold Rydberg atoms to be trapped and manipulated in unique ways. For example, Rydberg atoms may be trapped using the ponderomotive interaction (described in Section 1.4). This enables micron-sized Rydberg atoms to be trapped using optical standing-wave lattices (which also have a periodicity of about a micron), thereby keeping the Rydberg atoms isolated and localized, properties that are ideal for precision measurements. Additionally, as my graduate work has shown, the ponderomotive interaction may also be used to drive Rydberg-Rydberg transitions. Use of this interaction enables dipole selection rules to be entirely bypassed and thereby provides unprecedented spectroscopic access to the probed atomic species. I describe this phenomenon in Chapter III, Chapter IV, and Chapter V.

Another property of Rydberg atoms favorable for precision spectroscopy is that the energy intervals between Rydberg states are within the microwave/THz regime. Continued advances in microwave synthesizer technology have resulted in extremely accurate microwave outputs (a few parts in 10^{12}) when the internal crystal oscillator of a synthesizer is replaced by a commercially-available GPS-synchronized atomic clock. I exploit this microwave-synthesizer instrument precision in Chapter VII and Chapter VIII.

One other property of Rydberg atoms suitable for precision spectroscopy is that Rydberg atoms may be prepared in so-called "circular" states. These are states in which the electronic probability distribution of the valence electron forms a (node-line-free) torus around the ionic core of the atom, and the atom resembles that of a classical Bohr model. These circular states are insensitive to many issues that plague precision measurement spectroscopy (e.g. they are free from strong perturbations due to electric fields and effects from the nuclear and ionic-core overlap). These states are excellent candidates for a high-precision measurement of the Rydberg constant independent from effects of the proton size, as described in Section 1.2 and Chapter VIII.

1.2 Rydberg constant

The Rydberg constant is a value that relates the observed spectra of atomic lines with atomic energy levels [20]. First introduced in 1890 by Johannes Rydberg, the Rydberg constant R_∞ was initially empirically deduced from measurements of atomic spectral-line series. Rydberg deduced that the inverse-wavelength interval, $1/\lambda$, between two atomic states of principal quantum numbers n_i and n_f is expressed by

$$1/\lambda = R_\infty \left(\frac{1}{n_i^2} - \frac{1}{n_f^2} \right), \tag{1.1}$$

otherwise known as the Rydberg formula. Modern-day conventions typically rewrite

this expression in terms of frequency ($\nu = c/\lambda$) or energy ($W = h\nu$) intervals between atomic states, where c and h are the speed of light and Planck's constant, respectively.

In 1913, Niels Bohr used his model of the atom to define the Rydberg constant in terms of the charge (e) and mass (m_e) of the electron. Bohr modeled the atom classically as a valence electron orbiting a core with uniform circular motion, and he assumed quantized angular momentum [20], leading to the present-day definition of the Rydberg constant

$$R_\infty = \frac{1}{hc}\frac{k^2 Z^2 e^4 m_e}{2\hbar^2} = \frac{Z^2 e^4 m_e}{8\epsilon_0^2 h^3 c} = \frac{Z^2 \alpha^2 m_e c}{2\hbar}, \tag{1.2}$$

where $k = 1/(4\pi\epsilon_0)$ is the Coulomb constant (ϵ_0 is the vacuum electric permittivity), Z is the charge number of the atomic core (for hydrogen or alkali atoms, $Z = 1$), $\hbar$ is the reduced Planck's constant ($h/(2\pi)$), and α is the fine-structure constant.

Here, R_∞ indicates that it is assumed that the valence electron of the atom orbits around a core of infinite mass. In realistic systems, the finite mass of the core m_c means that the core is slightly displaced in response to the action of the electron (using Newton's third law). Then, the central force between the two bodies may be expressed as the product between the reduced mass μ and the center-of-mass motion, where $\mu = m_e m_c/(m_e + m_c)$. The reduced mass μ is an important correction to include in present-day precision measurements using the Rydberg constant [21]. This correction is introduced by replacing m_e in Equation 1.2 with μ. The correction is indicated via a new subscript for the Rydberg constant, typically indicating the atomic species used in the calculation of μ. For example, for Rb, it is common to write R_{Rb}.

1.2.1 Previous Rydberg-constant measurements

Over the years, Rydberg constant measurements have improved in precision. The most recent value of the Rydberg constant, as reported in CODATA 2014 [22], is

$R_\infty = 10973731.568508(65)\ \mathrm{m}^{-1}$, which has a low relative uncertainty of 5.9×10^{-12}. This value has been calculated via a least-squares regression comparing detailed theoretical predictions to experimental spectroscopic observations. The spectroscopic observations have been compiled from twenty-five various frequency intervals measured using hydrogen isotopes. The measurements took place between 1979 and 2013, with relative uncertainties improving over that time period from 2×10^{-5} to 4×10^{-15}, respectively. Each of these frequency-interval measurements either start or end in a low-lying $1S_{1/2}$ or $2S_{1/2}$ state, which are strongly affected by the overlap of the electron with the nucleus (detailed below).

On the other hand, a few spectroscopic efforts exist that do not appear in the CODATA compilation but have aimed to measure the Rydberg constant utilizing atomic states other than low-lying states of hydrogen. Three notable efforts include a 1993 proposal to measure the Rydberg constant with a relative uncertainty of $<10^{-10}$ using circular-state lithium atoms [23], a 2001 measurement performed as part of a doctoral dissertation that used millimeter-wave transitions between circular states of hydrogen to obtain a relative uncertainty of 2×10^{-11} [21], and a 2014 proposal to measure the Rydberg constant using transitions between Rydberg states in a single-electron ion [24]. All of these efforts have aimed to measure the Rydberg constant in a regime free from effects due to nuclear charge overlap, but the final results have either not yet been attained or else possess a relative uncertainty at least one order of magnitude higher than the currently-accepted Rydberg constant value.

1.2.2 Relation to the proton radius

The Rydberg constant has recently returned to the spotlight because of the proton radius puzzle introduced in Section 1.1.

The current CODATA 2014 value for the proton radius is 0.8751(61) fm [22]. This value has been compiled from results from electron-proton scattering experiments and

standard hydrogen spectroscopy. However, in 2010, a spectroscopic measurement of the Lamb shift of muonic hydrogen (an atom formed from a proton and a muon) first measured a significantly smaller proton radius [11], which was reproduced in 2013 with even lower uncertainty [12] and again re-adjusted in 2015 to be, at present, 0.84029(55) fm [22]. Overall, there is a discrepancy of about 5.7σ between the two values.

A portion of the quantum-electrodynamic (QED) contributions to the Lamb shift(s) of the energy intervals in a spectroscopic measurement depend on the root-mean square (rms) charge radius of the nucleus. In the case of standard hydrogen, this is the proton. Low-lying, especially S, states have a significant overlap of the electron wavefunction with the nucleus. If the electron is "inside" the nucleus, the overall charge it is exposed to is reduced, as is its binding energy [10]. This reduction in energy must be accounted for and is part of the QED theory that determines the Lamb shift for each state (along with self-energy and vacuum polarization terms, etc.). In standard hydrogen, this reduction in energy makes up 0.02% of the Lamb shift of the $1S$ state [10]. In muonic hydrogen on the other hand, the proton size has up to a 2% effect on the Lamb shift due to the tight orbit of the muon. In any hydrogen-like atom, as the electron overlap with the nucleus is reduced (i.e. the electron is excited to higher principal and angular-momentum quantum numbers), the portion of the Lamb shift that is dependent on the proton or nuclear radius goes to zero.

Because both the determination of the Rydberg constant and the proton rms charge radius are (at least in part) dependent on spectroscopic measurements of low-lying states of hydrogen, the least-squares regression that determines their values must consider both of these as simultaneous fit parameters. For example, it has been pointed out that including the muonic-hydrogen proton-radius value into the CODATA calculations would result in a Rydberg constant value that is shifted down by over five standard deviations from the currently-accepted value [22] (assuming the

correctness of QED).

Therefore, one way to resolve this proton radius puzzle is to perform a high-precision measurement of the Rydberg constant independent from nuclear-charge-radius effects, using precision spectroscopy of transitions between high-lying angular-momentum Rydberg states. I have designed the experiment that will enable such a measurement to be performed using circular-state Rydberg atoms, which will be described in Chapter VIII.

1.3 Atomic properties relevant to precision Rydberg spectroscopy

The studies presented in this thesis utilize the alkali species Rb to generate Rydberg atoms, which then take the form of a single valence electron orbiting an ionic core that possesses a net charge of +1.

With a highly-excited valence electron, the Rydberg atom is large, and the Rydberg electron is loosely bound to the ionic core of the atom. Because of this, Rydberg atoms are sensitive to external stimuli, such as electric and magnetic fields. These are summarized below in Subsection 1.3.2 and Subsection 1.3.3.

In Subsection 1.3.4, I describe the origin of the energy-level shift that arises from the interaction of an atom with the oscillatory electric field of light. This energy-level shift is a commonly-considered phenomenon in precision spectroscopy.

Finally, in Subsection 1.3.5, I describe a property common to alkali atoms and important for Rydberg spectroscopy: the quantum defect. The quantum defect represents a correction to the Rydberg formula (Equation 1.1) to account for the departure of the structure of alkali atoms from the structure of hydrogen (on which the Rydberg formula is based).

1.3.1 Scaling laws

In this section, select properties of Rydberg atoms are derived and summarized. Because the probability distribution function of the Rydberg electron is mostly far-removed from the ionic core of the atom, it is conventional and adequate to use the classical Bohr model to extract general scaling laws for Rydberg atoms [20].

First, I describe the scaling of the orbital radius of the Rydberg electron. Using classical mechanics, Newton's expression for the force on an object moving with uniform circular motion can be equated with the Coulomb force, obtaining $m_e v^2/r = kZe^2/r^2$, where v is the tangential velocity of the orbiting electron and r is the orbital radius. Using the Bohr condition for quantization of angular momentum $m_e v r = n\hbar$, the solution for r is

$$r \approx \frac{n^2\hbar^2}{m_e k Z e^2} = n^2 a_0, \tag{1.3}$$

where $a_0 = 5.29 \times 10^{-11}$ m is the Bohr radius. Here, r scales as n^2. In other words, a ground-state hydrogen atom with radius $r \approx a_0$ increases in size up to $r \approx 100a_0$ at just $n = 10$.

This property of the atoms means that the valence electron is also weakly bound to the core, with a Coulomb potential energy

$$V_c = -k\frac{Ze^2}{r} \approx -k\frac{Ze^2}{n^2 a_0}. \tag{1.4}$$

Because of this weak binding, external fields have a stronger effect on Rydberg atoms than on ground-state atoms, leading to forms of detection not available to ground-state atoms. For example, Rydberg atoms may be ionized with electric fields that are experimentally practical to produce (up to around 1 kV/cm). This can be seen by examining the sensitivity of the Rydberg atom to DC electric fields, otherwise known as the Stark effect. Here, I specifically examine the classical ionization limit.

This limit is derived by assuming a static electric field $E\hat{z}$ ($\hat{z}$ is a unit vector in the z-direction), with a potential $V_E = eEz$. Then, along the z-direction,

$$V = V_c + V_E = -k\frac{Ze^2}{|z|} + eEz. \tag{1.5}$$

The local maximum of this potential is found at $z = -\sqrt{kZe/E}$ with an energy of $V = -2e\sqrt{EkZe}$ [20]. The classical ionization-field threshold is derived to be

$$E_{\text{class}} = \frac{(hcR_\infty)^2}{4kZe^3n^4}. \tag{1.6}$$

Using a similar classical two-body model, the Kepler frequency of a circular-state Rydberg atom is likewise derived to be

$$\nu = \frac{1}{2\pi}\frac{1}{n^3}\sqrt{k\frac{Ze^2}{m_e a_0^3}}. \tag{1.7}$$

A few other relevant scaling laws are listed in Table 1.1 and derived in Reference [20].

Table 1.1: Rydberg-atom scaling laws.

Orbital radius	n^2
State energy	n^{-2}
Radiative lifetime (high-l)	n^5
Kepler frequency	n^{-3}
Separation between adjacent Rydberg levels	n^{-3}
Ionization electric field	n^{-4}

1.3.2 DC Stark shift and parabolic coordinates

The effect of external electric fields on electronic energy levels (DC Stark shift) is a critical consideration in precision spectroscopy with Rydberg atoms. The DC Stark shift arises when an external electric field is applied to an atom and perturbs the Coulomb potential (Equation 1.4). Moving from classical into quantum mechanics

and using degenerate perturbation theory for a hydrogen atom with states $|n, l, m\rangle$ (n is the principal quantum number, l is the angular-momentum quantum number, and m is the magnetic quantum number), it can be shown that the first-order correction to the Coulombic energy levels due to an external electric field E applied along z (the classical equivalent of which is displayed in Equation 1.5) is dependent on matrix elements $eE\langle n'l'm'|r\cos\theta|nlm\rangle$. As such, neglecting dipole-coupling to other n manifolds (for small fields), it can be seen that n and m remain good descriptors as the field lifts the degeneracy. However, the matrix elements indicate that in the presence of a field, spherical symmetry is broken along the z-direction, and l is no longer a good quantum number.

Instead, Stark states are the good quantum states in this system. As such, parabolic coordinates are used to describe Stark states, rather than spherical coordinates, because parabolic coordinates yield a separable wavefunction in the presence of an electric field. Parabolic coordinates refer to a set of coordinates that describes a position in space using surfaces that are rotationally symmetric around the z-axis, including two paraboloids sharing foci at the origin. As such, parabolic quantum numbers are quantum numbers for which n and m both represent the same idea as in spherical coordinates; principal and azimuthal (magnetic) quantum numbers, respectively. However, because the two paraboloids used to describe the set of spatial coordinates may have differing curvatures, two quantum numbers n_1 and n_2 are required to replace the single angular momentum quantum number l found in spherically-symmetric systems. The model is not overparametrized because of the relation $n = n_1 + n_2 + |m| + 1$. Using perturbation theory on zero-field wavefunctions expressed in these parabolic coordinates, the first- and second-order Stark shift V_S (in a.u.) is given by the sum [20]

$$V_S = \frac{3En}{2}(n_1 - n_2) - \frac{E^2}{16}n^4[17n^2 - 3(n_1 - n_2)^2 - 9m^2 + 19]. \tag{1.8}$$

This expression is noteworthy because in circular Rydberg states, which have $n_1 = n_2 = 0$, the first-order Stark shift is zero. In Chapter VIII, this characteristic of circular states (and nearby Stark states that also possess $n_1 = n_2$) is exploited in the proposed design for the precision measurement of the Rydberg constant.

1.3.3 Zeeman shift and other magnetic-field interactions

For a precision measurement, as well as for cold-atom preparation, atom interaction with magnetic fields must also be considered. Atoms with the quantization axis along an external magnetic field $B\hat{z}$ display energy splittings in their spectra due to magnetic sublevels, well-known as the first-order Zeeman effect V_Z. In the regime in which the energy shift due to the field is much less than the fine-structure interval of the atomic system (which goes as $1/n^3$), the quantum number j representing total angular momentum remains a "good" quantum number [25], and

$$V_Z = \mu_B g_j B m_j. \tag{1.9}$$

Here, $\mu_B = e\hbar/2m$ is the Bohr magneton, g_j is the Landé-g factor, and m_j is a magnetic sublevel $|m_j| = 0, 1, \ldots j$.

In a regime in which the energy shift due to B is much greater than the fine-structure interval of the atomic system (called the strong-field, or Paschen-Back, regime), total angular momentum is no longer conserved, and l, s, m_l, m_s become good quantum numbers. Among my studies, spectroscopy in the Paschen-Back regime is relevant in Chapter VIII.

Additionally, the first-order Zeeman effect is exploited in the cooling and trapping mechanism common to all experiments, presented in Chapter II.

1.3.4 Light shift

In this section, I will outline the origins of the light shift (known as the AC Stark shift) and describe its impact on the precision spectroscopy performed in this dissertation.

In spectroscopy, interaction with a light field typically causes a shift in the energy level of an atom. Light fields include those used for trapping as well as those used for probing an atomic transition. One of the optical forces used for trapping, the dipole force, is a direct consequence of the light shift and will be explained further in Subsection 1.4.2.

In a two-level atom (the "Rabi" problem [26]), the oscillating electric field of a light beam leads to dipole coupling between the two states $|i\rangle$ and $|f\rangle$. The coupling is described by a term known as the Rabi frequency, which describes the rate at which the probability of being in the excited state oscillates between its maximum and minimum value. Such a probability is determined not only by the amplitude of the light field, but also the detuning of the field frequency from the resonance energy $\hbar\omega_0$ between states.

For example, if a monochromatic light field with angular frequency ω_L is assumed to be propagating in the z-direction, $\mathbf{E}(\mathbf{r},t) = E_0\hat{\varepsilon}\cos(kz - \omega_L t)$, then the detuning is defined as $\delta = \omega_L - \omega_0$. In the interaction picture, the effective Rabi frequency is $\chi \equiv \sqrt{\chi_0^2 + \delta^2}$, where $\chi_0 \equiv -eE_0\hat{\varepsilon}\cdot\langle f|\hat{r}|i\rangle/\hbar$ is the Rabi frequency on-resonance. Using a rotating-frame transformation to eliminate rapidly oscillating frequencies in the problem [26], state $|i\rangle$ is assigned an unperturbed energy $W_i = 0$, state $|f\rangle$ is assigned an unperturbed energy $W_f = -\hbar\delta$, and the coupling between states is described by $\chi\hbar/2$ (note these have been corrected from an error in Reference [26]). This problem can easily be written as a 2×2 matrix and diagonalized to find the "true" eigenenergies of the two states. The results yield

$$W_{f,i} = \frac{\hbar}{2}(-\delta \mp \chi). \tag{1.10}$$

For $\chi_0 \ll |\delta|$, the shifts on the unperturbed level energies can be approximated from Equation 1.10 in a more familiar (first-order) form as

$$V_{L;f,i} = \mp\frac{\hbar\chi_0^2}{4\delta} = -\frac{\alpha E_0^2}{4}. \tag{1.11}$$

Here, $\alpha \equiv -\langle f|r|i\rangle^2/(\delta\hbar)$ is otherwise called the dynamic polarizability [27] of the state and becomes an important parameter in optical trapping. For example, a ground-state atom (state $|i\rangle$) in a far-red-detuned light trap would have a positive polarizability and experience a negative energy shift. Trapping involving this mechanism will be discussed further in Section 1.4. Overall, these light shifts must be minimized and accounted for in any precision measurement, unless a special condition is found such that the overall light shift is zero for a specific transition (or, in some cases, even for individual levels). This special condition is commonly referred to as a "magic-wavelength" condition. I explore this concept further in Chapter IV.

1.3.5 Quantum defects

The work in this dissertation is performed with the alkali metal Rb. In order to compare spectroscopy results from alkali atoms with models developed for hydrogen, the difference in structure between the two species must be evaluated. The primary difference is the presence of a finite-sized core in alkali atoms, which for Rb consists of the nucleus and thirty-six electrons. This difference is called the "quantum defect".

The quantum defect arises from two separate interactions between the valence electron and the finite-sized core: a penetration interaction and a polarization interaction. In the penetration interaction, the valence electron penetrates into the core. As a result, the electron is less shielded from the nuclear charge and exposed to a

deeper Coulomb potential (Equation 1.4). This deeper Coulomb potential depresses the energy of the hydrogenic state of the electron.

In the polarization interaction, on the other hand, the valence electron induces multipole moments in the ionic core [20]. The polarization interaction between the Rydberg electron and the ionic core likewise depresses the energy of the alkali Rydberg state.

To calculate the expected frequency of a transition between alkali-atom states, the non-integer quantum-defect values are determined empirically and inserted into the hydrogenic Rydberg formula as a correction on the principal quantum number. This correction yields

$$\nu_{n_i,n_f} = R_{\mathrm{Rb}} c \left(\frac{1}{(n_i - \delta_i)^2} - \frac{1}{(n_f - \delta_f)^2} \right) \tag{1.12}$$

as an expression for the transition frequency interval ν_{n_i,n_f} between two states n_i and n_f. Here, δ_i and δ_f represent the corresponding quantum defects. To obtain good fits to spectroscopic data, δ must itself often be expanded as a nonlinear function of n. This function is called the Ritz expansion $\delta = \delta_0 + \frac{\delta_2}{(n-\delta_0)^2} + \ldots$, which is then inserted for δ in Equation 1.12.

The exact shape of the probability distribution function of the Rydberg electron determines the amount of overlap of the electron with the core, especially for low-angular-momentum states. Therefore, δ is naturally a function of the quantum numbers l and j, along with n. In Rb, for angular momentum states above $l = 3$ (the F state), the contribution to δ from core penetration approaches zero, and the quantum defect may be expressed solely in terms of the polarization interaction [19, 28]. In this case, it is common to expand the interaction in terms of contributions from different multipole moments induced in the core, i.e.

$$\delta_{nl} n^{-3} = \frac{\alpha_d}{2} \langle 1/r^4 \rangle_{nl} + \frac{\alpha_q}{2} \langle 1/r^6 \rangle_{nl} + \ldots . \tag{1.13}$$

Here, $\delta_{nl}n^{-3}$ is an energy shift (in a.u.), α_d and α_q represent the dipolar and quadrupolar static core polarizabilities, respectively, and the $\langle 1/r^x \rangle_{nl}$ terms are spatial powers averaged over state nl [29].

These concepts will be especially important in Chapter VII and Chapter VIII.

1.4 Rydberg atoms in a ponderomotive potential

As mentioned in Section 1.1, Rydberg atoms trapped in ponderomotive potentials are isolated and well-localized, which is ideal for precision measurements [30, 31], as well as quantum computing applications [1, 7–9]. A portion of my dissertation work expands on previous work that uses a fixed, standing-wave optical field to confine Rydberg atoms using the ponderomotive potential. My work describes the results of dynamically modulating the amplitude of that ponderomotive optical standing wave to demonstrate a novel inelastic atom-light interaction that will be used in a future Rydberg constant measurement.

1.4.1 Previous work trapping Rydberg atoms

Previous work on Rydberg-atom trapping has been done with static fields (electric [32–34] and magnetic [35, 36]) and optical fields [27, 37–41]. For example, electric-field trapping makes use of the large dipole moment of the Rydberg atom, which arises due to the large separation of the valence electron from the ionic core. In terms of quantized states, the dipole moment arises from the first-order Stark effect (the first term in Equation 1.8). Three-dimensional trapping using electric fields is accomplished via electrodes generating a quadrupole field configuration with a field-amplitude minimum at the center [34]. Rydberg atoms with a positive Stark shift are attracted to the locations of these field minima. Likewise, magnetic-field trapping of Rydberg atoms has also been demonstrated, using strong fields to interact with the Rydberg electron [35].

However, while electric- and magnetic-field traps are one way to confine cold Rydberg atoms, they are not conducive to precision spectroscopy of the energy intervals between unperturbed Rydberg states, the primary interest of this thesis, because they rely on large nonzero fields (which may also be nonzero at field minima) to function as intended. These nonzero fields can induce shifts in the transition frequency between two Rydberg states, which is undesirable when performing a precision measurement of the unperturbed (unshifted) frequency.

Instead, for multiple experiments presented in this dissertation, I rely on an optical Rydberg-atom trap, generated from an optical standing wave. While optical traps may also induce unwanted light shifts in a precision measurement, one technique to mitigate such shifts is to use the magic-wavelength conditions that I demonstrate in Chapter IV.

Below I describe Rydberg trapping using optical standing waves.

1.4.2 Fixed ponderomotive traps

Optical-lattice traps for both Rydberg-state atoms and ground-state atoms utilize the intensity gradients in optical standing waves to generate a trapping potential for the atoms. However, the atom-field interaction that leads to this potential is fundamentally different for the two atomic states.

For ground-state atoms, the restoring force is a consequence of the interaction of the electric dipole moment of the atomic state with the electric field $\mathbf{E}(\mathbf{r}, t)$ of the light, otherwise called the dipole force. As discussed in Subsection 1.3.4, this interaction results in a light shift, or added potential, on an unperturbed atomic level, via Equation 1.11. In a lattice trap, composed of a standing-wave beam, this potential is a function of position. The negative gradient of this potential produces a force on the atom. For example, in Rb, a trap formed from a Nd:YAG (1064 nm) laser is far-red-detuned from the transition between the ground state and the next excited

state. As a result, the ground-state polarizability is positive, and ground-state atoms are attracted to lattice intensity maxima. Furthermore, these lattices depend on the polarization of the light.

Rydberg atoms, on the other hand, are trapped via the ponderomotive force, a conservative force arising from the ponderomotive potential, which is fundamentally different from the dipole interaction that traps ground-state atoms. In a Rydberg atom, the loosely-bound valence electron can be considered quasi-free. The ponderomotive potential arises as a consequence of the quivering motion of the quasi-free electron in the applied light field. The quivering motion of this electron occurs at the frequency of the light wave (10^{15} Hz), which is so quick compared to other frequencies of the atom (e.g. the Kepler frequency due to the electronic state and the center-of-mass motion) that it may be adiabatically separated from these. For example, the Kepler frequency of a $n=50$ circular state (Equation 1.7) is $\sim 5 \times 10^{10}$ Hz. Likewise, in lattices in the experiments presented in this dissertation, the maximum energy of the center-of-mass motion of the atom is on the order of 10 kHz. The adiabatic separation of these motional scales is called the Born-Oppenheimer approximation. After performing this separation, the problem simplifies to the interaction between the light-wave and a free electron, the solution of which is given by Volkov states [42] with eigenenergies $V = (\hbar^2 k_e^2)/(2m_e) + V_P$, where the free-electron ponderomotive potential V_P is given by

$$V_P = \frac{e^2 E_0^2}{4 m_e \omega_L^2}. \tag{1.14}$$

Here, $\hbar k_e$ is the momentum of the electron.

The increase in energy due to the quiver motion of the electron acts as a correction on top of other energy values in the system. For example, as long as the energy levels of the Rydberg atom are well-separated (which can be achieved by applying appropriate electric and magnetic fields to induce state separation [37] or in states with a large

quantum defect, e.g., nS-states), the quiver energy acts as a perturbation on top of the Coulombic states and any shifts thereon due to DC electric and magnetic fields. In other words, the effect of the optical field on the Rydberg atom can be accounted for by adding the position-dependent ponderomotive potential V_P onto the Rydberg electron's Hamiltonian. If the effect of the optical field cannot be treated as a perturbation, then state-mixing is induced [37].

Because the ponderomotive potential is position-dependent (with coordinate $\mathbf{R}$) and the Rydberg electronic wavefunction has a large spatial extent with respect to the lattice period, the true potential $V_{\text{ad}}(\mathbf{R})$ experienced by the electron is given by the spatial average of V_P over the electronic wavefunction $\psi(\mathbf{r})$ [39],

$$V_{\text{ad}}(\mathbf{R}) = \int d^3r V_P(\mathbf{r}+\mathbf{R})|\psi(\mathbf{r})|^2. \tag{1.15}$$

Therefore, for nondegenerate Rydberg states in a (one-dimensional) ponderomotive lattice, the energy shift of the unperturbed states depends on both the center-of-mass location $\mathbf{R}$ of the atom and the shape of its wavefunction. These concepts will be relevant in Chapter III, Chapter IV, and Chapter V.

As can be deduced from Equation 1.15, $V_{\text{ad}} \to V_P$ as the size of the atom gets smaller relative to the lattice period. This means that for low n, the overall shift on the unperturbed Rydberg energy levels is positive, and the effective polarizability α_P (derived by comparing with Equation 1.11) is negative. This is the opposite from that of ground-state atoms, indicating that low-n Rydberg atoms are attracted to locations of intensity minima in a ponderomotive lattice. This necessitates the use of a special phase-shifting technique to achieve efficient trapping [27] (see Section 3.1). However, it has been shown (and re-affirmed in this work) that at specific values of n, the polarizability of the trap-induced shift is reversed and Rydberg atoms are attracted to locations of intensity maxima. The oscillatory nature of α_P as a function of n means that there are specific principal quantum numbers for which the trap-

induced shifts are approximately equal. This property is exploited to demonstrate magic-wavelength conditions for these traps in Chapter IV.

1.4.3 Amplitude-modulated ponderomotive traps

In Appendix A, I do a more detailed derivation starting from the atom-field Hamiltonian to demonstrate that the introduction of dynamic amplitude modulation (a blinking lattice) is expected to energetically couple Rydberg states and induce an electronic transition. This phenomenon was first predicted theoretically in 2007 [43]. My work demonstrates the phenomenon for the first time experimentally (Chapter III and Chapter IV) and also builds on the theory (Chapter V). I demonstrate the phenomenon by dynamically modulating the amplitude of a ponderomotive optical lattice trap containing Rydberg atoms. I observe spectral peaks when the modulation is performed at a microwave frequency resonant with electronic energy intervals of the Rydberg atoms. Because this spectroscopy is fundamentally different from the usual dipole-field interaction, it allows the observation of strongly-dipole-forbidden transitions.

Amplitude-modulated ponderomotive traps can be used to simultaneously trap and perform precision spectroscopy on Rydberg atoms, with the promise of applications far beyond those proposed in Chapter III. For instance, by addressing only those Rydberg atoms in the trap, other nearby Rydberg atoms are filtered out of the interaction with a spatial resolution not attainable even using focused microwaves. Such a scheme could be used, for example, to streamline quantum gate operations (described at the end of Chapter III).

Furthermore, using this technique, the extremely-high precision of a microwave synthesizer (< 1 Hz) is retained, similar to Raman spectroscopy. "Ponderomotive" spectroscopy, however, is fundamentally different from Raman spectroscopy, as explained in Chapter III. One advantage of this difference is that in ponderomotive spec-

troscopy, transitions are driven as a first-order perturbation. Raman spectroscopy, on the other hand, is the result of a second-order process, thereby potentially requiring higher optical power to drive a transition. This makes Raman spectroscopy a comparatively less ideal scheme for precision spectroscopy due to potentially greater light shifts. For this reason, an amplitude-modulated ponderomotive lattice will be employed to perform the precision measurement of the Rydberg constant (see Chapter VIII).

Finally, it is important to note that these amplitude-modulated lattices are not restricted to Rydberg atoms. Available light-modulation technology has made the proof-of-principle demonstration using Rydberg atoms the logical choice. However, other particle-standing-wave configurations can be envisioned if the particle satisfies the following two primary conditions of ponderomotive spectroscopy: (1) the electronic distribution extends over a nonlinear intensity gradient of the standing wave and (2) the standing-wave amplitude is dynamically modulated at a frequency resonant with an energy interval of the particle. We have only scratched the surface!

CHAPTER II

Experimental Techniques

The work in this dissertation lays the groundwork for a precision measurement of the Rydberg constant using cold, circular-state Rydberg atoms trapped in an optical lattice. In this chapter, I describe the experimental processes common throughout the dissertation to prepare and detect samples of cold Rydberg atoms. I first review the basics of ground-state atom trapping in magneto-optical traps (MOTs). I then describe the lasers used to optically excite Rydberg atoms from these cold-atom samples, which vary between experiments. The last item I discuss in this chapter is the procedure used to detect Rydberg atoms. The remaining step, probing Rydberg-Rydberg transitions, is unique to each experiment and so will be described in the corresponding experiment chapters.

2.1 Laser cooling and trapping of ground-state atoms

In 1997, Steven Chu, Claude Cohen-Tannoudji, and Bill Phillips were jointly awarded the Nobel Prize in Physics for developing methods to cool and trap atoms using laser light. Laser-cooling methods have opened up a new world of study in quantum physics and have become a workhorse of the field. In an experiment, atoms are often produced as vapors at room temperature (300 K) or hotter with the velocities of the constituent atoms following a Maxwell-Boltzmann distribution. By slowing

("cooling") atoms down to temperatures a fraction of a degree above absolute zero and confining them, scientists gain advantages over using hot atoms. For example, scientists may probe a cold atomic sample at high density to observe exotic states of matter, such as Bose-Einstein condensates. Relevant to my work, scientists may also probe cold-atom samples for long interaction times and in the absence of motional effects (such as Doppler broadening), leading to narrow spectral lines ideal for precision measurements.

Two main types of interactions are used in ground-state laser cooling and trapping: the scattering force and the dipole force. The dipole force has already been introduced in Section 1.4 as a conservative force resulting from a light gradient interacting with an atomic dipole. On the other hand, the scattering force is a dissipative force that uses radiation pressure to alter the momentum of atoms. Atoms absorb light with momentum in a specific direction and re-radiate light in a random direction via spontaneous emission, thereby receiving a net change in momentum in the direction of the absorbed light over many cycles. Atoms are cooled using light that is red-detuned with respect to an atomic resonance between a lower (i.e. ground) state and an upper state, called the cooling transition. To avoid population loss or the need for multiple lasers, it is ideal to use a cooling transition that is as close to a closed two-level system as possible (see Subsection 2.1.1).

Adapted from Reference [26], the Doppler-cooling scattering force on an atom (due to absorption of light followed by spontaneous emission) can be expressed as

$$\mathbf{F} = \frac{\hbar \mathbf{k} \gamma}{2} \frac{I/I_s}{1 + I/I_s + (2\delta/\gamma)^2}, \tag{2.1}$$

where $\mathbf{k}$ is the wavevector of the interacting laser, γ is the spontaneous decay rate of the upper state in the cooling transition, I is the intensity of the laser at the location of the atoms, I_s is the saturation intensity of the cooling transition, and δ is the laser

detuning from the transition resonance in the atomic rest frame ($\delta = \delta_0 - \mathbf{k}\cdot\mathbf{v}$, where δ_0 is the detuning for a zero-velocity atom and $\mathbf{v}$ is the center-of-mass velocity of the atom). This expression can be used to estimate, for example, the fraction of atoms with an initially-hot velocity distribution that will be slowed down within some trap capture region.

2.1.1 Magneto-optical traps

One type of trap that uses the scattering force to both cool and confine atoms is the magneto-optical trap (MOT).

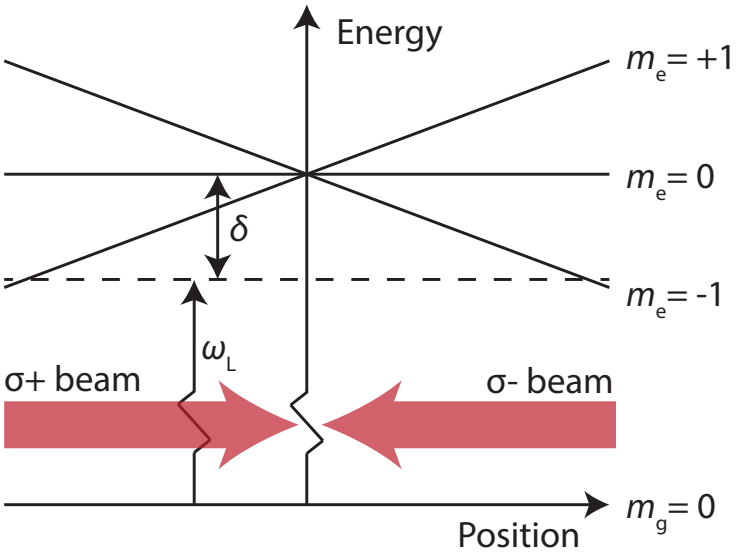

Figure 2.1: **MOT energy level diagram for a $J_g = 0 \rightarrow J_e = 1$ transition.** The position-dependent gradient of the magnetic field causes different excited-state magnetic sublevels (m_e) to shift into resonance with red-detuned lasers (red arrows). The σ^+/σ^- polarizations of the laser beams are indicated. Atoms are driven toward the trap center via the net scattering force.

To generate a strong MOT, both magnetic-field gradients and laser properties must be controlled. For the ^{85}Rb isotope used in each of my experiments, the cycling (cooling) transition occurs via the $|5S_{1/2}\rangle \rightarrow |5P_{3/2}\rangle$ line at 780 nm. In order to separate degenerate m_F sublevels as a function of position, a magnetic-field gradient is applied to split the magnetic sublevels via the Zeeman effect (Equation 1.9), as shown

in Figure 2.1 for the simplified case of a $J_g = 0 \rightarrow J_e = 1$ transition. Typical gradients are 10-20 Gauss/cm at the center of the trap region in a three-dimensional quadrupole configuration [26]. This configuration is achieved by a pair of anti-Helmholtz coils. Anti-Helmholtz coils refer to a magnetic coil pair in which the coils have opposing current directions. The ideal separation for a pair of coils is a separation on the order of the radius of the coils, which yields a maximum gradient [44].

In a pair of ideally-separated coils, the field gradient scales as $I_0 N/R^2$, where I_0 is the current, N is the number of coil windings, and R is the average coil radius, which is fixed by the geometry of the vacuum system. Power consumption per coil is given by $P = 2\pi R\rho N I_0^2/A$, where A is the cross-sectional area of an individual wire in the coil [44] and ρ is the resistivity of the magnet wire at the appropriate temperature.

To design the anti-Helmholtz coils presented in Chapter VI and Chapter VIII, I utilized numerical simulations of the Biot-Savart law to determine coil parameters. My design process is as follows: (1) Restrict R and coil cross-section ($\approx NAf$, where $f \approx 0.6 - 0.8$ is a packing fraction) to available geometry (for example, the project described in Chapter VIII uses elliptical coils); (2) While keeping the field gradient fixed and restricting A to commercially-available diameters of magnet wire, find values of both P and N that limit P to values below a desired heat-dissipation level, and limit N based on available coil-winding techniques (typically $N \approx 50$).

In addition to the magnetic-field gradient, it is important to set properties of the cooling laser(s) to optimal values. These properties include polarization, detuning and optical power. As shown in Figure 2.1, cooling and trapping occur simultaneously in a one-dimensional MOT via atom interaction with two counterpropagating, circularly-polarized laser beams. Using circularly-polarized light, atoms are optically pumped to a $|F=3, m_F=\pm 3\rangle \rightarrow |F'=4, m_{F'}=\pm 4\rangle$ transition with a saturation intensity I_s of 1.7 mW/cm^2 [45]. In order to provide a dissipative effect, as well as a restoring force, the light is further red-detuned from the cycling resonance by a few MHz. As shown in

Figure 2.1, due to this red-detuning and circular polarization, the atom preferentially absorbs light propagating in a direction opposite to its displacement from the trap center, thereby receiving a net force directed toward the center of the trap. This scheme can be extended to three dimensions by including additional beams.

Depending on the linewidth and detuning of the laser, a small number of atoms is also excited to a $F' = 3$ state and spontaneously decays to the $F = 2$ hyperfine ground state. Consequently, a second laser frequency is required to be on-resonant with the $|F = 2\rangle \rightarrow |F' = 3\rangle$ transition to "repump" this population back into the cooling transition. The difference between Rb cycling- and repumper-transition frequencies is about 2.9 GHz (plus any red-detuning).

The light sources used for these cycling and repumper beams are homebuilt external cavity diode lasers (ECDLs) (output about 30 mW) [46]. These lasers rely on a single-mode laser diode situated in a tunable external cavity formed from a reflection grating and the back facet of the diode. The angle θ between the reflection grating normal and the incident light beam is tuned via a piezo-electronic actuator such that the laser receives feedback for stimulated emission at a specified wavelength λ, given by $d\sin(\theta) = m\lambda$ for integer m. Here, d is the grating spacing (usually on the order of 1000/mm for these lasers at $\theta \sim 45°$). Feedback for laser-wavelength stabilization is generated by locking to a ^{85}Rb hyperfine spectral line in a saturated-absorption spectroscopy (SAS) set-up [47] and generating an error signal using proportional-integral-differential (PID) electronics.

Light from the cycling laser is amplified in a tapered amplifier to several hundred mW. Both lasers are sent through single-pass acoustic-optic modulators (AOMs) before being coupled into fibers that lead to the experiments. Sending the light through the AOMs allows the option to switch off the MOT light briefly during an experimental cycle to avoid light shifts in a precision measurement.

2.2 Experimental sequence

2.2.1 Optical excitation

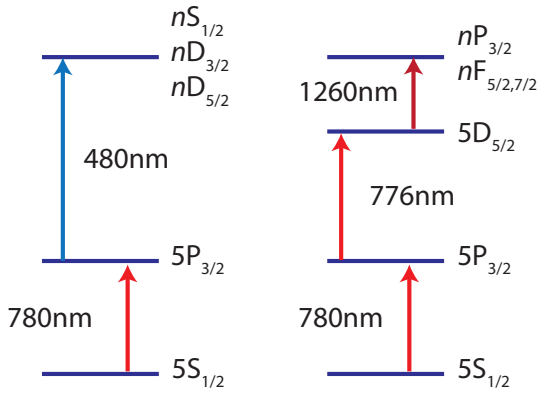

Figure 2.2: **Excitation schemes for Rydberg preparation.** Two different excitation schemes used in these experiments to prepare Rydberg atoms in levels with opposite parities, requiring different laser configurations.

In Chapter III and Chapter IV, ground-state atoms are transferred to Rydberg states via the two-photon excitation sequence $|5S_{1/2}\rangle \rightarrow |5P_{3/2}\rangle \rightarrow |\text{Rydberg}\rangle$, as illustrated in Figure 2.2. In Chapter VII and Chapter VIII, ground-state atoms are transferred to Rydberg states via the three-photon excitation sequence $|5S_{1/2}\rangle \rightarrow |5P_{3/2}\rangle \rightarrow |5D_{5/2}\rangle \rightarrow |\text{Rydberg}\rangle$. The former case allows even-parity Rydberg states to be prepared, while the latter case allows odd-parity Rydberg states to be prepared.

In both excitation schemes, the laser light for the $|5S\rangle \rightarrow |5P\rangle$ transition has a wavelength of 780 nm. The source of this laser is a homebuilt ECDL, and the set-up is similar to the MOT lasers.

The source of the laser light for the $|5P\rangle \rightarrow |\text{Rydberg}\rangle$ transition, on the other hand, is a Toptica SHG laser system, which outputs $\approx$ 200 mW of 480 nm light. The 480 nm light is generated via a seed laser at 960 nm, which is amplified and coupled into a bow-tie cavity housing a nonlinear crystal. Frequency doubling is achieved via second harmonic generation. The laser wavelength is stabilized via feedback on the seed laser. To generate the feedback loop, a portion of 960 nm light is

sent into a homebuilt pressure-tunable Fabry-Pérot etalon [48]. The etalon consists of a temperature-stabilized confocal cavity within a sealed enclosure. The enclosure volume may be compressed or expanded via an attached bellows, by way of a computer-controlled stepper motor. As the enclosure volume is systematically varied, so too is the pressure of the gas medium (typically air) within the cavity. This, in turn, linearly varies the $n_I - 1$ (n_I is index of refraction) response of the gas medium, increasing or decreasing the central frequencies of the cavity transmission peaks as a function of stepper motor location. As the peaks shift adiabatically with respect to the kHz-scale laser-locking electronics, the laser (which is locked to one of the cavity peaks) is correspondingly tuned.

For the $|5S_{1/2}\rangle \rightarrow |5P_{3/2}\rangle \rightarrow |5D_{5/2}\rangle \rightarrow |\text{Rydberg}\rangle$ scheme, the source for the $|5P_{3/2}\rangle \rightarrow |5D_{5/2}\rangle$ 776 nm laser light is a homebuilt ECDL, for which I led the construction and set-up. Stabilization of the wavelength is achieved by locking the ECDL to the $|5P_{3/2}, F = 2\rangle \rightarrow |5D_{5/2}, F' = 3, 4, 5\rangle$ transition via a modified SAS scheme [49] that uses a portion of the light that drives the on-resonant $|5S_{1/2}\rangle \rightarrow |5P_{3/2}\rangle$ lower transition to prepare $5P_{3/2}$ states in a Rb vapor cell. In the modified SAS spectrum, I am only able to resolve shoulders due to hyperfine splitting in the $5D_{5/2}$ state (expected to be $<$10 MHz). I peak-lock to the dominant $F'=5$ peak, expecting some off-resonant excitation due to the other hyperfine lines. Peak-locking refers to the practice of sending the spectral line through a lock-in amplifier to generate an error signal. Applying a small frequency modulation (much less than the width of the spectral line), multiplying the resulting signal by a TTL pulse synchronized with the frequency modulation, and time-integrating the product yields an error signal with a voltage that goes through zero at the peak of the spectral line.

Finally, the source for the $|5D_{5/2}\rangle \rightarrow |\text{Rydberg}\rangle$ laser light is another homebuilt ECDL, lasing around 1260 nm, for which I led the construction and set-up. This laser is tuned to achieve single-photon resonance with a $|5D_{5/2}\rangle \rightarrow$ —Rydberg P or $F\rangle$ tran-

sition. In Table 2.1, I list confirmed $|5D_{5/2}\rangle \rightarrow |\text{Rydberg}\rangle$ resonances that have been observed during the course of my experiments using the 1260 nm laser. For reference, the ionization limit for this excitation channel is at 1251-1252 nm. I record these (vacuum) wavelengths λ_{exp} from a Burleigh WA-1000 wavemeter, internally calibrated to a helium-neon ($\lambda = 633$ nm) laser. I assign Rydberg levels to these resonances by matching against values from literature references (λ_{ref}). Values for Rydberg $nF_{7/2}$ levels are from Reference [50]. Values for Rydberg $nP_{3/2}$ levels are from Reference [51]. Since the nF fine-structure is unresolveable on the scale of my experiments, I assign $nF_{5/2}$ and $nF_{7/2}$ to the same values. I also assign resonances to the nG fine-structure peaks, for which the anticipated separation from the corresponding nF levels has been verified via microwave spectroscopy (see Chapter VII). Finally, note that $nP_{1/2}$ is not accessible in the three-photon excitation scheme presented above due to dipole selection rules.

λ_{exp}	λ_{ref}[50, 51]	Assigned Rydberg level
1275.401-403	1275.399	$30P_{3/2}$
1264.436-437	1264.435	$40P_{3/2}$
1264.023-024	1264.025	$38F_{5/2,7/2}$
1264.016-017		$38G_{7/2,9/2}$
1263.407-409	1263.410	$39F_{5/2,7/2}$
1263.399-401		$39G_{7/2,9/2}$
1262.837-846	1262.841	$40F_{5/2,7/2}$
1262.831-839		$40G_{7/2,9/2}$
1262.311-314	1262.313	$41F_{5/2,7/2}$
1262.305-309		$41G_{7/2,9/2}$
1261.821	1261.823	$42F_{5/2,7/2}$
1261.646	1261.649	$45P_{3/2}$
1261.367-370	1261.368	$43F_{5/2,7/2}$
1261.363		$43G_{7/2,9/2}$
1258.144-152	1258.145	$53F_{5/2,7/2}$
1256.629-633	1256.630	$61F_{5/2,7/2}$

Table 2.1: Measured $5D_{5/2} \rightarrow$Rydberg resonances.

Similar to the 480 nm laser, this 1260 nm laser is stabilized by providing feedback on the diffraction grating to lock to a transmission peak from a pressure-tuned Fabry-

Pérot cavity on which I likewise led construction and set-up, based on the same design used for the 480 nm laser. Explicitly, it is a confocal cavity housed in a sealed enclosure, temperature-stabilized to 300.0 K. The relation between the fractional change in frequency $\delta\nu/\nu$ and the fractional change in enclosure length $\delta l/l$ as the laser is tuned by the stepper motor is given by the formula $\delta\nu/\nu = (n_I - 1)/n_{\mathrm{I}}(\delta l/l)$ [48], where n_{I} is the index of refraction of the gas medium in the cavity/enclosure. With an air medium, this cavity had a free spectral range (FSR) of 375 MHz (FSR=$c/(4n_{\mathrm{I}}l)$), with a calibration of 9.55 kHz/step (frequency translation per stepper motor step), measured using the known spacing of RF sidebands introduced onto an atomic resonance. Subsequent to that measurement, I introduced difluoroethane, R152a (trade name: HFC-152a) into the cavity to increase its index of refraction. As given in Reference [52], HFC-152a has $n_{\mathrm{I}} = 1.0083$ for a wavelength of $\lambda = 545$ nm, temperature of 313.8 K, and at standard pressure, compared to air at $n_{\mathrm{I}} = 1.00029$ at STP. Therefore, a mixture of HFC-152a and air is expected to increase n_{I} within the cavity. By increasing n_{I}, the frequency translation per step is increased to 12.9 kHz/step, as measured by a second calibration. This indicates that 1-10% of the cavity medium is HFC-152a. The full scan range of this Fabry-Pérot cavity is about 2 GHz.

Lastly, in each experiment, I minimize unwanted interactions with light fields during Rydberg-Rydberg transition measurements by timing the excitation sequence such that the excitation light turns off after preparation of the atoms in the initial Rydberg state. This is achieved, similar to the MOT light, by passing the excitation laser beams through separate AOMs and pulsing the RF power applied to the AOMs. The first-order light from the AOMs in either a single-pass (1260 nm laser) or a double-pass (780 nm and 776 nm) configuration is selected and coupled through optical fibers to the experiment.

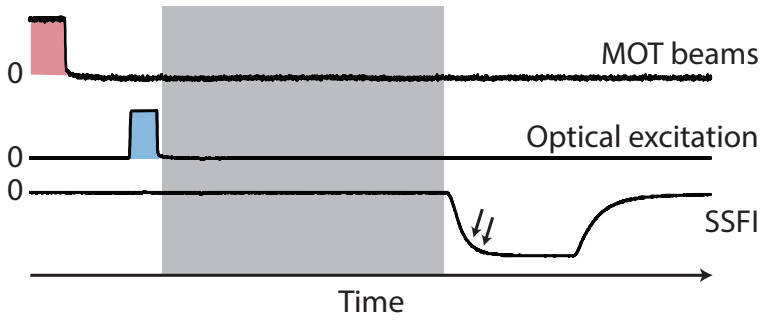

Figure 2.3: **Sample timing diagram.** MOT beams (light red) are turned off prior to Rydberg preparation via optical excitation (blue), which is typically on the order of 1 μs. The interaction time (gray) is typically on the order of 10 μs (although this varies among experiments). The SSFI ramp allows Rydberg states to be detected at unique locations along the ramp (indicated by arrows).

2.2.2 Rydberg detection

As explained in Chapter I, a common detection method for Rydberg atoms is to use a DC electric field (hundreds of V/cm) to ionize the loosely-bound electron. The resulting charge then indicates the presence of a Rydberg atom. As indicated in Equation 1.6, the field at which a Rydberg atom (adiabatically) ionizes is uniquely state-dependent. Therefore, in a method called state-dependent field ionization (SSFI) [20], the ionization electric field is adiabatically ramped from zero to some value as a function of time. The accumulation of charges at unique locations along the ramp indicates the presence of Rydberg states. I used this method for detection in each of the experiments presented in this dissertation.

Ionized electrons are detected on an in-vacuum micro-channel plate (MCP) detector. A MCP is a charge-multiplier device that produces a voltage pulse for a single detected charge, with about a 30% detection efficiency. Voltage pulses are counted with a pulse counter, which integrates counts within a pre-set time window during an experimental cycle. Further discussion of this procedure can be found in Reference [53].

The timing diagram in Figure 2.3 shows a portion of a typical experimental cycle,

including trapping, optical preparation of Rydberg states, the interaction time, and the detection sequence.

2.3 Electric-field zeroing

Because the studies performed in this dissertation deal with precision spectroscopy using Rydberg atoms, I must be especially careful to cancel electric fields prior to a measurement, to prevent inaccuracies in the measurement results. To do so, I use the Stark spectroscopy procedure introduced in Chapter I. "Field zeros" are determined by varying the field direction in question while holding the other directions static until a minimum shift of a measured transition is observed. In this way, I generate a Stark map, a plot of the central frequency location of a transition versus electric-field strength. Because the shifts of low-angular-momentum states of Rb go as $-\alpha E^2/2$ (where α is, in this case, the static polarizability and E is the electric field), the field zero is determined by fitting the Stark map to a parabola. The uncertainty in the parabolic fit, along with the instrumental uncertainty of the voltage sources, determines the resulting uncertainty in the residual DC Stark shift contributed by the direction in question. For example, in Chapter VII, I describe an experiment in which the energy-shift uncertainty due to the fields has been determined by adding in quadrature the uncertainties due to the instrument noise and parabolic fit parameters, as well as their covariances. An example of a Stark map is likewise provided in Chapter VII.

CHAPTER III

Lattice-Modulation Spectroscopy of Rydberg-Rydberg Transitions

The model describing atomic spectroscopy includes the multipole-field interaction, which leads to established spectroscopic selection rules, and an interaction that is quadratic in the field, which is not often employed. However, spectroscopy using the quadratic (ponderomotive) interaction promises two significant advantages over spectroscopy using the multipole-field interaction: flexible transition rules and vastly improved spatial addressability of the quantum system. In this chapter, I demonstrate ponderomotive spectroscopy by using optical-lattice-trapped Rydberg atoms, pulsating the lattice light, and driving a microwave atomic transition that would otherwise be forbidden by established spectroscopic selection rules. This ability to measure frequencies of previously inaccessible transitions makes possible improved determinations of atomic characteristics and constants underlying physics, including the future measurement of the Rydberg constant outlined in Chapter VIII. The spatial resolution of ponderomotive spectroscopy is orders of magnitude better than the transition frequency would suggest, promising single-site addressability in dense particle arrays for quantum computing applications [1, 9].

To experimentally demonstrate an atomic transition via the ponderomotive interaction, Rydberg atoms trapped in an amplitude-modulated standing-wave optical

lattice are used. Rydberg-atom optical lattices are an ideal tool for this demonstration because the atoms' electronic probability distributions can extend over several wells of the optical lattice [27], and Rydberg-Rydberg transitions are in the microwave regime [20], a regime in which light-modulation technology exists.

To further illuminate the use of such an amplitude-modulated optical lattice for a demonstration of ponderomotive spectroscopy, I briefly examine the physics underlying the interaction between the Rydberg atom and the lattice light. The interaction between the atom and a light field is described by the interaction Hamiltonian [54]

$$V_{\text{int}} = \frac{1}{2m_e}\left(2\left|e\right|\mathbf{A}\cdot\mathbf{p} + e^2\mathbf{A}\cdot\mathbf{A}\right), \tag{3.1}$$

where $\mathbf{p}$ is the Rydberg electron's momentum operator and $\mathbf{A}$ the vector potential of the light (the laser electric field $\mathbf{E} = -\frac{\partial}{\partial t}\mathbf{A}$). The $\mathbf{A}\cdot\mathbf{p}$ term describes most types of atom-field interactions that are commonly engaged in spectroscopy [54]. These are classified as E1, M1, E2... multipole transitions, which follow well-established spectroscopic selection rules [29]. For reference, E1 (M1) denotes an electric (magnetic) dipole transition, E2 denotes an electric quadrupole transition, etc. Typically, the dipole-field term dominates the total atom-field interaction and leads to the electric-dipole selection rules for atomic transitions. For example, in the case of direct application of microwave radiation to Rydberg atoms, the electric-dipole (E1) selection rules apply (in first-order perturbation theory). In contrast, the quadratic $\mathbf{A}\cdot\mathbf{A}$ (ponderomotive) term allows transitions far beyond these selection rules to be driven, as theoretically demonstrated by the Raithel group in earlier work [43], by providing a substantial spatial variation of the field intensity within the volume of the atom and by modulating the laser intensity in time at the transition frequency between the coupled states. This method to drive atomic transitions is particularly effective in an amplitude-modulated optical lattice, because the lattice is spatially modulated with

a period that is on the same scale as the Rydberg-atom diameter.

In this chapter, I report a successful demonstration of this fundamentally-new method spectroscopy. ^{85}Rb atoms are trapped in a one-dimensional standing-wave optical lattice, formed by counter-propagating 1064-nm laser beams. The $|58S_{1/2}\rangle \rightarrow |59S_{1/2}\rangle$ transition is driven by sinusoidally modulating the lattice intensity at the resonant transition frequency, found to be 38.76861(1) GHz. The $|58S_{1/2}\rangle \rightarrow |59S_{1/2}\rangle$ transition has been chosen because it is forbidden as a first-order electric-dipole (E1) transition, because its E2 coupling (due to the $\mathbf{A} \cdot \mathbf{p}$ term) is negligible, and because for this transition a large spatial coupling (due to the $\mathbf{A} \cdot \mathbf{A}$ term) is expected in the amplitude-modulated lattice [43].

First, I describe the experimental set-up, along with the trapping and atom-field interaction methods unique to this project. After, I present results demonstrating an atomic transition driven via the $\mathbf{A} \cdot \mathbf{A}$ term of the Hamiltonian for the first time.

3.1 Description of the experimental set-up

Figure 3.1 shows a schematic of the experimental set-up. A continuous-wave (c.w.) 1064-nm laser beam is split in a Mach-Zehnder interferometer (left) into a low-power and a high-power beam. The low-power beam is sinusoidally modulated via an electro-optic fiber modulator driven by a tunable microwave-frequency voltage signal. This amplitude-modulated low-power beam is coherently re-combined with the unmodulated high-power beam at the exit of the interferometer. In the atom-field interaction region (right), the standing-wave optical lattice is formed by retro-reflecting the lattice beam. Cold ^{85}Rb Rydberg atoms are trapped with center-of-mass positions near intensity minima of the lattice [27].

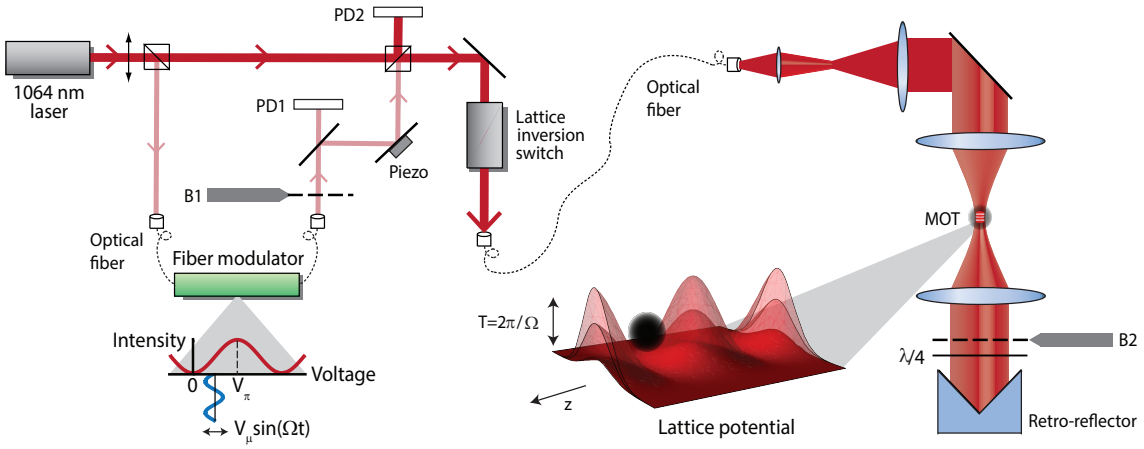

Figure 3.1: **Experimental set-up.** A Mach-Zehnder interferometer (left) combines two 1064-nm c.w. beams. One beam is amplitude-modulated at frequency Ω by a fiber-based electro-optic modulator ('Fiber modulator'), the operating point of which is set using photo-detector 'PD1'. Using photo-detector 'PD2' and a piezo-electric transducer ('Piezo'), the interferometer is locked such that the beams add up in phase. Rydberg atoms are laser-excited and optically trapped by lattice inversion. The optical lattice (right) is formed by retro-reflecting and focusing the 1064-nm laser beam into the magneto-optical trap ('MOT'). The lattice potential is amplitude-modulated with period T. Beam blocks ('B1','B2') are used for signal interpretation.

3.1.1 Preparation of cold Rydberg atoms in an optical lattice

Initially, ^{85}Rb atoms are cooled to a temperature of about 150 μK in a magneto-optical trap (MOT). A one-dimensional, 1064-nm optical lattice is applied to the MOT region. The optical lattice is formed by focusing an incident laser beam into the MOT region, retro-reflecting the beam, and re-focusing it. The incident beam interferes with the return beam and forms a standing wave. Pointing stability is greatly improved by using a retro-reflector rather than a plane mirror. See Figure 3.1 for an illustration of the set-up. The intensity ratio between the modulated and unmodulated portions of the incident lattice beam is about 1:100. The lattice has 880 mW of incident power at the MOT region with an 11-μm beam waist radius, and 490 mW of return power with an approximately 37-μm beam waist radius, as discussed in Appendix A. Both the MOT magnetic field and the lattice light remain on throughout a data scan, while the MOT light is turned off during Rydberg-atom

preparation and probing.

The Rydberg state is prepared via a two-stage excitation $|5S_{1/2}\rangle \rightarrow |5P_{3/2}\rangle \rightarrow |58S_{1/2}\rangle$ using 780-nm and 480-nm lasers, detuned from the intermediate $5P_{3/2}$ level by ≈ 1 GHz. Immediately after Rydberg-atom excitation, the lattice is inverted using an electro-optic component, required to efficiently trap Rydberg atoms at intensity minima [27]. The Rydberg atoms are trapped in the optical field using the ponderomotive interaction described in Chapter I. Finally, during a data scan, the Rydberg atom preparation laser wavelength is tuned so as to produce Rydberg atoms in the optical lattice at an average of 0.5 Rydberg atoms per experimental cycle. This ensures a negligible probability of atom-atom interactions.

3.1.2 Zeroing the fields

The electric field is zeroed prior to a series of data runs by performing Stark spectroscopy of the $58D_{3/2}$ and $58D_{5/2}$ fine-structure levels, while scanning the potentials applied to a set of electric-field compensation electrodes, as outlined in Chapter II. The residual field is less than 60 mV cm^{-1}. The MOT magnetic field, which is on during the experiment, does not cause Zeeman shifts of the $|58S_{1/2}\rangle \rightarrow |59S_{1/2}\rangle$ transition.

3.1.3 Lattice modulation

While $58S_{1/2}$ Rydberg atoms are trapped in optical lattice wells, the amplitude of the lattice is modulated at the expected $|58S_{1/2}\rangle \rightarrow |59S_{1/2}\rangle$ transition frequency. The electro-optic modulator used to perform the modulation is a fiber-coupled, polarization-maintaining, z-cut lithium niobate modulator, tunable from DC to 40 GHz. The modulator has an input optical power limit of 200 mW, which is, in the present experiment, insufficient for Rydberg-atom trapping. In a Mach-Zehnder-type interferometric set-up, the 1064-nm laser is split into a high-power (3.9 W),

unmodulated beam and a low-power (190 mW), amplitude-modulated beam, which is passed through the fiber modulator. The two beams are coherently re-combined at the exit beam-splitter of the Mach-Zehnder interferometer. The re-combined beam incident at the MOT region has approximately 1 W of average power, which is sufficient for Rydberg-atom trapping.

The fiber modulator has two voltage inputs, one for the microwave voltage signal and another for a DC bias voltage. The intensity transmitted through the fiber modulator depends on the values of these voltage inputs (see Appendix A). For most of the work presented in this chapter, the amplitude of the microwave signal is set to $V_\mu = V_\pi/2$, which yields maximal intensity modulation when the DC bias voltage is set at an inflection point of the modulator transmission curve (as illustrated in Figure 3.1). Due to thermal drifts in the fiber modulator, the DC bias voltage must be actively regulated to maintain this operating point. The lock circuit utilizes a photo-detector ('PD1' in Figure 3.1) and a PID regulator.

Due to drifts in the optical path length difference between the arms of the Mach-Zehnder interferometer, the path length of one of the interferometer arms must be actively regulated to maintain a fixed phase difference at the recombination beam-splitter. This phase difference is locked so that the intensity sent to the experiment is at a maximum (by maintaining an intensity minimum at the unused output of the recombination beam-splitter). The lock circuit utilizes a photo-detector ('PD2' in Figure 3.1), a mirror mounted on a piezo-electric transducer ('Piezo' in Figure 3.1), and a PID regulator.

In order to initialize certain experimental parameters (such as atom-field interaction time), an estimate of the expected Rabi frequency must be made. The full Rabi frequency expression is derived in Appendix A. Here, I provide an outline of the results. Due to the coherent mixing of the low-power, modulated lattice beam with the high-power, unmodulated beam, the time-averaged lattice depth is large enough that

most atoms remain trapped in the lattice while the $|58S_{1/2}\rangle \rightarrow |59S_{1/2}\rangle$ transition is probed. The coherent mixing of the two beams is additionally beneficial because it enhances the modulation in the atom-field interaction region, resulting in a much larger $|58S_{1/2}\rangle \rightarrow |59S_{1/2}\rangle$ coupling than would be possible with the weak modulated beam alone. The Rabi frequency for a transition $|n,l,m\rangle \rightarrow |n',l',m'\rangle$ between two Rydberg states that are resonantly coupled by the amplitude-modulated lattice is

$$\chi \approx \sqrt{\varepsilon}\frac{e^2}{\hbar m_e c\epsilon_0 \omega_L^2}\, I_{0\,\mathrm{inc}}^{\mathrm{dyn}}\, \mathrm{J}_1\left(\frac{\pi V_\mu}{V_\pi}\right)\left[1+\sqrt{\frac{2\, I_{0\,\mathrm{inc}}^{\mathrm{fixed}}}{I_{0\,\mathrm{inc}}^{\mathrm{dyn}}}}\right] D_{n,l,m}^{n',l',m'}, \tag{3.2}$$

where V_μ is the amplitude of the microwave voltage signal that drives the fiber modulator, V_π is the voltage difference between the minimum and maximum intensity transmission through the modulator (a fixed modulator property), ε is the intensity ratio at the atom location between the return and incident beams forming the lattice, ω_L is the angular frequency of the optical-lattice light, and $I_{0\,\mathrm{inc}}^{\mathrm{dyn}}$ and $I_{0\,\mathrm{inc}}^{\mathrm{fixed}}$ are the incident intensities of the dynamic (modulated) and fixed (unmodulated) lattice beams at the atom location, respectively. The transition matrix element $D_{nlm}^{n'l'm'}$ (unitless) has been derived in previous work [43] and is 0.215 for the $|58S_{1/2}\rangle \rightarrow |59S_{1/2}\rangle$ transition for an atom located at a minimum in the lattice. This value is large compared with those of other possible transitions due to a favorable ratio between atom size and lattice period (which is on the order of one). The detailed derivation of Equation 3.2 given in Appendix A includes values for the parameters listed above, yielding a typical Rabi frequency estimate on the order of 100 kHz. The in-phase addition of the fields corresponding to intensities $I_{0\,\mathrm{inc}}^{\mathrm{dyn}}$ and $I_{0\,\mathrm{inc}}^{\mathrm{fixed}}$, using the Mach-Zehnder beam combination set-up, leads to the enhancement term in square brackets in Equation 3.2. In the experiment, the Rabi frequency is enhanced by a factor of ≈ 20, which aids significantly in observing the transition. While in the experiment presented here the enhancement afforded by the interferometric set-up is critical for a successful

demonstration, in future implementations different laser wavelengths, advances in modulation technology, sub-Doppler and evaporative cooling techniques or the use of separate trapping and modulation beams could make the complex interferometric set-up nonessential in order to utilize this form of spectroscopy.

3.1.4 Detection

As detailed in Chapter II, the spectral line is detected through state-selective field ionization (SSFI), in which Rydberg atoms are ionized by a ramped electric field. Freed electrons are detected by a micro-channel plate, and detections on the micro-channel plate are registered by a pulse counter. Counting gates are synchronized with the field ionization ramp to enable state-selective detection of the $58S_{1/2}$ and $59S_{1/2}$ Rydberg levels.

During a data scan, the microwave frequency of the amplitude-modulation is stepped across the expected $|58S_{1/2}\rangle \rightarrow |59S_{1/2}\rangle$ resonance frequency. At each microwave frequency step, the pulse counter registers counts for 200 experimental cycles. Average counts per cycle are recorded before advancing to the next frequency step. The interferometer lock status is queried before and after each set of 200 experimental cycles. If either query indicates an unlocked interferometer, the data for that frequency step is omitted and re-taken.

At intensity minima or maxima, the intensity modulation of the lattice results (via the $\mathbf{A}\cdot\mathbf{A}$ term) in a time-periodic atom-field interaction with a leading quadratic dependence on position, needed to couple states with an angular momentum change $\Delta l = 0, 2$ in first order. The proper combination of temporal and spatial intensity modulation is essential for utilizing the $\mathbf{A}\cdot\mathbf{A}$ term to realize the type of spectroscopy introduced in this chapter.

3.2 Results

3.2.1 Spectroscopic signal

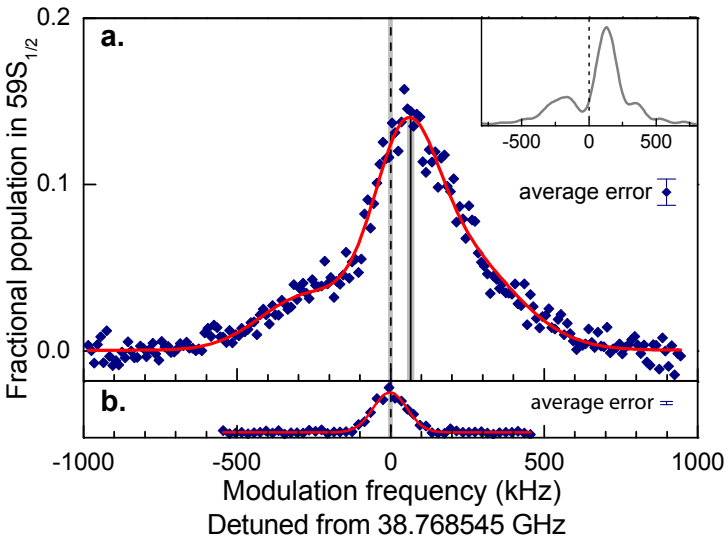

Figure 3.2: **The $|58S_{1/2}\rangle \rightarrow |59S_{1/2}\rangle$ transition driven via amplitude modulation of an optical lattice.** The fraction of atoms in $59S_{1/2}$ is shown. Spectral-line centers and background offset are determined by Gaussian fits (red curves). Gray areas represent the standard error of the mean (SEM) of fit results for line centers. (a) Spectral line obtained by scanning the modulation frequency of the amplitude-modulated optical lattice. The data are averages of 28 scans with 200 measurements each. Vertical error bar, SEM of the 28 scans. Line center is at 38.76861(1) GHz (black solid line). Inset, simulation results. (b) Reference scan performed by conventional two-photon microwave spectroscopy without the optical lattice, plotted versus twice the microwave frequency. The data are averages of 11 scans with 200 measurements each. Line center is at 38.768545(5) GHz (black dashed line).

Figure 3.2a shows the atomic transition $|58S_{1/2}\rangle \rightarrow |59S_{1/2}\rangle$ driven via amplitude-modulation of the optical lattice. The $|58S_{1/2}\rangle \rightarrow |59S_{1/2}\rangle$ spectrum is obtained by scanning the frequency of the microwave source driving the fiber modulator across the expected transition frequency. The spectral line shown in Figure 3.2a is evidence that the $|58S_{1/2}\rangle \rightarrow |59S_{1/2}\rangle$ transition has been driven in a single step (in first order), at the fundamental transition frequency. The inset in Figure 3.2a shows a simulated spectrum (details given in [41]). The simulation indicates that the sub-structure

in the spectral line originates from different types of center-of-mass trajectories of the atoms in the optical lattice. The dominant central peak results mainly from trapped atoms, whereas the small side structures result from atoms that traverse several lattice wells or that remain nearly stationary close to a lattice maximum during atom-field interaction [41]. The sub-structures, which are observed in the simulation, are not as clearly resolved in the experiment. This is most likely due to inhomogeneous broadening caused by optical-lattice imperfections. The simulation provides motivation to fit the spectrum in Figure 3.2a as a triple-Gaussian, which yields a central-peak location of 38.76861(1) GHz.

For reference, the $|58S_{1/2}\rangle \rightarrow |59S_{1/2}\rangle$ transition is also driven using direct application of microwave radiation at half the transition frequency; in this case the transition results from a two-step (second-order) electric-dipole (E1) coupling through the $58P$ off-resonant intermediate state. Figure 3.2b shows the lattice-free $|58S_{1/2}\rangle \rightarrow |59S_{1/2}\rangle$ spectral line, driven as a two-photon electric-dipole transition at half the transition frequency, using microwaves from a horn directed at the atom-field interaction region. This reference measurement yields a $|58S_{1/2}\rangle \rightarrow |59S_{1/2}\rangle$ transition frequency of 38.768545(5) GHz. The transition frequencies measured in Figures 3.2a and b are in good agreement with each other. The slight blue-detuning of the central peak in Figure 3.2a relative to the peak in Figure 3.2b is due to a light shift from the optical lattice. A calculation based on published quantum defect values [55] predicts a transition frequency at 38.7686(1) GHz, which is in agreement with the experimental measurements. Note that for the two-photon transition shown in Figure 3.2b, the microwave-induced AC Stark shift of the transition frequency is unusually small, due to near-cancellation of the upper- and lower-level AC shifts. This shift of the transition frequency is estimated to be less than 500 Hz, which is insignificant in the above comparisons.

3.2.2 Testing the nature of the atom-field interaction mechanism

Figure 3.3 shows two tests that prove the spectral line shown in Figure 3.2a is caused by a perturbation due to the $\mathbf{A} \cdot \mathbf{A}$ atom-field interaction term in Equation 3.1, which drives transitions via an amplitude-modulated optical lattice. First, Figure 3.3a displays verification that the transition does not originate from a combination of microwave leakage and stray DC fields. Although DC electric fields are carefully zeroed, a stray DC electric field in the atom-field interaction volume could, in principle, weakly perturb the $58S_{1/2}$ and $59S_{1/2}$ levels by increasing P-admixture to these levels. Any microwave-radiation leakage into the atom-field interaction region under the simultaneous presence of a DC electric field would drive the transition as an electric-dipole (E1) transition between the weakly-perturbed $58S_{1/2}$ and $59S_{1/2}$ levels. In order to verify that the spectral line is not due to such a coincidence, I search for a spectral line while leaving all microwave equipment fully powered but blocking the weak, amplitude-modulated optical beam in the Mach-Zehnder interferometer (beam block 'B1' in Figure 3.1). In this case, the atoms are still trapped via the high-power, unmodulated beam. A stray DC electric field and leakage of microwave radiation into the chamber could then drive the transition as a single-step E1 transition. To produce the data in Figure 3.3a, the microwave frequency is scanned in a manner identical with the procedure used for Figure 3.2a. No spectral line is evident in Figure 3.3a. This establishes that lattice light modulation, rather than microwave leakage in the presence of a stray DC electric field, drives the observed transition.

Next, I aim to distinguish between the $\mathbf{A} \cdot \mathbf{A}$ transition mechanism and a possible two-step $\mathbf{A} \cdot \mathbf{p}$ transition mechanism (Equation 3.1). Either mechanism may, in principle, drive the observed $|58S_{1/2}\rangle \rightarrow |59S_{1/2}\rangle$ transition via lattice modulation. However, these fundamentally distinct mechanisms differ in ways that can be tested experimentally.

The modulated light field contains the frequency ω_L and frequency sidebands

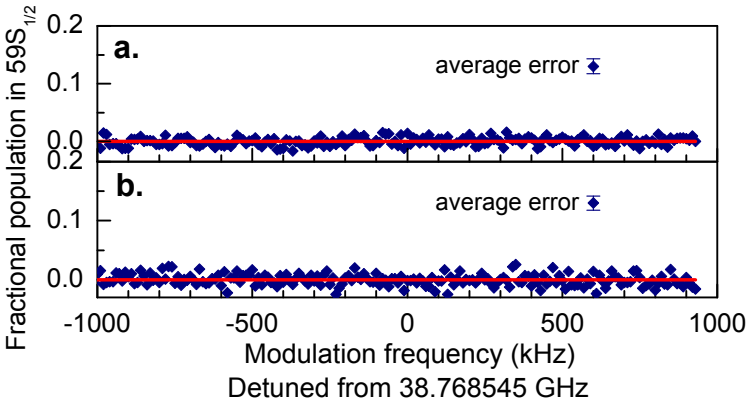

Figure 3.3: **Verification of the nature of the atom-field interaction mechanism.** The fraction of atoms in $59S_{1/2}$ is recorded as the modulation frequency is scanned. The absence of signals is important because it verifies the model presented in the text. Background offset is determined by a constant fit (red line). (a) Test to exclude dipole transitions caused by microwave leakage into the atom-field interaction region, performed using beam block 'B1' (Figure 3.1) during frequency scans, while leaving the microwave source at full power. The data are averages of 16 scans with 200 measurements each. Error bar, SEM of the 16 scans. (b) Test to exclude a stimulated electric-dipole Raman transition, performed using beam block 'B2' (Figure 3.1) during frequency scans. The data are averages of 10 scans with 200 measurements each. Error bar, SEM of the 10 scans.

$\omega_L \pm \Omega$, where ω_L is the laser frequency, and Ω is the microwave modulation frequency of the light intensity (which is resonant with the $|58S_{1/2}\rangle \rightarrow |59S_{1/2}\rangle$ transition). The presence of multiple frequencies allows, in principle, for the $\mathbf{A}\cdot\mathbf{p}$ term to couple $58S_{1/2}$ to $59S_{1/2}$ in a two-step (second-order) process via a stimulated Raman transition through one or more states that have an energy separation $\approx \hbar\omega_L$ from the $58S_{1/2}$ and $59S_{1/2}$ levels. Following E1 selection rules, this mechanism would involve optical $S \rightarrow P$ and $P \rightarrow S$ electric-dipole transitions through distant intermediate P-states. The Raman coupling mechanism would be effective in both running-wave or standing-wave laser fields. On the other hand, the coupling due to the $\mathbf{A}\cdot\mathbf{A}$ term is proportional to $\left\langle 59S_{1/2}\right| I(z) \left|58S_{1/2}\right\rangle \sin(\Omega t)$, where $I(z)$ is the light intensity. For this coupling to be effective in first order, two conditions must be simultaneously fulfilled: the light intensity must substantially vary as a function of position z within the volume of the atom, and the modulation frequency Ω must correspond to the energy-level difference.

Without spatial variation of $I(z)$, the coupling vanishes due to the orthogonality of the atomic states. Hence, the $\mathbf{A} \cdot \mathbf{A}$ coupling is present in the amplitude-modulated standing wave, while it is absent in an amplitude-modulated running wave.

To test whether it is a second-order $\mathbf{A} \cdot \mathbf{p}$ or a first-order $\mathbf{A} \cdot \mathbf{A}$ interaction that causes the spectroscopic signal, I exchange the amplitude-modulated standing-wave optical lattice for an amplitude-modulated running-wave beam by blocking the retro-reflected lattice beam with beam block 'B2' in Figure 3.1. The microwave frequency is then scanned in a manner identical with the procedure used for Figure 3.2a. No spectral line is evident in Figure 3.3b. Therefore, the transition mechanism responsible for the spectral line observed in Figure 3.2a is indeed a single-step atom-field interaction arising from the modulated optical standing-wave intensity (via a first-order $\mathbf{A} \cdot \mathbf{A}$ interaction), not a two-step electric-dipole Raman coupling process arising from the frequency sidebands in the light field (via a second-order $\mathbf{A} \cdot \mathbf{p}$ interaction).

3.2.3 Dependence on experimental parameters

In this section I characterize the dependence of ponderomotive spectroscopy on several experimental parameters. In Figure 3.4 I plot the scaling behavior of the spectral linewidth and amplitude on the atom-field interaction time. Experimentally, the interaction time t_{int} is defined as the time between when the atoms are excited to the $58S_{1/2}$ state and when the atoms are ionized for detection, typically $t_{\text{int}} = 6$ μs. During the atom-field interaction time, the transitions are driven by the amplitude-modulated lattice (which is always on), and the atoms undergo a square-pulse coupling to state $59S_{1/2}$ of duration t_{int}. In the limit of weak saturation and assuming a Fourier-limited spectral profile of the driving field, the full-width-at-half maximum (FWHM) of the spectral line is expected to decrease with increased interaction time as $\approx 0.9/t_{\text{int}}$. This agrees with the trend observed in Figure 3.4. A double-Gaussian fit of the 3 μs spectral line and triple-Gaussian fits of the 6-and-9-μs spectral lines

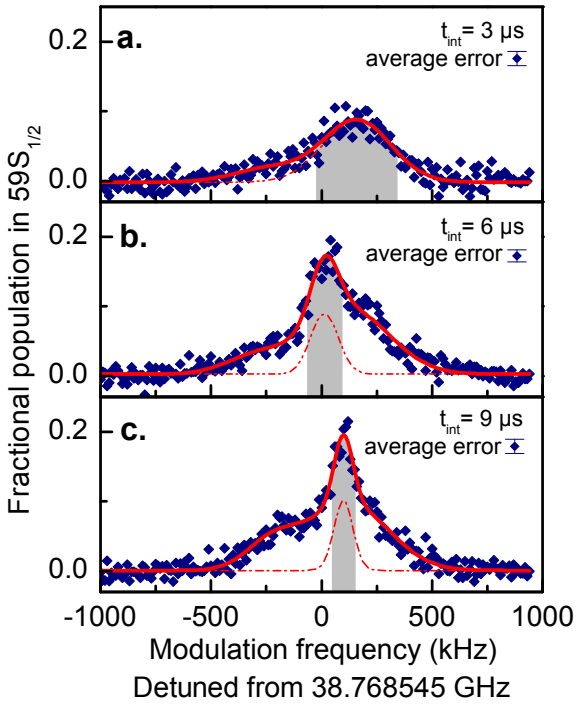

Figure 3.4: **Dependence of amplitude-modulation-driven $|58S_{1/2}\rangle \rightarrow |59S_{1/2}\rangle$ spectral line on interaction time.** (a)-(c) For each interaction time $t_{\rm int}$ with the modulated lattice, the fraction of atoms in $59S_{1/2}$ is recorded while scanning the microwave modulation frequency. The data are averages of 8 scans with 200 measurements each. Error bar, SEM of the 8 scans. The data for $t_{\rm int}$ = 3 (6 and 9) μs are fit with double- (triple-) peak Gaussians (red solid curves). The FWHM (gray areas) of the dominant Gaussians (red dashed curves) decrease with increasing $t_{\rm int}$, and the heights increase.

(red solid curves in Figure 3.4) indicate that the FWHM of the dominant Gaussian components in each line (red dashed curves) are within 20% of the Fourier limit.

Examining the spectral lines in Figure 3.4 further, it can be seen that the maximum signal height approximately doubles between 3 and 6 μs; the additional increase between 6 and 9 μs is relatively minor. This observation is consistent with a Rabi frequency within the range of $\chi/(2\pi) \sim$ 50-100 kHz. This result is in qualitative agreement with the calculated Rabi frequency presented in Appendix A.

In Figures 3.5 and 3.6 I summarize the dependence of the spectral-line height on additional experimental parameters. In Figure 3.5 I plot the dependence of spectral-line height on modulation strength, which is controlled by varying the amplitude of

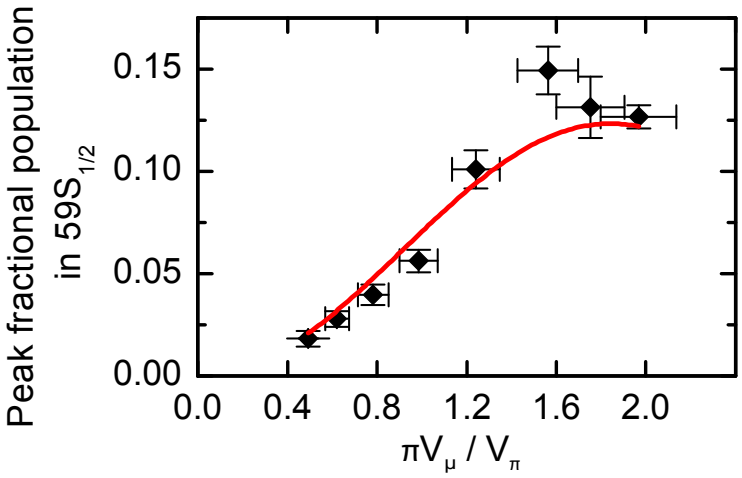

Figure 3.5: **Dependence of the height of the $|58S_{1/2}\rangle \rightarrow |59S_{1/2}\rangle$ spectral line on microwave voltage amplitude.** The peak fraction of $59S_{1/2}$ atoms is recorded versus $\pi V_\mu/V_\pi$, where the microwave voltage amplitude V_μ applied to the fiber modulator is varied (V_π is fixed). Each data point represents the observed peak height for an average of 5 scans with 200 measurements each. Vertical error bars, uncertainty of peak height. Horizontal error bars are due to the uncertainty in V_π. Red curve, fit proportional to $\mathrm{J}_1^2(\pi V_\mu/V_\pi)$.

the microwave voltage signal V_μ that drives the fiber modulator. As can be seen in Equation 3.2, the Rabi frequency χ has a first-order Bessel function (J_1) dependence on V_μ. Because the height of the spectral line indicates the peak fraction of population in $59S_{1/2}$, it is expected that in the limit $\chi t_{\mathrm{int}} \ll \pi$ (here, $\chi t_{\mathrm{int}} \approx 0.6$), the height will scale as $(\chi t_{\mathrm{int}})^2 \propto \mathrm{J}_1^2(\pi V_\mu/V_\pi)$ for fixed t_{int}. In Figure 3.5, the spectral line height is plotted as a function of the Bessel function argument, $\pi V_\mu/V_\pi$, as V_μ is varied. A $\mathrm{J}_1^2(\pi V_\mu/V_\pi)$ fit to the data yields good agreement.

The spectral-line height also depends on the distance of the retro-reflector from the atoms. Both the incident and the retro-reflected amplitude-modulated lattice beams can be viewed as periodic sequences of pulses with a repetition frequency Ω. The spectral-line height is maximal if the pulse trains of the incident and retro-reflected lattice beams arrive synchronously at the atoms' location. Considering the time delay between the retro-reflected and incident pulses, it is seen that the spectral-line height should sinusoidally vary with the position of the retro-reflector mirror with a period

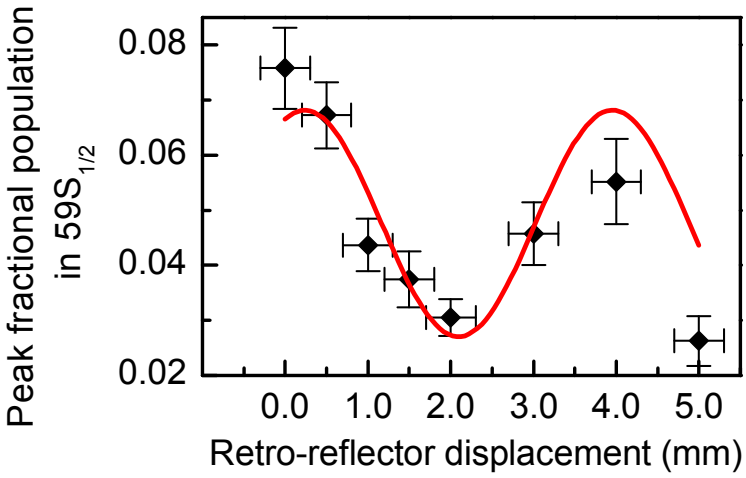

Figure 3.6: **Dependence of the height of the $|58S_{1/2}\rangle \rightarrow |59S_{1/2}\rangle$ spectral line on retro-reflector position.** The peak fraction of $59S_{1/2}$ atoms is recorded versus the lattice retro-reflector distance from the atoms. Each data point represents the observed peak height for an average of 3 scans with 200 measurements each. Vertical error bars, uncertainty of peak height. Horizontal error bars, distance uncertainty. A sinusoidal curve (red) with a period of 4 mm is plotted for reference.

of $c/(2\Omega) \sim 4$ mm, where c is the speed of light. Figure 3.6 displays the spectral-line height as a function of retro-reflector displacement over a range of a few millimeters. A sinusoidal curve with a period of 4 mm has also been plotted for reference. There is good qualitative agreement, with deviations attributed to alignment drift of the excitation beams during acquisition of multiple data scans. This test provides another verification of the ponderomotive nature of the transition mechanism.

3.3 Discussion

3.3.1 Quantized-field interpretation

In the analysis of the experimental evidence above, I have presented a classical-field picture. Spectroscopy using the ponderomotive interaction can also be interpreted using quantized fields. Using quantized fields, the lattice beams carry photons of three different frequencies: the optical carrier frequency, ω_L, and the optical carrier frequency with microwave sidebands, $\omega_L \pm \Omega$. The transitions described in this chapter

(and in Chapter IV and Chapter V) are due to absorption of a photon from one lattice beam and (simultaneous) re-emission of a photon into the other lattice beam, with the frequency difference between the two photons being Ω. It is necessary to have two counter-propagating (or non-co-propagating) fields in order to retain the spatial coupling between Rydberg levels.

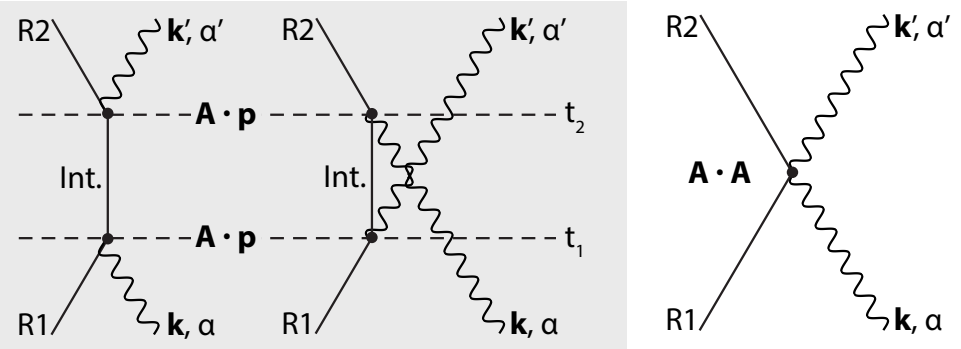

Figure 3.7: **Feynman diagrams comparing inelastic second-order $\mathbf{A}\cdot\mathbf{p}$ and first-order $\mathbf{A}\cdot\mathbf{A}$ processes.** Although each process begins in an atomic state $R1$ and photon mode $(\mathbf{k},\alpha)$ and ends in an atomic state $R2$ and photon mode $(\mathbf{k}',\alpha')$, the processes are fundamentally different. Two types of inelastic second-order $\mathbf{A}\cdot\mathbf{p}$ processes (gray region) are displayed, showing intermediate absorption and emission stages between times t_1 and t_2. On the other hand, the $\mathbf{A}\cdot\mathbf{A}$ process (white region) is a simultaneous interaction with two photons.

In the standard description of the interaction between an atom and a quantized electromagnetic field, the $\mathbf{A}\cdot\mathbf{p}$ term in Equation 3.1 leads to well-known multipole transitions characterized as E1, M1, E2, etc. The terms arise from an expansion of the exponential phase factor e^{ikz} of the field, assuming a plane running wave propagating in the z-direction (without spatial amplitude modulation). The leading term of the expansion, E1, describes electric dipole transitions. These are often dominant, but higher-order terms such as the electric-quadrupole term, E2, are also used in precision spectroscopy [56]. All electromagnetic multipole transitions, can, in principle, be driven in first order and are associated with well-known selection rules [54]. One common way to visualize first-order E1, M1, E2, etc., $\mathbf{A}\cdot\mathbf{p}$ transitions is via a three-branch Feynman diagram [54] (one vertex with three branches), in which an atom in

an initial state transitions into a final state by absorption or emission of a photon.

On the other hand, the common way in which to visualize first-order $\mathbf{A} \cdot \mathbf{A}$ interactions is via a four-branch Feynman diagram [54] (one vertex with four branches, as in Figure 3.7c), in which an atom in an initial state interacts simultaneously with an incoming and an outgoing photon, resulting in an atom in a final state. When a plane running wave is assumed, the atomic state and the photon energy are unchanged. The process is an elastic scattering process that gives rise to Thomson scattering.

However, if the field amplitude substantially varies within the volume of the atom, as is the case in the present work, then the field is not a plane running wave, and the atomic state and the photon energy may indeed be changed (an inelastic process). Such a state-changing $\mathbf{A} \cdot \mathbf{A}$ interaction is typically not considered in spectroscopy because the field intensity is typically constant within the volume of the atom. In the work presented in this chapter, I have demonstrated that a field inhomogeneity can be intentionally introduced into an atom-field system so that the $\mathbf{A} \cdot \mathbf{A}$ interaction results in state-changing transitions. Explicitly, since $\mathbf{A} \cdot \mathbf{A}$ is proportional to field intensity I, the matrix element $\langle R2|\mathbf{A} \cdot \mathbf{A}|R1\rangle$ representing a transition between two (different) Rydberg states $|R1\rangle$ and $|R2\rangle$ is different from zero only if $\langle R2|I|R1\rangle \neq 0$, i.e. if the intensity I depends on position within the atom. For fixed intensity the matrix element vanishes due to the orthogonality of the atomic states. Therefore, to drive transitions the light field must contain different spatial modes, to retain the spatial coupling between the Rydberg levels, and different optical frequencies, with a frequency difference corresponding to the energy difference between states $|R1\rangle$ and $|R2\rangle$. An optical lattice that is amplitude-modulated at the desired atomic transition frequency, such as the lattice used in this work, satisfies these conditions.

As shown in the white region of Figure 3.7, these transitions can be further described in terms of the four-branch Feynman diagram [54] referenced above: Instantaneous exchange of a photon between two different field modes ($\mathbf{k}$ representing the

wavevector and α representing polarization) of the lattice yields different initial and final Rydberg states $|R1\rangle$ and $|R2\rangle$. Finally, it should be noted that this process is not the same as stimulated Raman scattering because the latter is a second-order $\mathbf{A} \cdot \mathbf{p}$ process through an intermediate state, which can be visualized by a sequence of two three-branch, $\mathbf{A} \cdot \mathbf{p}$-type Feynman diagrams (gray region in Figure 3.7).

3.3.2 Advantages of using the ponderomotive interaction

While transitions driven by the $\mathbf{A} \cdot \mathbf{A}$ term and transitions driven by the $\mathbf{A} \cdot \mathbf{p}$ term (E1, E2, E3, etc., in first- and higher-order) may connect the same atomic states, I have explained above that the physical origins of these mechanisms are quite different, resulting in different scaling laws. For instance, the Rabi frequencies of first-order multipole transitions are linearly proportional to the driving field, while Rabi frequencies in ponderomotive spectroscopy are linearly proportional to the intensity (see Equation 3.2).

One advantage of ponderomotive spectroscopy over established spectroscopic methods is flexible transition rules. Ponderomotive spectroscopy affords single-step access to atomic transitions that are forbidden by electric-dipole selection rules, an example of which is the $|58S_{1/2}\rangle \rightarrow |59S_{1/2}\rangle$ transition demonstrated in this chapter. Atomic states with large differences in angular momentum can be coupled by choosing an appropriate atom size relative to the lattice period [43]. Accurate measurements of transitions for a wide range of angular-momentum separations may improve the determination of quantum defects and other atomic constants.

As with any high-precision measurement method, light-induced level shifts must be considered. In spectroscopic studies of low-lying atomic states, E2 transitions in the optical spectral range between long-lived states can be driven as a single-photon process in low-intensity fields [56]. In contrast, in microwave spectroscopy of Rydberg levels, similar transitions are usually driven as E1 transitions in higher

order (see, for instance, Figure 3.2b), necessitating relatively strong microwave fields. These typically result in strong AC Stark shifts of the measured transition (the small shift seen in Figure 3.2b is an anomaly of the specific transition in rubidium). On the other hand, in ponderomotive spectroscopy, light-induced shifts originate solely from the optical trapping fields acting on the Rydberg levels via the non-state-changing part of the $\mathbf{A}\cdot\mathbf{A}$ interaction. While in the present work these shifts are relatively large (on the order of 100 kHz), state-of-the-art laser cooling techniques will allow users to reduce the atom temperature from $\sim$100 μK (this chapter) to $\lesssim$1 μK (proposed in Chapter VIII). This will allow a reduction of the trap depth and associated light shifts by at least a factor of 100. Furthermore, the differential light shift between selected upper and lower Rydberg levels cancels under magic-wavelength conditions, leading to at least one more order-of-magnitude reduction in the shift of the measured transition. I experimentally demonstrate the existence of these magic-wavelength conditions in Chapter IV. Therefore, ponderomotive spectroscopy could have immediate potential as a new tool for high-precision spectroscopy of Rydberg atoms.

Furthermore, another powerful innovation afforded by ponderomotive spectroscopy is a spatial resolution orders of magnitude better than the frequency of the transition would suggest. Electronic transitions in a particle are typically driven by applying radiation resonant with the transition frequency. The best possible spatial resolution will be at the diffraction limit of the applied radiation, which is on the order of the wavelength corresponding to the transition frequency and, in most cases, orders of magnitude larger than the particle size. In contrast, in ponderomotive spectroscopy, the frequency of the applied radiation is very different from the frequency of the transition being driven. The applied radiation is a standing wave with a wavelength on the order of the particle size. The frequency resonant with the desired transition is introduced by amplitude-modulating the standing wave. In this chapter, a microwave-frequency atomic transition (typical resolution: centimeter-scale) has been

driven by amplitude-modulating a standing-wave optical lattice (typical resolution: micrometer-scale). This spatial addressability could streamline certain gate schemes in quantum computing, especially those schemes involving controlled electrostatic interactions between Rydberg atoms [7, 9]. For example, by using site-selective transitions driven by ponderomotive spectroscopy, a recently-proposed controlled-z gate scheme [57] could be modified such that the same Rydberg state is used for both control and target qubits (and no microwave field is needed).

In this chapter, I have described a successful first-time demonstration of spectroscopy using the ponderomotive interaction. I have shown major advantages over standard spectroscopy, including improved spatial addressability and flexible transition rules, which are relevant in a broad range of applications. Using a temporally- and spatially-modulated ponderomotive potential, an atomic microwave transition forbidden by established electric-dipole selection rules has been driven with a spatial resolution in the micrometer range. One application of the method is in quantum computing [9, 58], where single-site addressability plays a central role. Another application is in precision measurement of atomic characteristics [28] and physical constants (e.g. the Rydberg constant [59], leading to the proton size [11]); there, flexible spectroscopic transition rules will be very convenient. In the future, it may be possible to explore extending ponderomotive spectroscopy to smaller-sized atoms or molecules trapped in shorter-wavelength optical lattices.

In the next chapter, I expand upon this novel demonstration by employing higher harmonics in the lattice modulation to drive Rydberg-Rydberg transitions. I also demonstrate magic-wavelength conditions, positioning this spectroscopy to be used in future precision-measurement efforts.

CHAPTER IV

Magic Wavelengths and Spectroscopy Using Lattice-Modulation Harmonics

As introduced throughout this dissertation, measurements of atomic transition frequencies are the cornerstone of precision metrology, used in applications ranging from atomic clocks [60] to measuring gravitational redshifts [61] and the radius of the proton [11]. An important metric of precision in these applications is the relative uncertainty, $\Delta\nu/\nu$, in which ν is the measured frequency and $\Delta\nu$ is its absolute uncertainty. In order to obtain the lowest $\Delta\nu/\nu$, it is desirable to increase ν while decreasing $\Delta\nu$. In the previous chapter, the novel technique of ponderomotive spectroscopy was demonstrated, wherein Rydberg atoms are trapped in a standing-wave laser field (optical lattice). Electronic transitions are driven by modulating the lattice-light intensity at the transition frequencies of interest. In this chapter, I employ nonlinearities intrinsic to this excitation process to increase ν by driving atomic transitions at higher harmonics of the modulation frequency. I also identify magic transitions that minimize trap-induced line shifts and reduce the uncertainty $\Delta\nu$ by about one order of magnitude.

First, I describe modifications to the experimental set-up from Chapter III that introduce harmonics into the lattice modulation. After, I present the results, which demonstrate suitability of ponderomotive spectroscopy for precision measurement ap-

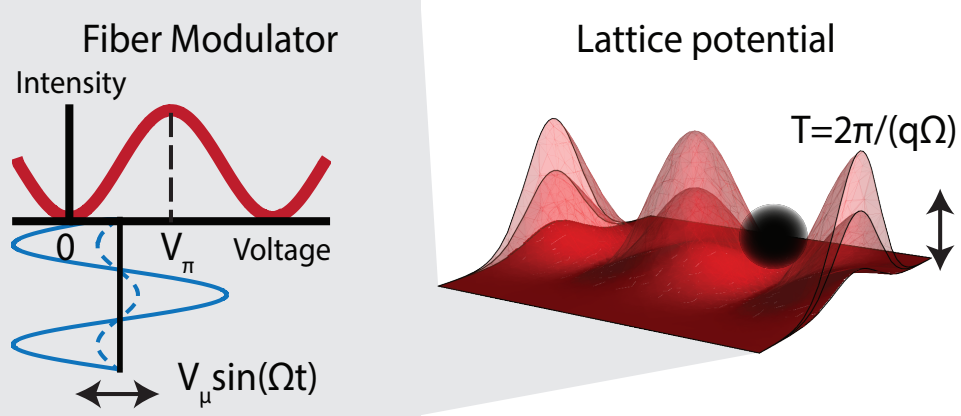

Figure 4.1: **Modifications to experimental set-up to introduce lattice-modulation harmonics.** See Chapter III for full set-up details. Here, the fiber modulator optical transmission function (red curve) is driven (blue voltage curves) at a fundamental modulation frequency Ω. The lattice modulation period in qth order is $T = 2\pi/(q\Omega)$, where $q>1$ becomes prominent as $V_\mu > V_\pi/2$.

plications.

4.1 Experimental Set-Up

As described in Chapter III, temporal harmonics in the lattice modulation drive transitions at frequencies $q\Omega$, where q is an integer. The EOM offset voltage is set to $V_\pi/2$ (see inset in Figure 4.1). Modulation at the fundamental frequency Ω occurs when $V_\mu \lesssim V_\pi/2$ (dashed blue line), as was demonstrated in Chapter III. To access higher harmonics, V_μ is increased (solid blue line). The resultant frequency upconversion is described by

$$\frac{I_{\mathrm{sw}}^{\mathrm{dyn+fixed}}}{I_{0\,\mathrm{inc}}^{\mathrm{fixed}}} = 1 + 2\left(\frac{\eta}{2} + \eta\sum_{q=1,3,5\ldots}^{\infty} \mathrm{J_q}\left(\frac{\pi V_\mu}{V_\pi}\right)\sin\left(q\Omega t\right)\right)^{1/2} + \eta\left(\frac{1}{2} + \sum_{q=1,3,5\ldots}^{\infty} \mathrm{J_q}\left(\frac{\pi V_\mu}{V_\pi}\right)\sin\left(q\Omega t\right)\right), \tag{4.1}$$

where the total incident intensity $I_{\mathrm{sw}}^{\mathrm{dyn+fixed}}$ at the location of the atoms is scaled by $I_{0\,\mathrm{inc}}^{\mathrm{fixed}}$, the intensity of the fixed (unmodulated) high-power beam. This expression

is derived in detail in Appendix A. Here, η is the power ratio between the dynamic (modulated) and fixed (unmodulated) beams in the interferometer. A Fourier analysis of Equation 4.1 with $\eta = 0.0077$ (typical experimental value) leads to the Rabi frequency for the qth harmonic as a function of modulation strength V_μ/V_π (shown in Figure 4.2).

The Rabi frequency is scaled by $I_{0\,\mathrm{inc}}^{\mathrm{fixed}}$ (in units of W/m^2), $\sqrt{\varepsilon}$, and $D_{n,l,m}^{n',l',m}$. For this experiment, ε is a factor included to account for inefficiencies in the lattice optics system, as derived in Appendix A. Specifically, ε is the ratio of the return and incident lattice-beam intensities, and $\varepsilon = 0.09$ for this system. The matrix elements for the spatial coupling, $D_{n,l,m}^{n',l',m}$, have previously been obtained in Reference [43] and are also described in Chapter III.

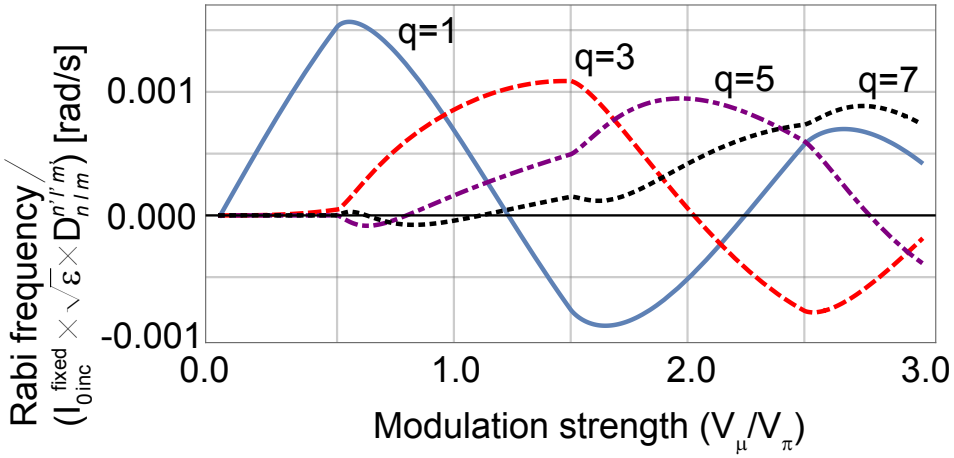

Figure 4.2: **Scaled Rabi frequencies of the qth harmonics of the lattice modulation.** These are calculated as a function of V_μ (units of V_π). Even-order harmonics are not plotted because in this set-up the modulated EOM voltage is centered at $V_\pi/2$, and therefore odd orders dominate the modulation spectrum when atom center-of-mass locations are at lattice intensity minima or maxima.

The Rabi frequencies exhibit a sinusoidal dependence on position in the optical lattice [62] and, for even-parity transitions (the case demonstrated here), are maximal for atoms at lattice intensity maxima and minima. Since the peak Rabi frequencies in Figure 4.2 slowly decrease as a function of q, unlike in typical nonlinear spectroscopy,

$I_{0\,\mathrm{inc}}^{\,\mathrm{fixed}}$ does not need to be increased to realize higher-order transitions, thereby avoiding increased light shifts. Figure 4.2 is utilized to determine the V_μ needed to achieve a high Rabi frequency at the harmonic order of interest. In this experiment, $S \rightarrow S$ transitions are targeted because they are insensitive to the MOT magnetic field (which is always on). Under traditional electric-dipole selection rules, these transitions would not be allowed in first-order perturbation theory. However, because ponderomotive spectroscopy is employed, typical selection rules do not apply [43].

4.2 Results

4.2.1 Nonlinear drive using modulation harmonics

Figure 4.3 displays the results of driving the ponderomotive transition $|52S_{1/2}\rangle \rightarrow |53S_{1/2}\rangle$ via the third harmonic ($q = 3$) of the lattice modulation. For this transition, $D_{52S}^{53S} = 0.19$, which is near in value to the maximal value for $nS \rightarrow (n+1)S$ transitions, $D_{58S}^{59S} = 0.215$. The inset in Figure 4.3a shows that most spectral features can be reproduced by a semi-classical simulation. Details of the simulation can be found in Reference [62]. The two outermost peaks are attributed to atoms that are anti-trapped (red-detuned peak) or trapped (blue-detuned peak) in the lattice [40, 41]. The simulation and auxiliary analysis does not reproduce the sharp central peak in the experimental spectrum.

To determine the frequency of the transition, I fit the smoothed, averaged spectral line in Figure 4.3a to a triple-Gaussian. To eliminate most of the trap-induced systematic shifts, I take the mean of the center locations of the outermost peaks. Assuming a perfect optical lattice, the outermost peaks correspond to equal but opposite extremum light shifts from the unperturbed Rydberg-Rydberg transition. Therefore, the mean provides a measurement of the transition line center ν_{meas} with much-reduced light shift. Results are summarized in Table 4.1.

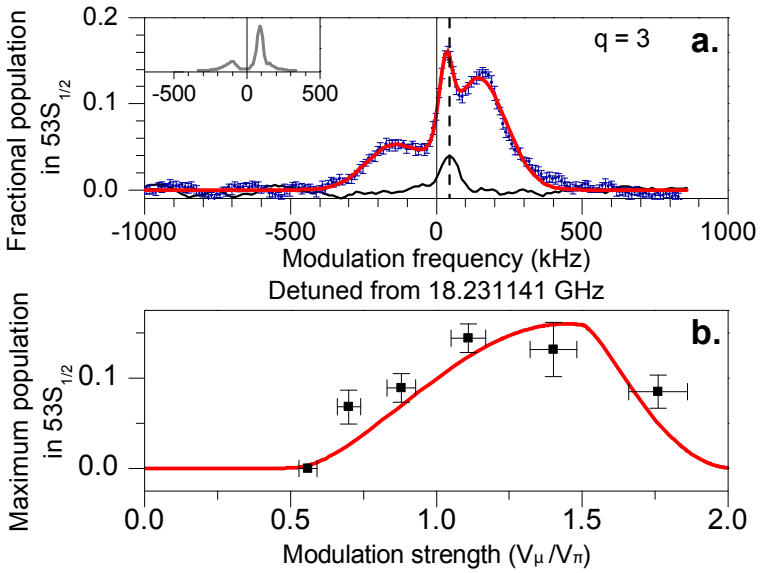

Figure 4.3: **Third-harmonic drive.** (a) Population in $53S_{1/2}$ as a function of fundamental lattice modulation frequency Ω, detuned from the measured central frequency ν_{meas}, which is consistent with the third sub-harmonic of the expected transition energy interval (see Table 4.1). Data are a smoothed average of 10 scans with 200 measurements per frequency step. Error bars, standard error of the mean (SEM). Red curve, triple-Gaussian fit. Vertical black line, line center. Black dashed line, center location of a two-photon microwave spectroscopy measurement (black curve). Inset, simulation results. (b) Peak $53S_{1/2}$ population as a function of modulation strength V_μ. For each data point, 6-10 scans are taken. Vertical (horizontal) error bars, peak height (V_π) uncertainty. Red curve, proportional to the square of the $q = 3$ curve in Figure 4.2.

Figure 4.3b shows the dependence of the $53S_{1/2}$ excited-state population on modulation strength V_μ/V_π. The behavior qualitatively agrees with the square of the Rabi frequency for the $q = 3$ curve in Figure 4.2, plotted for comparison. In particular, significant excited-state populations only occur beyond a threshold value of $V_\mu/V_\pi \approx 0.6$. Figure 4.3b reinforces that the spectrum in Figure 4.3a is due to the nonlinear $q = 3$ component of the lattice modulation.

In the context of high-precision spectroscopy, a low relative uncertainty $\Delta\nu/\nu$ is desired. Therefore, if the measurement uncertainty $\Delta\nu$ is unchanged, a lower relative uncertainty can be attained by driving transitions at higher frequencies ν. To reach higher-frequency transitions, I drive transitions at higher q. Figure 4.4 displays the

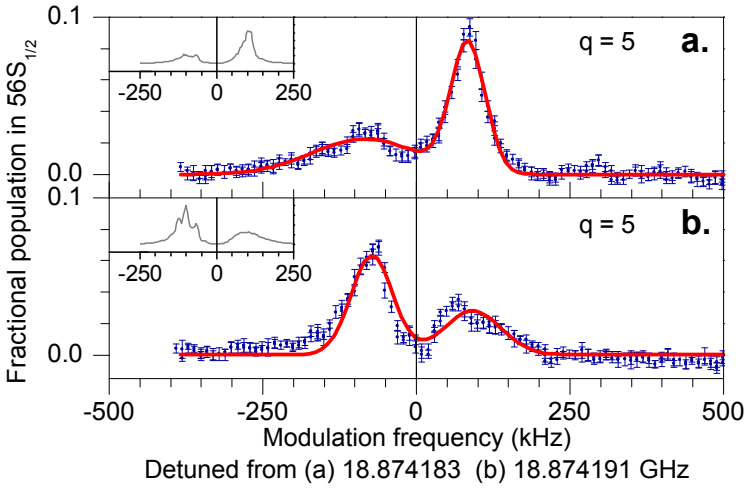

Figure 4.4: **Fifth-harmonic drive.** Population in $56S_{1/2}$ as a function of fundamental lattice modulation frequency Ω, detuned from the measured central frequency ν_{meas}, which is consistent with the fifth sub-harmonic of the expected transition energy interval (see Table 4.1). Data are displayed for Rydberg atoms prepared at lattice potential (a) minima (b) maxima. Data are a smoothed average of (a) 18 (b) 10 scans, 200 measurements each. Error bars, SEM. Red curve, double-Gaussian fit. Vertical black line, line center. Insets, simulation results.

ponderomotive transition $|54S_{1/2}\rangle \rightarrow |56S_{1/2}\rangle$, which has $D_{54S}^{56S} = 0.08$, via the fifth harmonic ($q = 5$). The spectra in Figures 4.4a and b are reproduced accurately by the simulations (insets). As before, the red-detuned (blue-detuned) peak is mostly due to atoms that are anti-trapped (trapped) in the lattice. Here, I demonstrate the relation between Rydberg-atom position and light-shift polarity by preparing the Rydberg atoms either near a potential minimum (Figure 4.4a), which results in mostly trapped atoms with positive light shifts; or maximum (Figure 4.4b), which results in mostly anti-trapped atoms with negative light shifts [27].

To determine the line center, I fit the spectra in Figures 4.4a and b to double-Gaussian functions. The mean of the center locations of the peaks yields a measurement in which the systematic light shifts mostly cancel. Table 4.1 contains the results. The $q = 5$ transition in Figure 4.4 has a transition frequency of about 94.4 GHz. Hence, this scheme approaches the sub-THz regime, which is important for improving $\Delta\nu/\nu$ in precision frequency measurements. Specifically, $\sim$94 GHz is

the frequency of the transition that will be measured with high precision to obtain a new value of the Rydberg constant (Chapter VIII). With this demonstration of utilizing harmonics of the lattice modulation to drive Rydberg-Rydberg transitions, I have proven the suitability of this method for the Rydberg constant measurement.

4.2.2 Magic conditions in a modulated lattice

Magic-wavelength lattices play an important role because they allow for probing atoms in a light trap while avoiding systematic line-shifts due to the trap [1]. In a ponderomotive lattice, a magic condition occurs when a Rydberg atom becomes comparable in size to the lattice period, detailed in Appendix B. The lattice-induced shifts of certain upper and lower Rydberg levels are nearly the same [37] and cancel in the measured transition frequency. For Rb $nS_{1/2}$ atoms in a 1064-nm lattice, this occurs for lower- and upper-level principal quantum numbers symmetric about 69.5. Furthermore, for principal quantum numbers between $n = 66 - 73$, the sign of the effective polarizability of the atoms is reversed, indicating that Rydberg atoms are attracted to lattice-field maxima. This case differs from the more typical case where Rydberg atoms are attracted to field minima. This topic is also detailed in Appendix B.

Figure 4.5 displays the results of driving the magic transition $|69S_{1/2}\rangle \rightarrow |70S_{1/2}\rangle$, for which $D_{69S}^{70S} = 0.13$, at the fundamental frequency ($q = 1$). The trap depths (light shifts) for both states are about the same (2.2% of the free-electron ponderomotive trap depth). The magic condition results in a lineshape that is symmetric and has a narrow central feature. These characteristics are well-reproduced by the simulation (inset). To determine the line center, I fit the central feature, expected to have nearly-zero systematic light shift, to a single Gaussian. This measurement has 2 kHz statistical uncertainty (see Table 4.1).

In Figure 4.6 I show a combination of both magic and nonlinear ponderomotive

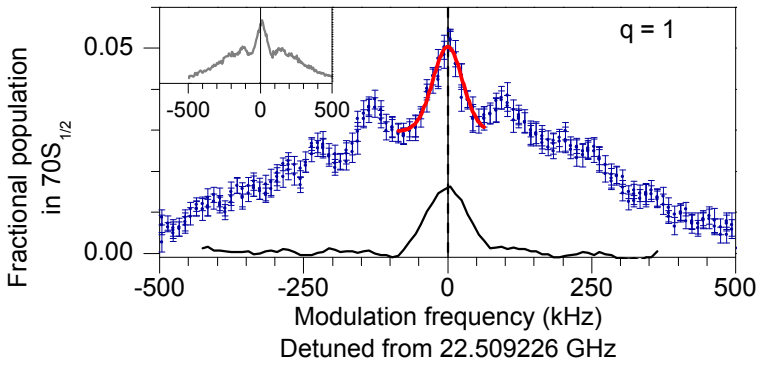

Figure 4.5: **Magic condition, fundamental.** Population in $70S_{1/2}$ as a function of fundamental lattice modulation frequency Ω, detuned from the measured central frequency ν_{meas}, which is consistent with the expected transition energy interval (see Table 4.1). Data are a smoothed average of 18 scans, 200 measurements each. Error bars, SEM. Red curve, single-Gaussian fit. Vertical black line, line center. Black dashed line, center location of a two-photon microwave spectroscopy measurement (black curve).

spectroscopy, which has the greatest potential to improve $\Delta\nu/\nu$. Here, the magic transition $|68S_{1/2}\rangle \rightarrow |71S_{1/2}\rangle$ (which has $D_{68S}^{71S} = 0.08$) is driven via the third harmonic ($q = 3$). The trap depths for these states are both approximately 2.0% of the free-electron ponderomotive trap depth. The lineshapes are reproduced well by simulations (insets). In Figure 4.6a, Rydberg atoms are prepared at trapping potential minima and a narrow central peak is observed, the location of which agrees very well with the result of a two-photon microwave spectroscopy measurement (also shown). This peak is largely due to trapped atoms, which experience a Rabi frequency that is approximately fixed in phase throughout the atom-field interaction time. This leads to a large pulse area and a central peak at zero detuning.

Other spectral features observed in Figure 4.6 are attributed to the effect of atoms passing over the shallow lattice wells, because of which the position-dependent Rabi frequency then flips sign at the lattice inflection points. For example, in Figure 4.6b, atoms are prepared at lattice potential maxima. From here, the atoms are likely to traverse several wells during the interaction time, resulting in several flips of the Rabi-frequency sign. This leads to a rotary-echo-like effect [31] (i.e. small net pulse

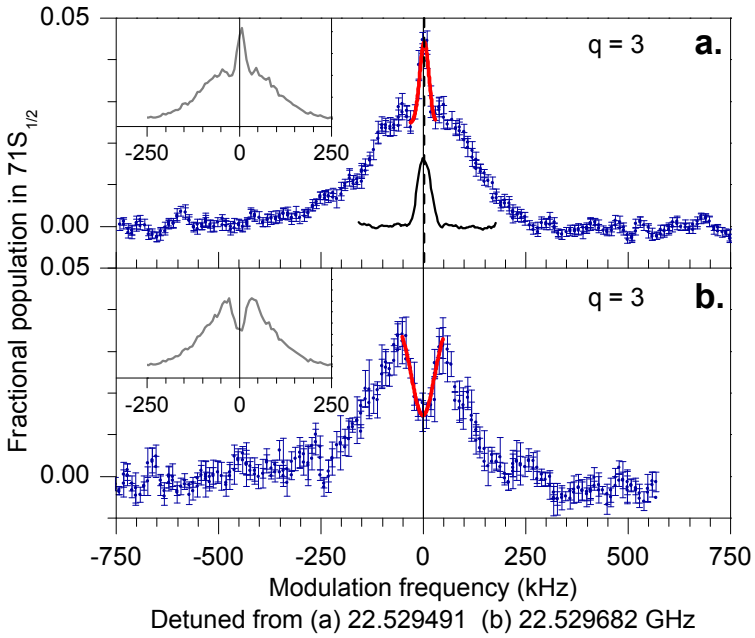

Figure 4.6: **Magic condition, third harmonic.** Population in $71S_{1/2}$ as a function of fundamental lattice modulation frequency Ω, detuned from the measured peak frequency ν_{meas}, which is consistent with the third sub-harmonic of the expected transition energy interval (see Table 4.1). Data are a smoothed average of (a) 12 (b) 5 scans, 200 measurements each. Error bars, SEM. Red curve, single-Gaussian fit. Vertical black line, line center. (a) Lattice not inverted. Black dashed line, center location of a two-photon microwave spectroscopy measurement (black curve). (b) Lattice inverted.

area and transition probability). A small non-zero detuning (partially) negates the echo effect, leading to the central dip observed in Figure 4.6b. Likewise, the small oscillations near the central peak in Figure 4.5 (and to a lesser extent in Figure 4.6) are also due to the interplay between consecutive Rabi-frequency sign-flips at the lattice inflection points and the detuning-induced phase, which cause the detuning-dependent oscillations. These motional effects are complex and require numerical analysis to solve for exact solutions describing the atom-field interaction. I therefore explore the problem numerically in Chapter V.

Because both Figures 4.5 and 4.6 correspond to a magic condition, the respective frequency measurements, based on the central peaks, are expected to have nearly-zero light shift. In both cases, the symmetry of the lineshapes agrees with expec-

		$q\nu_{\mathrm{meas}}$(GHz)	ν_{th}(GHz)	$2\nu_{2\mathrm{p}}$(GHz)
$52S_{\frac{1}{2}} \rightarrow 53S_{\frac{1}{2}}$ q=3		54.693423(15) [2.7×10^{-7}]	54.693577(5) [9×10^{-8}]	54.693556(6) [1×10^{-7}]
$54S_{\frac{1}{2}} \rightarrow 56S_{\frac{1}{2}}$ q=5	a.	94.370915(15) [1.6×10^{-7}]	94.371060(8) [8×10^{-8}]	
	b.	94.370955(15) [1.6×10^{-7}]	94.371060(8) [8×10^{-8}]	
$69S_{\frac{1}{2}} \rightarrow 70S_{\frac{1}{2}}$ q=1		22.509226(2) [9×10^{-8}]	22.509227(1) [4×10^{-8}]	22.509226(2) [9×10^{-8}]
$68S_{\frac{1}{2}} \rightarrow 71S_{\frac{1}{2}}$ q=3	a.	67.588473(2) [3×10^{-8}]	67.589048(4) [6×10^{-8}]	67.588478(1) [1×10^{-8}]
	b.	67.589046(9) [1×10^{-7}]	67.589048(4) [6×10^{-8}]	

Table 4.1: Summary of results. All measurement uncertainties, statistical. Transitions below the double-line table divider are magic. Quantities in brackets are $\Delta\nu/\nu$. Here, ν_{meas} represents measurements performed via ponderomotive spectroscopy, ν_{th} represents theoretically-expected results, and $\nu_{2\mathrm{p}}$ represents measurements performed via traditional microwave spectroscopy. See text for details.

tations, as outlined in Appendix B. The $\approx$ 200 kHz discrepancy observed between Figures 4.6a and b is attributed to differing residual electric fields, causing different systematic DC shifts between the data sets (which were taken on different days).

In both Figures 4.5 and 4.6 the central peaks in the lattice-modulation spectra and the peaks in the two-photon reference spectra are at Fourier-limited resolution. Therefore, precision measurements made via magic-condition ponderomotive spectroscopy and traditional microwave spectroscopy can have similar spectral resolution. However, nonlinear ponderomotive spectroscopy permits access to a wider variety of typically-forbidden transitions at high frequencies.

4.2.3 Summary of results

Table 4.1 summarizes the transition frequencies ($q\nu_{\mathrm{meas}}$) measured in the modulated lattice, the expected transition frequencies (ν_{th}) calculated using quantum

defects from Reference [55], and the reference measurements ($2\nu_{2p}$) obtained via two-photon microwave spectroscopy in the absence of a lattice. The terms in brackets represent $\Delta\nu/\nu$ for each frequency value. Overall, agreement is quite satisfactory. Statistically significant shifts in the measured results from the calculated values are negative, indicating possible Stark shifts due to residual DC electric fields. In the magic-condition cases, the statistical uncertainty in $q\nu_{\mathrm{meas}}$ is on the same order as the uncertainty in $2\nu_{2p}$.

The data presented in this chapter shows that in magic-lattice spectroscopy on trapped atoms the statistical uncertainties are transform-limited. Therefore, nonlinear magic-condition ponderomotive spectroscopy improves the relative uncertainty $\Delta\nu/\nu$ by increasing ν by a factor of q. For a given atom-field interaction time t_{int} and transform-limited transitions, $\Delta\nu/\nu$ improves from $\approx 1/(t_{\mathrm{int}}\nu_{\mathrm{meas}})$ to $\approx 1/(qt_{\mathrm{int}}\nu_{\mathrm{meas}})$. With improved stray electric field control, the modulated lattice should be suitable for precision measurement of (dipole-forbidden) atomic transitions at high frequencies.

In this chapter, I have presented ponderomotive spectroscopy of Rydberg atoms by employing higher harmonics of the lattice modulation. The nonlinearity intrinsic to the lattice modulation has allowed access to transition frequencies ν near the sub-THz regime, with the potential to exceed that limit, using modulation sources that are much lower in frequency. Using magic lattices, I have demonstrated Fourier-limited spectral lines with a small $\Delta\nu$, as well as reduced light shifts. Being able to access sub-THz atomic transitions with low $\Delta\nu$ and free from light shifts will improve the relative uncertainty ($\Delta\nu/\nu$) of transition frequency measurements. Applications include precision measurement of atomic characteristics [28] and physical constants, especially the design for the new Rydberg constant measurement presented in Chapter VIII.

CHAPTER V

Classical Motion in a Modulated Lattice - A Theoretical Study

The unique effects of atomic motion in ponderomotive spectroscopy make this spectroscopy an excellent choice for precision frequency measurements, in both the classical- and quantum-motion regimes. In the classical-motion regime, the unique nature of the atom-field spatial coupling leads to narrow, sub-Doppler features in an excited-state spectrum.

Previous theoretical work has examined the inelastic ponderomotive interaction between a dynamically-modulated optical standing wave and a stationary Rydberg atom [43]. In this chapter, I describe theoretical work that accounts for atomic motion within a cold atom sample. In Chapter III and Chapter IV, I showed experimentally that first-order, even-parity ($|l'-l| = 0, 2, \dots$) Rydberg transitions could be driven by the ponderomotive interaction acting on Rydberg atoms trapped at lattice intensity minima. Here, I show theoretically that, for magic-condition lattices, the inclusion of atomic motion does not broaden the central resonance line for these even-parity transitions, as would be expected in traditional first-order dipole-field spectroscopy. Equally significant, I demonstrate that atomic motion also enables odd-parity ($|l' - l| = 1, 3, \dots$) transitions to be strongly driven using this scheme, a phenomenon not predicted in stationary-atom calculations.

5.1 Model

In the semi-classical model presented here, I employ a two-level atom (basis set $\{|1\rangle, |2\rangle\}$) in the interaction picture. As introduced in Chapter I, field-induced coupling between the two levels can be described by a Rabi frequency written in phasor form, $\chi(t) = \tilde{\chi}e^{i\delta t}$, where δ is the detuning of the field frequency from the $|1\rangle \rightarrow |2\rangle$ resonance (explicitly defined below) and $\tilde{\chi}$ is a real-valued amplitude. The probability of excitation to state $|2\rangle$ can be determined by solving a set of coupled-amplitude equations, which incorporate $\chi(t)$ (see for example, Subsection 5.2.2 below).

The full atom-field interaction Hamiltonian introduced in Chapter III is given by

$$V_{\text{int}} = \frac{1}{2m_e}\left(2\,|e|\,\mathbf{A}\cdot\mathbf{p} + e^2\mathbf{A}\cdot\mathbf{A}\right), \tag{5.1}$$

where once again, $\mathbf{p}$ is the Rydberg electron's momentum operator, and $\mathbf{A}$ is the vector potential of the light field. When the $\mathbf{A}\cdot\mathbf{p}$ term is used to describe the interaction of a mobile atom having velocity $\mathbf{v}$ with a field having wavenumber $\mathbf{k_\Omega}$, the well-known Doppler effect emerges, such that the Rabi frequency is expressed as $\chi(t) = \tilde{\chi}e^{i(\delta+\mathbf{k_\Omega}\cdot\mathbf{v})t}$. Averaging the resulting detuning-dependent excitation probability over the thermal velocity distribution of an atomic sample leads to a Doppler-broadened and -shifted spectral profile.

On the other hand, as demonstrated below, spectroscopy using the $\mathbf{A}\cdot\mathbf{A}$ (ponderomotive) term features the emergence of sub-Doppler spectral-line profiles, with widths independent of the thermal distribution of the sample. As described in the previous chapters, Rydberg-Rydberg transitions are driven using this spectroscopy by introducing a substantial spatial variation of the field intensity within the volume of the atom and by dynamically modulating the intensity at the transition frequency between the coupled states.

Using a semi-classical model, I assume an ideal one-dimensional standing wave

along the z-direction, amplitude-modulated at a microwave frequency $q\Omega$ (q is an integer). As shown in Reference [43] and Appendix A, the interaction Hamiltonian coupling an atom in a bound Rydberg state $|1\rangle = |n, l, m\rangle$ to a bound Rydberg state $|2\rangle = |n', l', m'\rangle$ in a two-level system is expressed by

$$V_1^2 = V_p \left[\frac{1}{2} + \sum_{q=1,3,\ldots}^{\infty} \mathrm{J}_q \left(\frac{\pi V_\mu}{V_\pi} \right) \sin(q\Omega t) \right] \times \left[\sum_{p=|l'-l|,|l'-l|+2,\ldots}^{\infty} \frac{(2k)^p}{p!} (-1)^{(p+\sigma)/2} (r_e^p)_{n,l}^{n',l'} (\cos^p \theta_e)_{l,m}^{l',m'} \right] \begin{cases} \cos(2k\tilde{z}) + \delta_{0,p} & p \text{ even} \\ \sin(2k\tilde{z}) & p \text{ odd} \end{cases}, \tag{5.2}$$

where $\sigma = 0$ ($\sigma = 1$) for even (odd) $|l' - l|$ transitions. Note that the variable p describes the parity of a transition. For example, $p = |l' - l| = 2$ describes an even-parity transition between an initial state with angular-momentum l and a final state with angular momentum $l' = \pm 2$.

Here, as in previous chapters, V_p is the free-electron ponderomotive potential $e^2|E_0|^2/(4m_e\omega_L^2)$, E_0 is the peak electric-field amplitude of the optical standing wave, $k = (\omega \pm q\Omega)/c \approx \omega/c$ is the wavenumber of the optical beams constructing the standing wave, $\tilde{z}$ is the instantaneous center-of-mass location of the Rydberg atom (origin coincident with a standing-wave intensity maximum), and r_e and θ_e are the radial and polar relative coordinates, respectively, of the Rydberg electron with respect to the atomic core. The first term in brackets contains the parameters for dynamic amplitude modulation using an electro-optic modulator with an offset voltage set to $V_\pi/2$. The voltage ratio V_μ/V_π controls the modulation amplitude around the offset (see Appendix A for details).

In this model, the fundamental modulation frequency $q = 1$ is selected. Detuning is defined as $\delta = \Omega_0 - \Omega$, where Ω_0 is the resonance frequency of the $|1\rangle \rightarrow |2\rangle$

transition. Throughout this chapter, δ represents an angular frequency unless explicitly expressed in units of Hz. The rotating-wave approximation is employed, and Equation 5.2 is re-written in the form $V_1^2 = \hbar\chi(t)$ to obtain

$$\chi(t) = \frac{X}{2} e^{i(\delta t + \frac{\pi}{2})} \begin{cases} \cos(2k\tilde{z}) & p \text{ even} \\ \sin(2k\tilde{z}) & p \text{ odd} \end{cases} . \tag{5.3}$$

This expression has been derived following the procedure presented in Appendix A, in which non-contributing DC terms have been omitted and

$$X = \frac{V_p}{\hbar} \mathrm{J}_1 \left(\frac{\pi V_\mu}{V_\pi} \right) \left[\sum_{p=|l'-l|,|l'-l|+2,\ldots}^{\infty} \frac{(2k)^p}{p!} (-1)^{(p+\sigma)/2} (r_e^p)_{n,l}^{n',l'} (\cos^p \theta_e)_{l,m}^{l',m'} \right] . \tag{5.4}$$

5.2 Methods

5.2.1 Center-of-mass motion

To introduce center-of-mass motion of the atom relative to the standing wave, the ideal case is assumed wherein the atomic trajectory is along the standing-wave axis during the interaction time τ. The atomic center-of-mass velocity v is perturbed as the atom moves through the sinusoidal lattice potential and satisfies the coupled equations $\dot{\tilde{z}}(t) = v(t)$ and $\dot{v}(t) = \frac{V_{\mathrm{av}} k}{M} \sin(2k\tilde{z}(t))$. Here, M is the atomic mass, and V_{av} is the average potential depth for states $|1\rangle$ and $|2\rangle$, given by $V_{\mathrm{av}} \approx \frac{1}{2}(\langle V_2^2(\tilde{z})\rangle + \langle V_1^1(\tilde{z})\rangle)$, and the angled brackets indicate a time average. Experimentally, this value is set near V_{av} =10 MHz for Rydberg atoms with a mean temperature T =100 μK [27]. I use the fourth-order Runge-Kutta method to solve these coupled equations.

In Figures 5.1e and 5.1j, for example, I show one-dimensional velocity trajectories seeded with a Maxwell-Boltzmann distribution of initial velocities and an initial position of $z_0 = \lambda/4$, at a lattice intensity minimum. In a case such as Figure 5.1e,

many trajectories approach a harmonic-motion limit, whereas in Figure 5.1j, many trajectories approach a constant-motion limit.

5.2.2 Coupled-amplitude equations

In these simulations, the coupled-amplitude equations for the basis set $\{|1\rangle, |2\rangle\}$ satisfy the following as $dt \to 0$:

$$c_1(t+dt) = c_1(t) - \frac{i}{2} X e^{-i(\delta t + \pi/2)} c_2(t) dt \begin{cases} \cos(2k\tilde{z}) & |l'-l| \text{ even} \\ \sin(2k\tilde{z}) & |l'-l| \text{ odd} \end{cases}, \tag{5.5}$$

and

$$c_2(t+dt) = c_2(t) - \frac{i}{2} X e^{i(\delta t + \pi/2)} c_1(t) dt \begin{cases} \cos(2k\tilde{z}) & |l'-l| \text{ even} \\ \sin(2k\tilde{z}) & |l'-l| \text{ odd} \end{cases}. \tag{5.6}$$

In Figures 5.1 through 5.3, it is assumed that the atom-field interaction has a temporal Gaussian envelope with a full-width-half-max of τ. The excited-state population $|c_2(\tau)|^2$ is calculated using Equation 5.5 and Equation 5.6 for a range of initial velocities v_0 and positions z_0. To obtain $\langle |c_2(\tau)|^2 \rangle$, a weighted average of $|c_2(\tau)|^2$ over v_0 is performed, using a Maxwell-Boltzmann distribution. A uniform average over initial position z_0 is also performed, using the range $\lambda/8 \leq z_0 \leq 3\lambda/8$. Unless otherwise specified, $X/2 = (\pi/2)/\tau$, such that the full interaction time in the limit of $v \to 0$ yields a π-pulse.

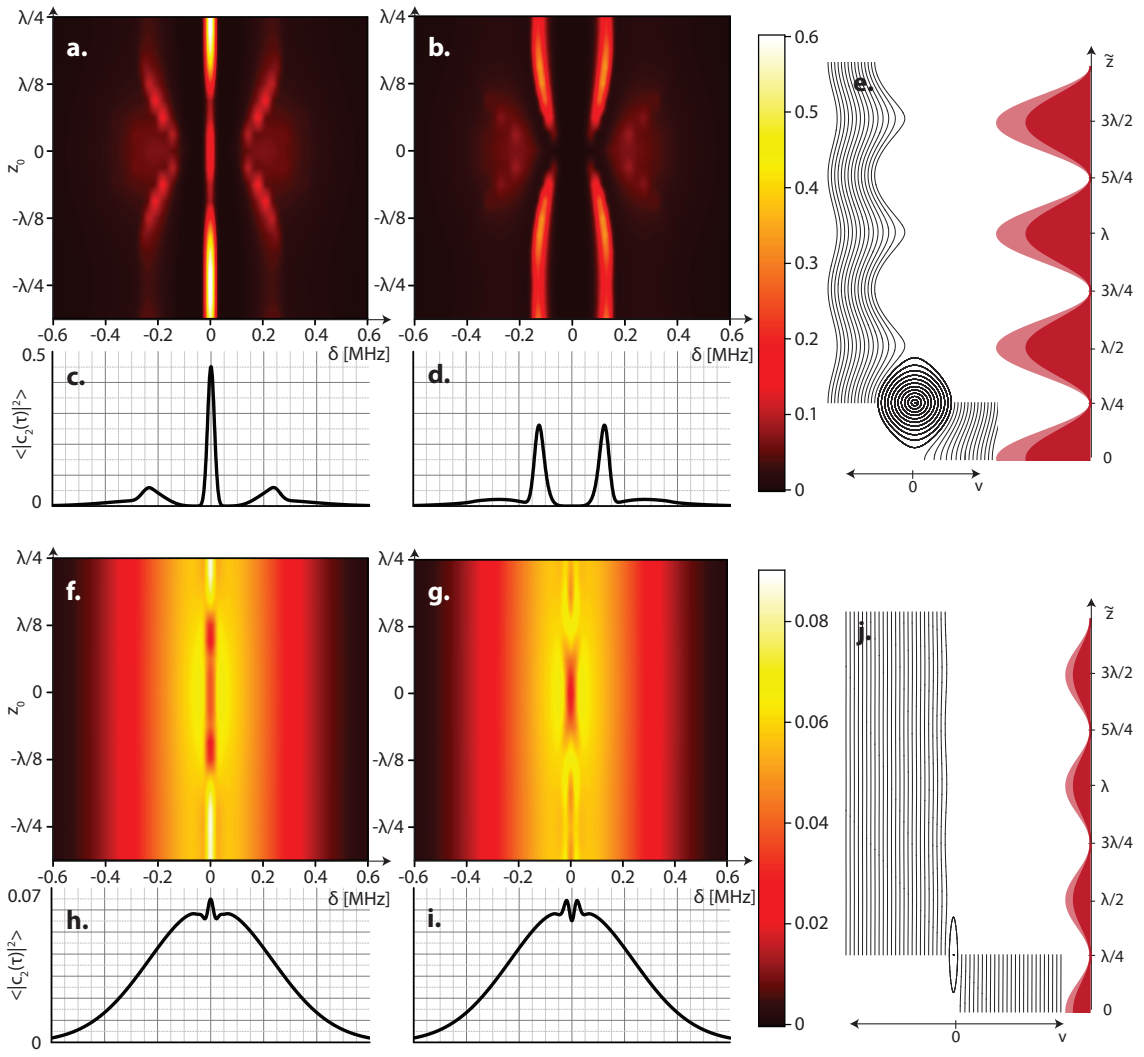

Figure 5.1: **Excited-state spectra as a function of detuning δ for T = 100 μK, τ = 20 μs.** (a)-(e) V_{av}=2500 kHz. (f)-(j) V_{av}=25 kHz. (a),(f) Even-parity and (b),(g) odd-parity cases spanning -10$\lambda/32 \leq z_0 \leq 8\lambda/32$. (c),(h) Even-parity and (d),(i) odd-parity cases averaged over $\lambda/8 \leq z_0 \leq 3\lambda/8$. (e),(j) Sample atom trajectories relative to the standing-wave intensity pattern. These results show the attainment of odd-parity transitions, as well as the preservation of narrow central spectral-line features in the limit of a shallow lattice.

5.3 Discussion

5.3.1 Numerical results

The spatial dependence in the Rabi amplitude, given by $\tilde{\chi} = (X/2)\cos(2k\tilde{z})$ or $\tilde{\chi} = (X/2)\sin(2k\tilde{z})$ in Equation 5.3, is a unique feature of $\mathbf{A}\cdot\mathbf{A}$ (ponderomotive) spec-

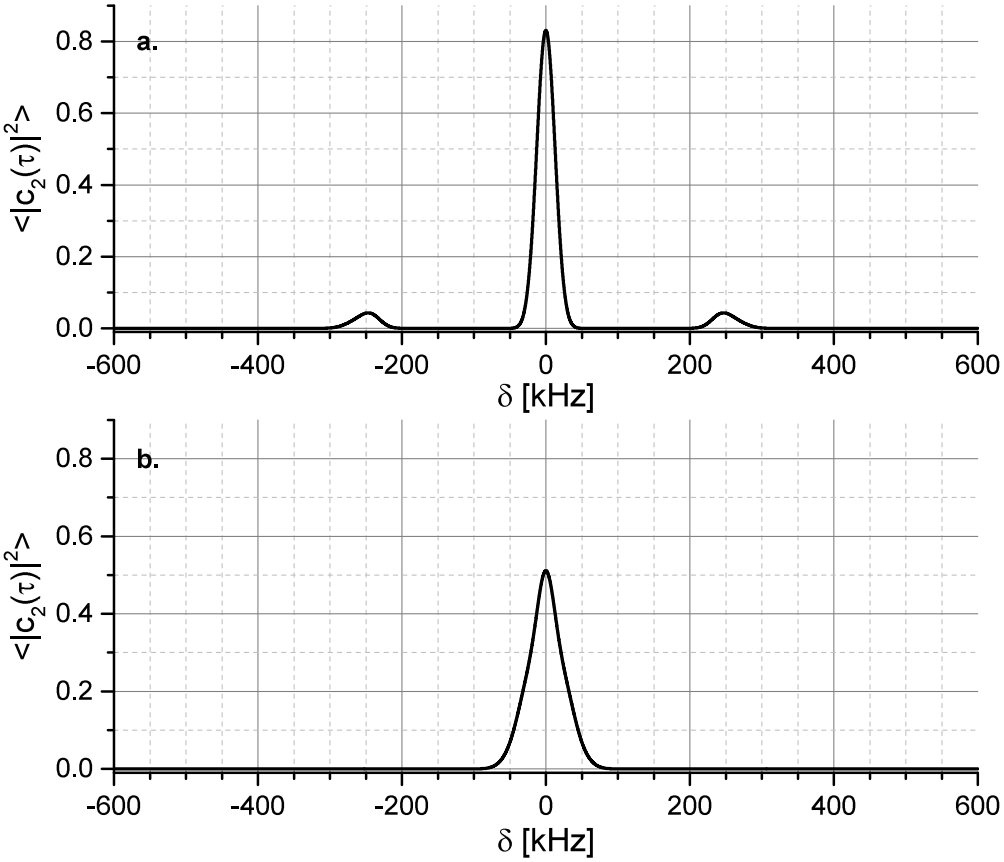

Figure 5.2: **Excited-state spectra as a function of detuning δ, averaged over $\mathbf{v_0}$ and $\mathbf{z_0}$, for $\mathbf{T = 1}$ μK, $\tau = 20$ μs, even-parity case.** (a) $V_{\rm av}$=2500 kHz. (b) $V_{\rm av}$=25 kHz. See text for details.

troscopy. For example, spectroscopy using the $\mathbf{A} \cdot \mathbf{p}$ interaction commonly contains a spatial dependence in the phase of the Rabi frequency, but not the amplitude. Because I am considering mobile atoms with a time-dependent position $\tilde{z}(t)$, the resulting ponderomotive Rabi frequency then has, in general, both a time-dependent amplitude and phase. This characteristic leads to coupled-amplitude equations (Equation 5.5 and Equation 5.6) for which analytical solutions do not exist. Therefore, I have solved the coupled-amplitude equations exactly using the numerical methods outlined above. The atomic center-of-mass motion has been treated classically, which is a reasonable treatment for cold atoms trapped in a deep lattice (as is the case with $V_{\rm av} = 2500$ kHz, used in many of the simulations). For the case of $V_{\rm av} = 25$ kHz, the other lattice

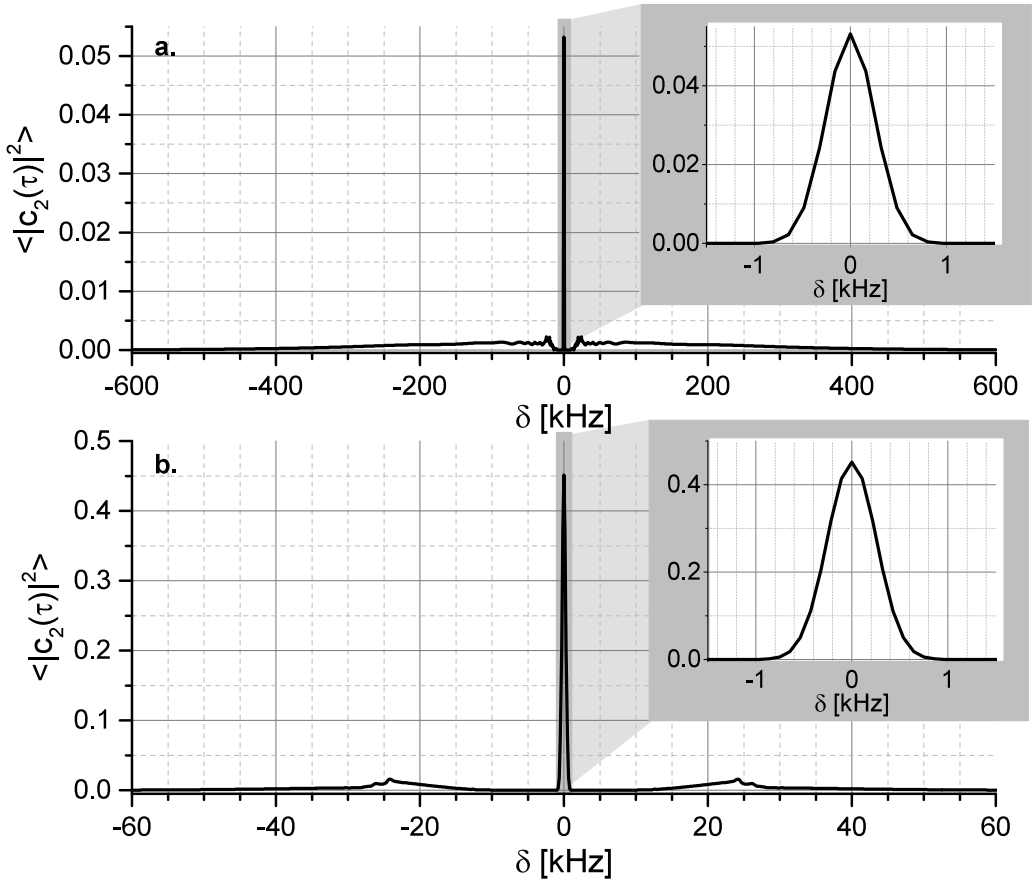

Figure 5.3: **Excited-state spectra as a function of detuning δ, averaged over $\mathbf{v_0}$ and $\mathbf{z_0}$, for $\tau = 1000$ μs, $\mathbf{V_{av}}$=25 kHz, even-parity case.** Note that the horizontal axes differ in scale. (a) $T = 100$ μK. (b) $T = 1$ μK. The insets show Fourier-limited central lines at this long interaction time τ, differing only by signal strength (due to differing atom temperatures).

depth used in the simulations, $V_{\rm av}$ is only about three times the recoil energy, and so classical-motion results must be compared with quantized-motion results at that lattice depth.

In Figures 5.1a, b, f and g, excited-state population is mapped as a function of detuning δ on the x-axis and initial position z_0 on the y-axis, averaged over the Maxwell-Boltzmann velocity distribution for the mean atom-ensemble temperature listed in the figure caption. Spectral lines are displayed below the population maps, depicting a uniform average of the initial position over the range $\lambda/8 \leq z_0 \leq 3\lambda/8$ (representing atoms distributed in a lattice potential well).

Two key features arise from these numerical solutions. The first feature is a Fourier-limited spectral line centered at $\delta = 0$ for the case of even-parity transitions, which are displayed in the plots on the left side of Figure 5.1. As shown in Subsection 5.3.3 below, one way to interpret this velocity-independent linewidth is by examining resonances induced by harmonic-like atomic motion in the lattice well. In that case, it will be shown that the frequencies introduced into the atomic rest frame by the harmonic-like motion are not dependent on velocity and therefore the resonance line is not inhomogeneously broadened by an average over velocity classes.

Another way to interpret the prominent height of the Fourier-limited spectral line at $\delta = 0$, especially for atoms with $z_0 = \lambda/4$, is by considering a unique feature of ponderomotive spectroscopy. Namely, for atoms that remain in a single lattice well $\lambda/8 \leq \tilde{z}(t) \leq 3\lambda/8$ during the interaction time τ, the real part of the Rabi frequency $\chi(t)$ has a constant sign (in this case, negative) during the entirety of the interaction time, regardless of the specific details of the atomic motion. At $\delta = 0$, this leads to a steady population accumulation in the excited state (until saturation), as any atoms in the well contribute to the net pulse area at the $\delta = 0$ resonance. This constant Rabi-frequency phase (i.e. the constant sign of the amplitude) for atoms that remain in a single lattice well, regardless of the details of their motion, is a feature unique to ponderomotive spectroscopy. At $\delta \neq 0$, the problem becomes unsolvable analytically, and the numerical results displayed here must be referenced.

The second key feature observed from the results in Figure 5.1 is the emergence of spectral lines due to odd-parity transitions, displayed in the plots on the right side of the figure. These spectral lines were unexpected. Stationary-atom calculations [43] had previously indicated that a frequency-modulated lattice, rather than an amplitude-modulated lattice, would be required to drive odd-parity atomic transitions using the ponderomotive interaction. As shown in Subsection 5.3.3 below, one way to interpret the emergence of these spectral lines is by showing that harmonic-like

atomic motion in the lattice well introduces the needed frequency-sidebands onto the lattice modulation in the rest frame of the atom.

Other even-parity results have been calculated for colder, 1-μK atoms (Figure 5.2) and longer, 1-ms interaction times (Figure 5.3). The latter case is important because it demonstrates a Fourier-limited spectral line at a long interaction time that approaches the interaction time ($\sim$ 10 ms) that will be used for the Rydberg constant measurement.

In the sections below, I make two approximations to the classical atomic motion in this system in an attempt to analytically interpret the multiple resonances (multiple spectral lines) observed in the exact numerical results displayed in Figures 5.1 through 5.3.

5.3.2 Constant-motion approximation

Some features in the exact numerical results may be explained by atoms traveling at a near-constant velocity (i.e. atoms for which the lattice potential induces only a small perturbation on the atomic motion, as in Figure 5.1j). In this case, the instantaneous position of the atom, $\tilde{z}(t)$, may be approximated as $\tilde{z}(t) = z_0 + v_0 t$. Here, z_0 represents initial position, and v_0 represents a constant center-of-mass velocity.

Inserting $\tilde{z}(t) = z_0 + v_0 t$ into Equation 5.3 and selecting the even-parity case, Equation 5.3 may be re-written as

$$\chi(t) = \frac{X}{4}\left(e^{i(2k(z_0+v_0t)+\delta t)} + e^{-i(2k(z_0+v_0t)-\delta t)}\right), \tag{5.7}$$

where the global phase has been neglected for simplicity.

By isolating terms in the sum (setting $\chi(t)$ equal to one term in the sum while neglecting the other term), the resulting coupled-amplitude equations can be solved analytically using the standard technique of finding the roots of the characteristic equations for $c_1(t)$ and $c_2(t)$. This technique is outlined in Chapter 2 of Reference [6].

It can then readily be shown that resonance conditions occur at $\delta = \pm 2kv_0$. These two resonance conditions originate from the first-order Doppler effect. The dynamically amplitude-modulated standing-wave field can be re-framed as two pairs of counter-propagating optical beams with frequencies $\omega_1 = \omega + \Omega/2$ and $\omega_2 = \omega - \Omega/2$. As discussed in Chapter III, the atom interaction with this field can be viewed as a difference-frequency $(\omega_1 - \omega_2)$ inelastic scattering process from one beam into a counter-propagating beam. Because there are effectively four fields (due to the two frequencies and two beam directions), there are two resonances per velocity class, regardless of direction.

For atomic ensemble temperatures of $T = 100$ and 1 μK, the most probable first-order Doppler resonances occur at $\delta = 322$ and 32 kHz, respectively. Note that even though Equation 5.7 was derived for even-parity transitions, these Doppler resonances are the same for odd-parity transitions. Additionally, Equation 5.7 is inhomogeneous with respect to velocity class. Therefore, upon averaging over the velocity distribution of the ensemble, line-broadening is observed at these resonances. These broad resonance peaks are especially evident in Figures 5.1 and 5.3.

5.3.3 Harmonic-motion approximation

In contrast to these broad resonance peaks, the narrow spectral lines appearing in the exact numerical results may be explained by the motion of atoms as it is governed by the restoring force of the lattice potential. In the limit of a deep lattice, motion in a lattice potential well is approximated by that of a harmonic oscillator. In other words, the instantaneous center-of-mass position of the atom can be expressed as $\tilde{z}(t) = \zeta \sin(\omega_T t)$, with "trap" frequency $\omega_T = \sqrt{\frac{2V_{\mathrm{av}}k^2}{M}}$ and oscillation amplitude ζ (defined below). In the rest frame of the atom, this periodic motion adds frequency-modulation sidebands onto the amplitude-modulation frequency Ω.

For example, I examine the case of an even-parity transition with $z_0 = \lambda/4$ by

inserting the harmonic-motion approximation for $\tilde{z}(t)$ into Equation 5.3. Then, Equation 5.3 may be re-written as

$$\begin{aligned}\chi(t) &= \frac{X}{2}e^{i\delta t}\cos(2k\zeta\sin(\omega_T t)) \\ &= \frac{X}{2}e^{i\delta t}J_0(2k\zeta) + e^{i\delta t}\sum_{n=1}^{\infty}J_{2n}(2k\zeta)\left(e^{i2n\omega_T t}+e^{-i2n\omega_T t}\right). \end{aligned} \tag{5.8}$$

Here, $\zeta = \sqrt{\frac{Mv_0^2}{2V_{\rm av}}}\frac{1}{k}$ is the amplitude of oscillation for $z_0 = \lambda/4$ and some initial velocity v_0. The global phase has been omitted for simplicity. Using the same technique as Subsection 5.3.2 to identify resonance conditions, it can be shown that resonances occur at $\delta = 0$ and $\delta = \pm 2n\omega_T$ in this approximation.

For the examples of $V_{\rm av} = 2500$ and 25 kHz used in this chapter, the $n=1$ trap-frequency resonance occurs at $\delta = 288$ and 28.8 kHz, respectively. These resonances can be observed in the numerical results. In Figures 5.1f and g, these trap-induced resonances appear on top of broad Doppler profiles and are somewhat distorted and closer to the origin than predicted due to anharmonicity effects. In Figure 5.2a, the sidebands are resolved from the carrier linewidth (centered at $\delta = 0$), whereas in Figure 5.2b, the sidebands are not resolved and increase the perceived linewidth of the carrier. The amplitudes of the sidebands are dependent on v_0, and in general on z_0. The resonance frequencies of the sidebands are dependent on ω_T and also on the harmonicity of the trap. Averaging over the initial velocities and positions of atoms in an ensemble introduces inhomogeneous broadening to the sidebands only due to differing degrees of anharmonicity.

For the odd-parity case, a similar procedure may be used to reveal resonances at $\delta = \pm(2n-1)\omega_T$. Here, $n=1$ trap-frequency resonances occur at $\delta = 144$ and 14.4 kHz for trap depths of $V_{\rm av} = 2500$ and 25 kHz, respectively. These resonances can be seen as sharp spectral lines in Figure 5.1. The spectral lines are slightly distorted from

symmetric, Fourier-limited line profiles due to anharmonicity effects. Therefore, the interaction of an amplitude-modulated standing wave and a Rydberg atom possessing harmonic-like motion opens up the possibility of driving odd-parity transitions, by way of introducing frequency-modulation sidebands in the rest frame of the atom.

It should be stressed that the resonances derived in this section and the last section are the results of approximations. To examine the exact solution to the coupled-amplitude equations listed in Subsection 5.2.2, the numerical results presented in Figures 5.1 through 5.3 must be utilized.

5.4 Outlook

The numerical results presented in this chapter are based on a semi-classical model. Ongoing work is being done to investigate quantized center-of-mass motion in this system, to determine whether transitions may be driven between motional states in a lattice via the ponderomotive interaction. Future experimental work will also investigate using the lattice-modulation scheme described in this dissertation to drive odd-parity transitions, an exciting prediction of the work presented in this chapter. Finally, the proposed Rydberg-constant measurement experiment described in Chapter VIII will utilize the Doppler-free, $\delta = 0$ feature of even-parity transitions driven via ponderomotive spectroscopy to drive a Rydberg-Rydberg transition from which a new measurement of the Rydberg constant will be extracted.

In the next two chapters, I shift focus and discuss the design work and experimental results for a precision measurement that utilized a different kind of spectroscopy, microwave spectroscopy, to drive Rydberg-Rydberg transitions.

CHAPTER VI

System Design for Precision THz Spectroscopy of Rydberg Atoms

In this chapter, I describe the overall design process for a cold-atom system that I designed and built over the course of nine months. This ultra-high-vacuum chamber and optics system was designed to perform multi-purpose, cutting-edge precision spectroscopy experiments with Rydberg atoms, with a focus on THz-based measurements.

This system is not the Rydberg-constant measurement system (which is presented in Chapter VIII). Rather, it is a set-up for auxiliary precision-measurement experiments. However, the first experiment done in this chamber was a precision measurement to lay further groundwork for the Rydberg constant measurement, as described in the next chapter.

First, I will briefly outline the cooling and trapping mechanism in this cold-atom system. Then, I will describe design features of the in-vacuum electrode package that are especially unique or significant for future precision-measurement experiments.

6.1 Atom cooling and trapping

A photo of the main vacuum chamber is displayed in Figure 6.1e. This two-MOT system utilizes a primary MOT stage (not shown) to both reduce the initially-hot velocity of atoms and shield the final cold-atom sample from untrapped hot atoms. In this system, I designed the primary MOT stage to be a pyramidal atom-beam MOT, which is a variant of a LVIS ("low-velocity intense source of atoms") [63]. This is a fairly common, robust design in which a large-diameter (about 2 inches), circularly-polarized laser beam is directed onto an in-vacuum square-pyramidal, concave mirror. The mirror has a small (1-2 mm) aperture at its center. With the addition of external anti-Helmholtz coils, hot ($\gtrsim$300 m/s) atoms from a nearby rubidium (Rb) dispenser are cooled via radiation pressure and compressed transversely. In the direction orthogonal to the mirror, there is a radiation pressure imbalance due to the aperture. Therefore, cooled atoms traverse through the aperture into the main chamber, where they are once again captured in a traditional six-beam MOT, the design process for which was described in Chapter III.

6.2 In-vacuum electrode package

For precision measurements, the ability to control electric fields in three dimensions is critical to avoid unwanted Stark shifts in atomic energy-interval measurements. This is best accomplished by enclosing a cold-atom sample within an electrode package (Figures 6.1d and f), which is itself mounted inside the (grounded) vacuum chamber.

6.2.1 Plate electrodes

I designed the package with three pairs of orthogonal plates, the DC voltages of which can be controlled independently. To increase the versatility of the package,

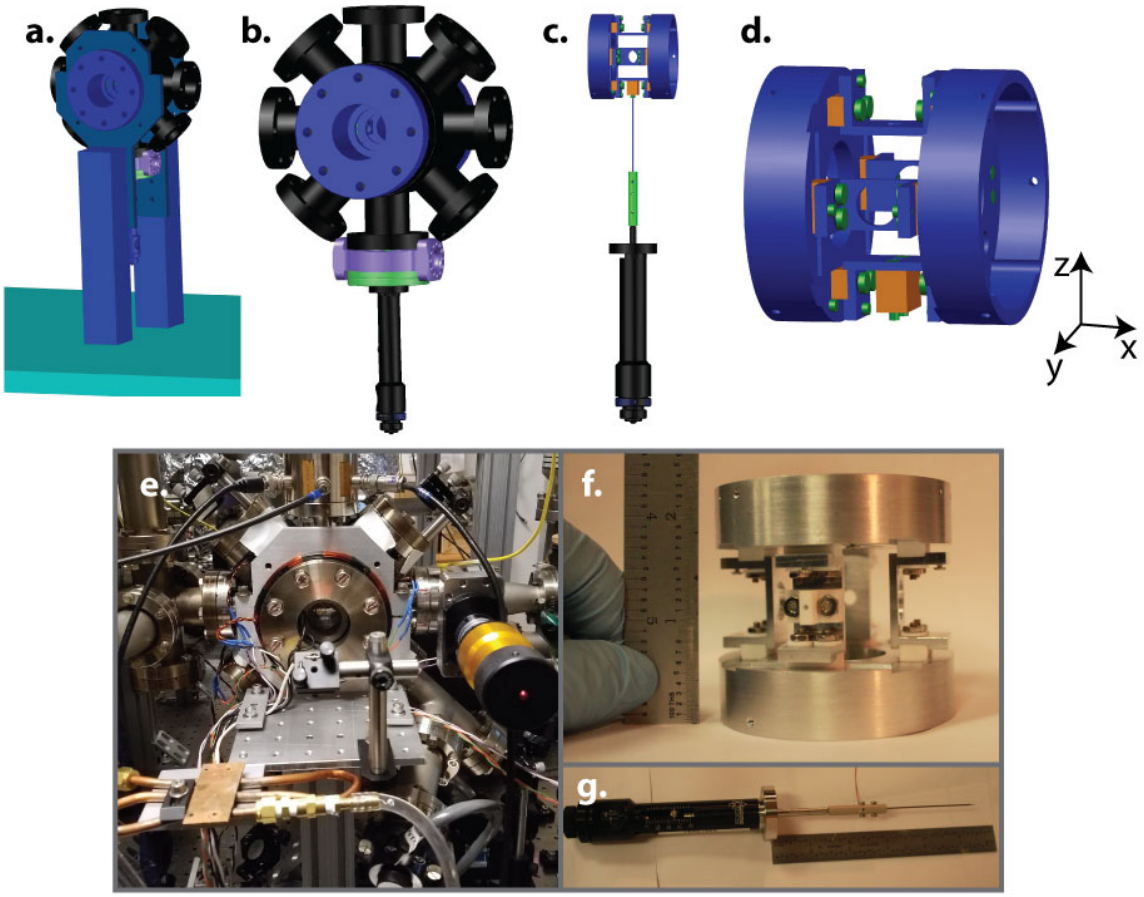

Figure 6.1: **THz spectroscopy vacuum system design.** (a)-(d) AutoCAD designs for the vacuum system. (e)-(g) Photos of the finished system. (a),(b),(e) Assembled system displaying the main vacuum chamber, which features large re-entrant windows for close optical and THz access to the spectroscopy region from outside vacuum. In (b), the handle of the retractable needle electrode is displayed mounted to the bottom of the chamber. (c) Side view of the electrode package, picturing the needle electrode in its retracted position. (d),(f) Close-up view of the three-dimensional electrode package. In the AutoCAD design, blue represents aluminum material, orange represents machinable ceramic, and green represents screws (the heads of which are electrically insulated from the electrode plates). (g) Photo of the needle electrode.

I also included the ability to generate radio frequencies (RF) (100-MHz-range) in-vacuum by applying opposing RF phases to the two plate electrodes along the y-direction (as defined in Figure 6.1d).

The geometry of this electrode package was constrained by a number of considerations. A major constraint was the dimensions of the vacuum chamber, which had an $\sim$11-cm inner diameter. The plates of the package also required apertures to permit

optical access to the cold-atom sample for MOT light (1-2 cm), Rydberg-preparation laser beams, and THz probe waves, as well as an aperture to permit the passage of electrons from the probe region to the MCP for detection. Finally, to make this a multi-purpose system, I included an in-vacuum retractable needle electrode (see Subsection 6.2.2), for which an additional, small aperture in a plate electrode was needed.

These geometrical requirements were further constrained by the need to generate (1) high voltage for detection via state-selective field ionization (SSFI) and (2) a homogeneous electric field at the location of the atoms. The first constraint was an issue because the voltage source used to generate SSFI voltage ramps is limited to a maximum output of about ± 450 V by internal high-voltage operational amplifiers, which represent state-of-the-art models. The classical ionization field for Rydberg atoms goes as $1/n^2$ (Equation 1.6), and a range of $n = 30$ to $n = 70$ is desired. For detection of $n \approx 30$ atoms, ionization fields of ~ 400 V/cm will be needed. Therefore, ionization electrode plates could be separated by no further than a few cm (assuming a differential voltage of 900 V). In the final design, the plate separation was 3 cm.

The second constraint was an issue because the apertures in the plates could lead to unwanted fringe effects and field gradients in the center of the package. To address this, I simulated my AutoCAD model using a finite-element analysis. In Figure 6.2, I display the results. The figure shows bisections of the electrode package by two orthogonal planes, defined by the coordinate axes in the figure. The $x-y$ plane gives the same result as the $x-z$ plane due to symmetry (neglecting small differences in aperture sizes). It can be seen from the figure that the contour lines are nearly linear (and thus field divergence is small) within the center $(0.5 \text{ cm})^2$-region of each 2-D plot (red rectangle), which is a reasonable region in which to generate the ($\lesssim$ mm-scale) MOT. Therefore, this electrode package design is suitable for applications requiring field homogeneity, such as field zeroing (see Chapter II).

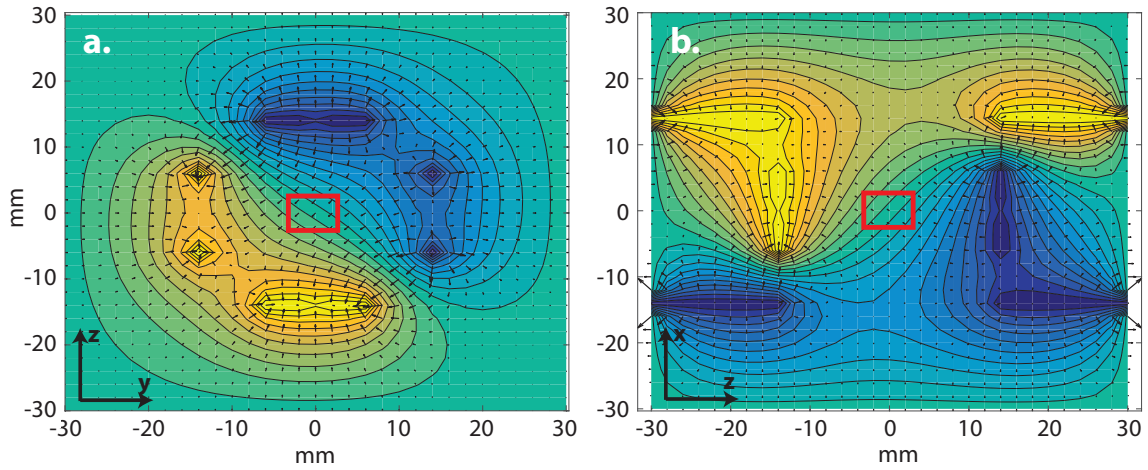

Figure 6.2: **Simulations of the electric field in the spectroscopy region due to the plate electrodes.** These simulations indicate that with the electrode design, the field is approximately linear in the center of the electrode package (the location of the atoms). The blue and yellow regions represent electrode plates held at fixed voltages of +1 V and -1 V, respectively. Typical voltages applied for field-zeroing are 1-2 orders of magnitude less than this. The contour lines have a 0.1 V spacing. The overlaid arrows indicate the magnitude and direction of the resulting electric field. The red rectangles outline the center $(0.5\text{ cm})^2$-regions of each contour plot. The contour plots show results from planes bisecting the electrode package, as defined by the coordinate axes in (a) and (b).

6.2.2 Needle electrode for THz imaging

The final piece in the electrode package is a retractable needle electrode, shown in Figures 6.1b and g. This needle electrode represents the opposite end of the field-homogeneity spectrum from plate electrodes. The needle electrode provides an option for experiments in which strong field gradients [64] or radiation amplification effects are desired. The electrode is a beryllium copper needle with a 125-μm-diameter tip. The electrode may be extended to slightly beyond the center of the electrode package (the location of the atoms) and may be retracted back beyond the plate electrode surface. The needle electrode has been positioned opposite the MCP aperture so that it can be used in a charge-imaging detection scheme if desired. In this way, when a high voltage is applied to the needle, it acts as an effective point source. When Rydberg atoms are ionized, the charges follow the diverging field lines to the

MCP, forming a magnified image and preserving their original location [64]. Future experiments could use this feature to spatially map microscopic Rydberg-Rydberg interactions or for THz imaging. In THz imaging, passive (e.g. blackbody radiation) or active THz radiation could be used to image a source onto a cold Rydberg-atom sample, which itself acts as a very sensitive, position-dependent detector.

6.3 Outlook

In addition to THz imaging, an ongoing project in this system is exploring Rydberg-Rydberg molecules formed from atoms in opposite-parity Rydberg states.

In the next chapter, I describe an experiment I completed in this system in which I performed a high-precision measurement of the quantum defect of a high-angular-momentum state in Rb. The technique used for that measurement can be replicated to measure other high-angular-momentum-state defects. Together, these measurements are required to extract a more precise value of the Rb core polarizability (introduced in Chapter I), which is currently one of the dominant uncertainties in our future Rydberg constant measurement (Chapter VIII).

CHAPTER VII

Precision Measurement of Rb ng-series Quantum Defect using sub-THz Radiation

7.1 Introduction

In an alkali atom such as rubidium (Rb), the interaction between the ionic core of the atom and the valence electron depresses the energy levels of the valence electron below the expected hydrogenic levels, resulting in a quantum defect (see Chapter I). In cold-atom precision spectroscopy, alkali species are commonly used in place of hydrogen because alkali atoms are easier to laser-cool, due to a lower recoil energy and near-infrared cooling transition. Therefore, it is imperative to precisely quantify the quantum defects for alkali-species atoms. In this chapter, I present the results of a measurement of the high-angular-momentum ng-series quantum defect of Rb. For electrons in high-angular-momentum states, the quantum defect is dominated by the polarizability of the ionic core, which may be extracted from high-angular-momentum defect measurements. In the most recent experimental measurement of the ng-series quantum defect, microwave spectroscopy of $nd \rightarrow (n+1)g$ transitions [19] was performed, whereas I use sub-THz spectroscopy to measure $ng \rightarrow (n+2)g$ transitions in a field-free environment. This two-photon transition depends only on one set of quantum defects. I measure the ng-series δ_0 and δ_2 quantum defects of ^{85}Rb

with a precision improved by one order of magnitude each, better characterizing this hydrogen-like species for future precision measurements.

7.2 Methods

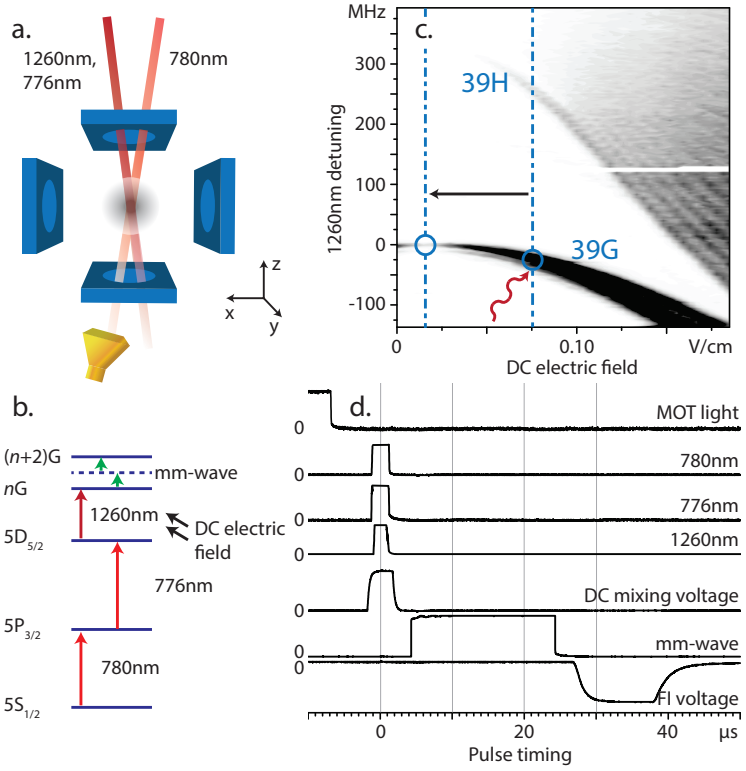

Figure 7.1: **Sketch of the experimental set-up.** (a) Electrode, laser, and microwave-horn configuration. The two y-electrodes present in the experiment are not pictured. (b) Level diagram of excitation scheme. (c) Experimental Stark map demonstrating the preparation of $39g$ population. Black indicates high (>40) Rydberg counts per detection cycle. The preparation consists of optical excitation of a DC-field-perturbed ng state (red squiggly line) and subsequent ramping of the DC field to zero (black arrow). (d) Partial timing diagram of experiment. Full experimental period is 5 ms and includes MOT loading time, not pictured here.

In Figure 7.1a I show the experimental set-up. Atoms are laser-cooled and trapped in a magneto-optical trap (MOT). During each experimental cycle, I prepare atoms in an initial Rydberg ng state via an on-resonant three-stage optical excitation under simultaneous application of a perturbative DC electric field. The weak DC field

admixes a small nf character into the ng state, allowing the single-photon $5d \rightarrow ng$ optical transition (Figures 7.1b and d). As can be seen from the experimental Stark map example shown in Figure 7.1c, significant population is obtained in the initial Rydberg ng state, well-isolated from the neighboring nh state and the hydrogenic manifold. After state preparation, the perturbative DC electric field is adiabatically lowered (Figure 7.1d) to the pre-determined zero-field value, thereby producing a sample of pure ng-state atoms. Next, a rectangular microwave pulse is applied for $\tau = 40$ μs, driving the ng-state atoms into the $(n+2)g$ state. The microwave frequency is scanned across resonance and the $(n+2)g$ target-state population is detected via SSFI (see Chapter II).

In the microwave system, microwaves are first generated in a synthesizer (Agilent N5183A). Next, they are frequency-quadrupled in an active frequency multiplier (Norden Millimeter N14-4680). Finally, because this multiplier accepts a limited range of input power from the generator, the output intensity at the location of the atoms is either increased or attenuated by removing or inserting a waveguide or layers of attenuating foam. I monitor the response of the atoms by taking a data series in which I systematically vary the power output from the synthesizer. For each of these "power" series, I apply an intensity range such that the signal amplitude is indiscernible from the noise floor up until the signal is severely broadened or until I have spanned the available multiplier input range.

I measure the sub-THz energy intervals for four choices of n. For each interval, I take six data series. Five of the series are to evaluate systematics, as outlined in the following sections, and the final, longer data series is averaged to produce a measurement result with low statistical uncertainty.

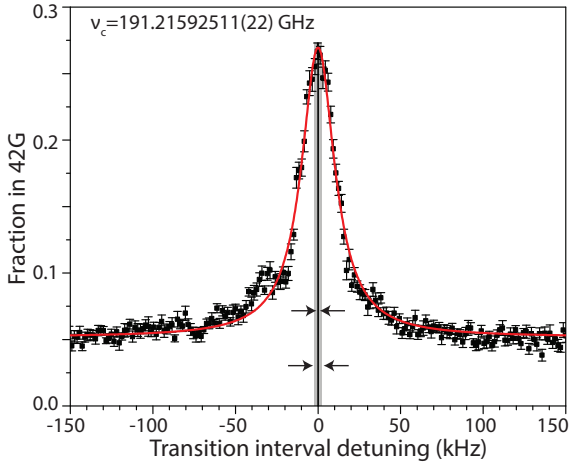

Figure 7.2: **Statistical average of final data set for the 40g→42g transition.** Black squares, fraction of atoms detected in $42g$, detuned from ν_c (black line). The statistical uncertainty on ν_c is less than the width of the black line. Uncertainty on the final corrected interval frequency (gray region), listed in Table 7.2, reflects systematic uncertainty. Error bars on data points, standard error of the mean (SEM). Red curve, Lorentzian fit. In the figure, the systematic corrections exhibited in Table 7.1 have not yet been applied to ν_c.

7.2.1 Statistical uncertainty evaluation

By averaging many data sets in the absence of systematic drift, I observe a Fourier-limited sinc^2-shaped spectral peak centered on resonance at ν_c (Figure 7.2). For the microwave-interaction time τ, the expected Fourier-sideband zeros at $m \times 25$ kHz (m is a nonzero integer) coincide with local minima observed in the spectrum. However, these sidebands are not well-resolved. Since a sideband-averaged sinc^2 function approaches a Lorentzian, I perform each peak fit using a Lorentzian function. I achieve a statistical uncertainty of the line centers on the 100-Hz level. Since the frequencies ν_{n_1,n_2} of the transition intervals (as defined in Equation 7.3) exceed 0.1 THz, this amounts to a relative uncertainty of 10^{-9}.

In order to achieve this precision, it was critical to lock the internal crystal oscillator of the microwave synthesizer to a factory-calibrated, external atomic clock (SRS 725) with a relative internal uncertainty of $\pm 5 \times 10^{-11}$ (when not synchronized to a GPS signal). The absolute instrument uncertainty for the measured $ng \rightarrow (n+2)g$

frequency interval is ≈ 10 Hz. This instrument uncertainty is well below systematic uncertainties.

The only exception is the $40g \rightarrow 42g$ frequency-interval measurement, for which I used a different atomic clock (DATUM LPRO) because the SRS 725 was not available. Maximum aging puts the LPRO relative clock uncertainty at 10^{-9}, with unknown calibration. I have determined the LPRO clock shift by beating the LPRO clock with the calibrated SRS 725 used in the other data. I have determined that the LPRO runs faster by a relative amount of 2.53×10^{-8}, showing that a correction of the clock shift is important. The frequency correction applied to the $40g \rightarrow 42g$ measurement that results from the LPRO clock shift is explicitly listed in Table 7.1.

7.2.2 Systematic uncertainty evaluation

In this experiment, systematic uncertainties include shifts in the resonance frequency due to atom perturbations, e.g. from external fields or other Rydberg atoms.

I have specifically chosen to probe $\Delta l = 0$ ($\Delta j = 0$) transitions in order to eliminate broadening due to the MOT or other external magnetic fields.

As described in Chapter VI, I have isolated the system such that static electric fields are controlled in three directions (see Table 7.1). These field zeros are determined by varying the field direction in question while holding the other directions static until a minimum shift of the transition ν is observed, determined by fitting the measured center transition frequencies versus the DC tuning voltage to a parabola. The uncertainty in the parabolic fit determines the resulting uncertainty in the residual DC Stark shift contributed by the direction in question.

I have timed the excitation sequence such that optical light is not present during the measurement interval, eliminating optical AC Stark shifts (see Figure 7.1d).

The microwave intensities at the atom location are unknown due to nonlinearities in the frequency multiplier and other unknowns in the system. For that reason, I have

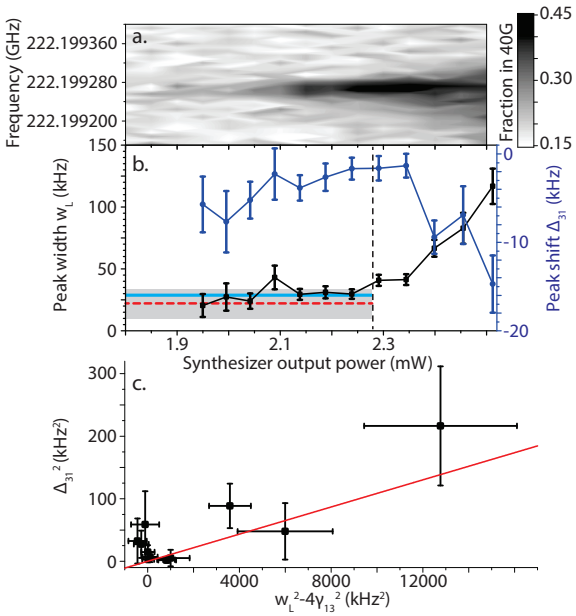

Figure 7.3: **AC Stark shift analysis for the 38g→40g transition.** This analysis is representative of the procedure used for all measured transitions. (a) Power map displaying synthesizer power as a function of interval frequency. Power broadening is evident. (b) Plot of measured peak widths (w_L; black squares, left axis) and peak center-frequency shift (Δ_{31}; blue circles, right axis) versus synthesizer power. Expected Fourier limit γ_F (red horizontal dashed line) ±50% (gray region) and $2\gamma_{13}$ (thick cyan line) are also displayed. Data points to the left of the vertical dashed line contribute to $2\gamma_{13}$. (c) Δ_{31}^2 as a linear function of $w_L^2 - 4\gamma_{13}^2$. Black squares, data points. Red line, linear fit. In (a)-(b), note that synthesizer output power is not linearly proportional to microwave intensity at the location of the atoms. In (b)-(c), Δ_{31} is detuned from the final measured value in Table 7.2. All error bars, propagated from standard errors of peak fits (Lorentzian model).

determined the AC Stark shift (and corresponding uncertainty) for each measured transition by analyzing the relationship between the power-broadened peak width and center frequency location as the microwave intensity is varied (Figure 7.3a). As the full-width-half-maxima w_L of the Lorentzian spectral profiles broaden as a function of microwave power, microwave-induced AC Stark shifts of the transition frequency Δ_{31} become evident. I observe this relation experimentally (Figure 7.3b).

Using density matrix formalism [6] for a two-photon transition between lower state $|1\rangle$ and upper state $|3\rangle$,

$$\Delta_{31} = \left(\frac{\beta}{\kappa}\right)\sqrt{\frac{\gamma_3}{\gamma_{13}}}\left(w_L^2 - 4\gamma_{13}^2\right)^{1/2}. \tag{7.1}$$

Here, β/κ represents the ratio between the AC Stark shifts of the transition (β) and the two-photon state-coupling (κ),

$$\frac{\beta}{\kappa} = \frac{\sum_m \left(\frac{|\mu_{3m}|^2\omega_{m3}}{\omega_0^2 - \omega_{m3}^2} - \frac{|\mu_{1m}|^2\omega_{m1}}{\omega_0^2 - \omega_{m1}^2}\right)}{\sum_m \left(\frac{\mu_{3m}\mu_{m1}}{\omega_0 - \omega_{m1}}\right)}, \tag{7.2}$$

where μ_{mn} and ω_{mn} are the dipole matrix element and transition frequency, respectively, between states m and n, and $\omega_0 \simeq \omega_{31}/2$ is the microwave-field frequency. The coherence decay rate of ρ_{13} (γ_{13}) may be written in terms of the decay rate of ρ_{33} (γ_3) using the relation $2\gamma_{13} = \gamma_3 + \Gamma$. Here, Γ is some dephasing rate, in which we include Rydberg-Rydberg interactions, decay channels that do not re-populate state $|1\rangle$, and effects due to the non-adiabatic turn-on of the interaction pulse. For a system where $\Gamma = 0$, $\Delta_{31} \to 0$ as $w_L \to \gamma_3$, the natural linewidth of the transition. However, because the field is not adiabatically turned on (a rectangular pulse of duration $\tau = 40$ μs that reaches maximum amplitude in < 50 ns), the experimental peak widths $2\gamma_{13}$ are dominated by the Fourier transform of the pulse ($\gamma_{\rm F}$=$0.89/\tau$=22.3 kHz).

In order to obtain values for $2\gamma_{13}$ for each transition $|1\rangle \to |3\rangle$, we calculate the weighted average of peak widths in the region within $\pm 50\%$ of $\gamma_{\rm F}$ (Figure 7.3b). Our results are $2\gamma_{38g-40g} = 29.3 \pm 2.1$ kHz, $2\gamma_{39g-41g} = 29.2 \pm 2.0$ kHz, $2\gamma_{40g-42g} = 27.4 \pm 0.4$ kHz, and $2\gamma_{41g-43g} = 25.1 \pm 1.3$ kHz. These are generally slightly higher than $\gamma_{\rm F}$, but largely consistent with each other, indicating the presence of additional sources of dephasing in the system.

For each transition, I use $2\gamma_{13}$ to plot Δ_{31}^2 versus $w_L^2 - 4\gamma_{13}^2$ (Figure 7.3c). The linear relationship is consistent with the prediction of Equation 7.1. Moreover, the cluster of data points near the origin indicates there is very low AC-Stark shift for

peaks of width $\approx 2\gamma_{13}$. Indeed, for each transition, the peak width of the spectrum averaged from the final data set is consistent with $2\gamma_{13}$, and so we take the AC-Stark-shift value to be zero. The shift uncertainty (Table 7.1) is generated from the weighted average of the center frequencies of the data points that contribute to $2\gamma_{13}$.

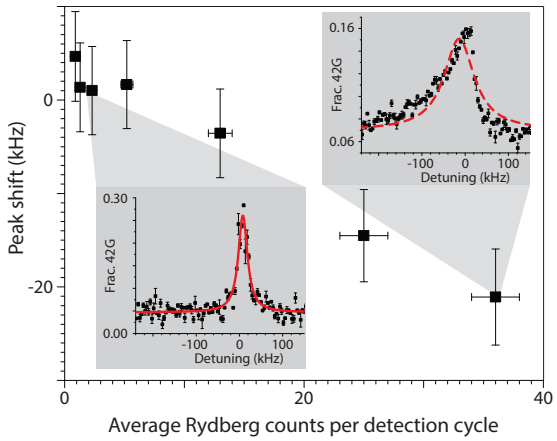

Figure 7.4: **Rydberg-Rydberg shift analysis for the 40g→42g transition.** This analysis is representative of the procedure used for all measured transitions. Data points (black squares) represent measured peak locations versus average Rydberg counts per detection cycle, detuned from the final measured value in Table 7.2. Error bar (y), standard error of fit (Lorentzian model). Error bar (x), standard deviation of counts. Insets, measured resonance peak (black squares) and Lorentzian fit (red curve), detuned from final measured value in Table 7.2. The dashed red curve indicates that a Lorentzian is not an ideal fit function for the asymmetric peak.

Finally, I have identified a maximum number of Rydberg atoms that may be excited per detection cycle without inducing collisional shifts affecting the result, thereby optimizing the signal/noise ratio while minimizing that source of uncertainty. Figure 7.4 shows the measured peak position versus average total detected Rydberg counts per cycle for the $40g \rightarrow 42g$ transition. Although an increase in detected Rydberg counts can improve the signal/noise ratio, Rydberg-Rydberg interactions can cause a red shift of the detected transition frequency, as well as asymmetric broadening (compare insets of Figure 7.4). The asymmetric lineshape observed at high Rydberg counts (in the inset of Figure 7.4) can be attributed to an attractive van der Waals interaction between Rydberg atoms. Although a Lorentzian is not an ideal choice as

a fit function for these asymmetric shapes, it still provides an approximate value for the peak shift/broadening as a function of detected Rydberg counts. Importantly, for each transition, the peak position and width become approximately constant below about ten detected Rydberg counts, and the final data sets are therefore limited to this Rydberg-count region.

7.3 Results

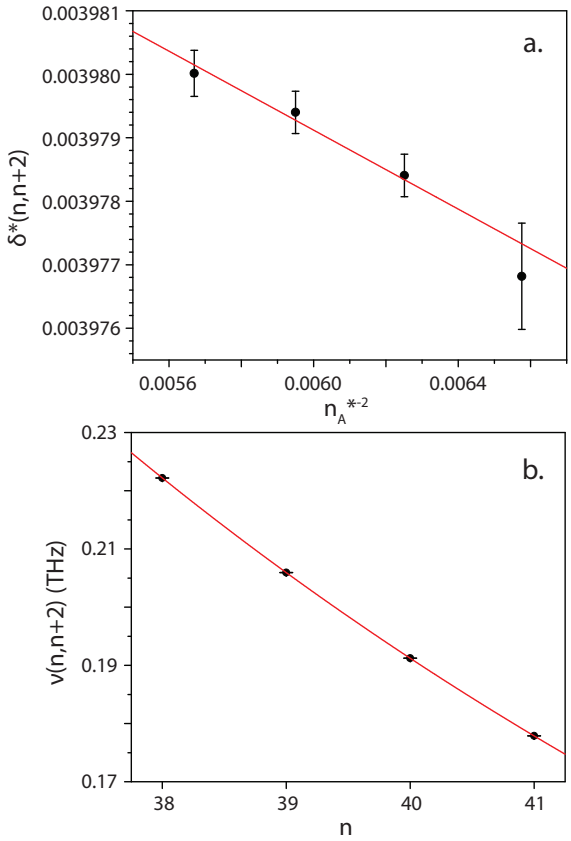

Figure 7.5: **Quantum defect determination.** (a) Determination of δ_0^*. Black circles, data. Error bars, error propagated from final frequency-interval results (see Table 7.2). Red line, weighted linear fit to data. (b) Determination of δ_0 and δ_2. Black circles, data. Error bars, error in final frequency-interval results (see Table 7.2). Red line, nonlinear least-squares fit to data using model in Equation 7.3, initialized using δ_0^* and δ_2^*. See text for details.

The systematic corrections for each measured transition frequency are listed in Table 7.1. The uncertainties have been reported to three significant digits, so as not

Shift (Hz)	$38g \rightarrow 40g$	$39g \rightarrow 41g$	$40g \rightarrow 42g$	$41g \rightarrow 43g$
AC Stark	0 ± 978	0 ± 965	0 ± 161	0 ± 452
DC Stark (x)	10 ± 2460	0 ± 2550	3 ± 765	459 ± 924
DC Stark (y)	4 ± 1550	10 ± 1140	0 ± 1430	0 ± 1780
DC Stark (z)	$100 \pm 14\bar{0}00$	13970 ± 4230	80 ± 4370	20 ± 4120
"Clock"	0 ± 11	$0 \pm 1\bar{0}$	$478\bar{0} \pm 191$	0 ± 9

Table 7.1: Summary of corrections to the measured ng-series transition-frequency intervals. A bar over a zero digit indicates that the digit is significant. See text for details.

to lose information in the calculations of the corrected transition frequencies (which are rounded to two significant digits in Table 7.2).

For $39g \rightarrow 41g$, there is a z-direction DC Stark shift of -14 kHz in the final averaged data, which accounts for a small field adjustment that was made subsequent to field-zeroing. This has been determined by comparing the final result with the result from field-zeroing. All other final data sets are consistent with field-zeroing results.

To obtain a final δ_g value, I follow the procedure of Reference [65]. First, I calculate an average quantum defect $\delta^*(n, n+2)$ for the pair of appropriate levels using

$$\nu_{n_1,n_2} = R_{\mathrm{Rb}} c \left(\frac{1}{(n_1 - \delta(n_1))^2} - \frac{1}{(n_2 - \delta(n_2))^2} \right), \tag{7.3}$$

where $\nu_{n_1,n_2} = \omega_{31}/(2\pi)$ and R_{Rb} is the Rydberg constant using the rubidium reduced mass. Here, the substitution $\delta(n_1) = \delta(n_2) = \delta^*(n, n+2)$ is made. Table 7.2 lists the final reported transition frequencies $\nu_{n,n+2}$, including corrections from Table 7.1, along with the corresponding values of $\delta^*(n, n+2)$.

Next, in Figure 7.5 I plot $\delta^*(n, n+2)$ versus n_A^{*-2}, where $n_A^* = n+1-\delta_0^G$. Here, δ_0^G is the previous value of δ_0 determined by [19]. Extrapolating to $n_A^{*-2} = 0$, I obtain $\delta_0^* = 0.0039978$.

For each frequency interval, I use Equation 7.3 and substitute $\delta(n) = \delta_0^* + \delta_2/(n - \delta_0^*)^2$ to solve for δ_2. Averaging the four results yields a preliminary value $\delta_2^* = -0.018741$.

Using δ_0^* and δ_2^* as initial values for the two free parameters δ_0 and δ_2, I perform a nonlinear least-squares fit of Equation 7.3 to the transition-frequency values listed in Table 7.2, where n is the independent variable (Figure 7.5). I use a Levenberg-Marquardt algorithm, weighting uncertainties σ_i as $1/\sigma_i^2$.

The final results for the ng-series quantum defects are $\delta_0 = 0.0039977(26)$ and $\delta_2 = -0.0186(25)$. The uncertainties are the standard error of the fit. These results are consistent with recent previous ng-series measurements [19], but at least one order of magnitude more precise.

n	Transition frequency (GHz)	$\delta^*(n, n+2)$
38	222.199268(14)	0.00397682(84)
39	205.9325407(52)	0.00397841(33)
40	191.2159230(47)	0.00397940(33)
41	177.8690737(46)	0.00398002(36)

Table 7.2: Summary of measurement results leading to the ng-series quantum-defect measurement. See text for details.

Finally, I have explored how to use this precise ng-series energy-interval measurements to extract a new estimate of the Rb^+ polarizability, using the polarizability model found in Reference [19] (and presented in Chapter I). Unlike Reference [19], however, the measurements presented in this chapter are constrained to energy intervals between the same l. Consequently, to extract α_d and α_q, I have adapted the method of Reference [19] to interval measurements by writing

$$\frac{8\pi h\epsilon_0}{e^2}\frac{a_0^4}{r_{4,\mathrm{D}}}\left(\nu(n,n+2) - R_{\mathrm{Rb}}c\left(\frac{1}{n^2} - \frac{1}{(n+2)^2}\right)\right) = \alpha_d + \alpha_q\frac{r_{6,\mathrm{D}}}{a_0^2 r_{4,\mathrm{D}}}. \tag{7.4}$$

Here, $r_{i,\mathrm{D}} = \langle 1/r^i\rangle_{n,l} - \langle 1/r^i\rangle_{n+2,l}$. Using Equation 7.4 to analyze the energy-interval measurements in Table 7.2, I have confirmed that the measurements presented here do not rule out polarizability results consistent with Reference [19]. However, as

can be seen by examining the $\langle r^i \rangle_{n,l}$ functions in Reference [29], the variation in $\langle r^i \rangle_{n,l}$ has a much stronger l-dependence than n-dependence at the quantum numbers used in this experiment, which cannot be compensated for by the strong n-dependence exhibited in our data. Therefore, to reach a definitive improvement on α_d and α_q, an improved measurement of the nh-series quantum defect is required as well. I have demonstrated that the method presented in this chapter is suitable to improve nh-series quantum defects, and thus Rb^+ polarizability values, in near-future experiments.

The uncertainty of the Rb^+ polarizability value is one of the main uncertainty sources anticipated in the planned Rydberg constant measurement, presented in the next chapter. Therefore, extending the method I have described in this chapter to measure the quantum defects of nh states will be an important contribution toward that measurement.

CHAPTER VIII

System Design for the Rydberg Constant Measurement

In this chapter, I describe the design process for the cold-atom system for the Rydberg constant measurement that I designed and led a team to build over the course of three to four years, in parallel with the projects described in the preceding sections. This project is ongoing. Here, I will outline my primary contributions to the project and describe how these contributions help to lower the expected dominant uncertainties of the resulting measurement. Our ultimate goal is to perform a measurement that is competitive with the relative uncertainty of the currently accepted value, $\delta\nu/\nu = 5.9 \times 10^{-12}$ [22], as introduced in Chapter I. To reduce measurement uncertainty to this level, the measurement may ultimately be performed in microgravity, using the general procedure outlined here.

8.1 General procedure

Here, I outline the proposed method of the project. This is meant to be an outline only; details will be provided in future papers and theses after the experiment is performed. I utilize the precision-measurement concepts introduced in Chapter I to generate a list of expected dominant uncertainties (those with relative uncertainty

$\delta\nu/\nu > 10^{-12}$). These uncertainties motivate the final experimental design described in the next section.

8.1.1 Proposed method

As described in Chapter I, this experiment must be designed to extract a value of the Rydberg constant free from nuclear charge radius effects. For this reason, the proposed method utilizes circular-state Rydberg atoms ($|m| = n-1$). These Rydberg electronic states have a negligible probability of overlap with the nucleus and even the ionic core.

The general method is to perform a high-precision measurement of an energy interval between two well-defined atomic states with well-defined energy eigenvalues and extract the Rydberg constant using the Rydberg formula (Equation 1.12). We have chosen to probe the interval $|n = 51, n_1 = 0, n_2 = 0, |m| = 50\rangle \rightarrow |n = 53, n_1 = 1, n_2 = 1, |m| = 50\rangle$. These Stark states are expressed in parabolic coordinates (see Chapter I). The justification for these specific states is provided in the next section. Note that the initial state is a circular state.

In the experiment, we will begin with a sample of cooled and trapped ground-state rubidium atoms in an optical lattice. To prepare a cold-atom sample in the initial circular state of the Stark manifold, we optically excite to the Rydberg $51F$ state, as described in Chapter II and shown in Figure 2.2, and initiate ponderomotive trapping in the lattice. Following the procedure of Reference [66], we then use a static magnetic field, a ramped DC electric field, and a linearly-polarized RF field to circularize atoms with an anticipated $\sim$70% efficiency (as reported by [66]).

This circularization method is called the adiabatic rapid passage (ARP) method. It uses a RF field ($\sim$ 200 MHz) to couple the ladder of $|m, n_1 = 0\rangle$ Stark states from an optically-accessible low-m Stark state to a circular state, while applying the electric field along the quantization axis to shift the levels into resonance and

facilitate adiabatic population transfer. The desired transitions are a sequence of the type $|n, 0, n_2, m\rangle \rightarrow |n, 0, n_2{-}1, m{+}1\rangle$, where $m = n{-}n_2{-}1$ and $n_2 = n{-}4, n{-}5, \ldots, 0$. Typically, in order to attain efficient population transfer, a σ^+-polarized RF field must be used to couple the $\Delta m = +1$ transitions. However, a σ^+ RF field is difficult to generate. The novel modification to the ARP method made in Reference [66] that I have emulated in this design is the simultaneous application of a magnetic field along the quantization axis. This magnetic field will separate otherwise-near-degenerate magnetic sublevels. In that way, we may apply an experimentally-convenient linearly-polarized RF field (perpendicular to the quantization axis), which is a superposition of σ^+ and σ^- polarizations. The σ^- component of the field will not drive unwanted, parasitic $\Delta m = -1$ transitions, because these will be sufficiently out of resonance. In this way, we should attain efficient circularization using a linear RF field.

To maintain the atoms in well-defined Stark states, a DC electric field will be applied during the measurement, along with a parallel, weak magnetic field. The ponderomotive shift of the energy of each individual state due to the lattice must be a perturbation on top of each of these energy shifts (see discussion in Chapter I).

To perform a precision measurement of the ~ 94 GHz energy interval of the $|n = 51, n_1 = 0, n_2 = 0, |m| = 50\rangle \rightarrow |n = 53, n_1 = 1, n_2 = 1, |m| = 50\rangle$ transition, we will modulate the ponderomotive lattice at ~ 19 GHz and use the fifth harmonic to drive the transition. (See Chapter III for a description of the experiment I did to demonstrate that this type of modulated-lattice spectroscopy is possible, and see Chapter IV for a description of an experiment where I drove a transition with the fifth harmonic of the lattice modulation.) We will use state-selective field ionization (SSFI) to detect population in the excited state. During the measurement, the cold-atom sample of circular-state Rydberg atoms will be held in the well-controlled environment detailed below, so that any systematics on the measurement can be accurately evaluated.

8.1.2 Dominant uncertainties

Statistical, instrumental, and systematic uncertainties play key roles in any precision measurement. Statistical uncertainty in the experimentally-measured frequency will stem from the confidence level of the fit function that is used to determine the center of the measured spectral line. This confidence level typically decreases as the width of the spectral peak increases. Circular and near-circular states have long natural lifetimes τ on the order of tens of ms ($\tau \propto n^5$). If we probe the transition for a longer time than the natural lifetimes of both states, then the peak width ν_{LW} would ideally be limited by the natural lifetimes to $\nu_{\mathrm{LW}} = 2/(2\pi\tau) \approx$ a few Hz. (Here, the factor of 2 in the numerator arises from adding the linewidth of the upper state to the linewidth of the lower state).

However, in a realistic system, the peak width of a very narrow Rydberg-Rydberg transition such as this will typically be broadened by two main considerations: (1) Doppler broadening due to inhomogeneous velocity distributions in the atom sample and (2) population redistribution due to blackbody radiation. I have addressed the first consideration with my calculations in Chapter V, showing that Doppler broadening is eliminated in even-parity transitions for atoms in a magic-condition lattice (as is the case presented here). The second consideration is a specific concern of Rydberg atoms and has been addressed in the experimental design, presented in Subsection 8.2.1. In that section, I estimate that a statistical uncertainty of $\sim 3 \times 10^{-12}$ is achievable.

The main source of instrumental uncertainty stems from the microwave generator driving the lattice modulation, the internal crystal oscillator of which has a relative uncertainty of 10^{-6}. To solve this problem, I have purchased and installed a portable atomic clock (SRS FS725) as an external time source for the generator. The clock can be synchronized to an external GPS signal to attain a long-term accuracy of a few parts in 10^{-12}.

Systematic shifts of the unperturbed transition frequency must also be carefully considered. These shifts will all be calculated and applied as corrections to the experimentally-measured frequency, and the uncertainties will be added in quadrature. For example, in any precision frequency measurement with external, nonzero electric and magnetic fields (as in this proposed experiment), first-order Stark and Zeeman shifts would be expected to dominate the list of systematic shifts of the measured frequency from its unperturbed value. However, we have specifically chosen the initial and final states of the transition such that first-order Stark and Zeeman shifts are zero, along with their corresponding uncertainties (refer to Equation 1.8 and Equation 1.9). On the other hand, the second-order Stark shift on the measured transition frequency is expected to be nonzero (~ -7 Hz), with a relative uncertainty of $\delta\nu/\nu = 2\times 10^{-12}$. This uncertainty comes from assuming a 1% instrument stability (i.e. voltage fluctuations).

Two other systematics are expected to have $\delta\nu/\nu > 10^{-12}$. The first is the uncertainty due to the polarizability quantum defect, introduced in Chapter I and described further in Chapter VII. The current value [19] yields a relative uncertainty of 3×10^{-12}. In Chapter VII, I have described important groundwork that I have laid toward obtaining a polarizability quantum defect measurement with a lower uncertainty.

The second dominant uncertainty is the uncertainty on the differential shift due to the ponderomotive lattice. We plan to apply a three-dimensional, two-color lattice (one 1064 nm and two 532 nm) to confine the circular-state Rydberg atoms. We will dynamically modulate only one lattice direction (the 1064 nm direction). Although the lattice induces a shift on each individual level, it is possible to choose lattice parameters such that the differential shift of the measured transition frequency is zero (a magic condition, as demonstrated in Chapter IV). However, intensity fluctuations still introduce uncertainty on this zero shift. The $\delta\nu/\nu = 30 \times 10^{-12}$ relative uncer-

tainty listed in Table 8.1 stems from assuming a 1% intensity stability of the lattice lasers, given a lattice depth on the order of tens of kHz.

As can be seen from the table, this light-shift uncertainty dominates all others. If this relative uncertainty were lowered to be on the order of 1×10^{-12}, then the Rydberg constant measurement performed using the method outlined in this chapter would have a relative uncertainty $< 7 \times 10^{-12}$. This uncertainty would firmly enable us to identify any significant differences between our nuclear-charge-overlap-free measurement and the currently-accepted value (which is not free from nuclear charge overlap effects). Significant differences are expected to occur on the level of five standard deviations, which is the difference predicted to be observed if the Rydberg constant is the culprit in the proton radius puzzle. (This was discussed in detail in Chapter I).

Lowering the light-shift uncertainty is therefore our motivation for proposing that this experiment be performed in micro-gravity. In a micro-gravity environment, lattice light would not need to be used (in part) to localize atoms for a long period of time (~ 10 ms) against gravitational acceleration. We would therefore be free to use shallow lattices for the measurement (assuming the mean kinetic energy of the cold-atom sample is correspondingly lowered such that a sufficient number of atoms are still trapped). We estimate that lattice depths of a few hundred Hz (corresponding to 10 nK-temperature atoms) would lower the light-shift uncertainty to the 1×10^{-12} level.

Uncertainty source	$\delta\nu/\nu$ ($\times 10^{-12}$)	Justification
Residual lattice shift	30	Assuming 1% light-intensity fluctuations
Dipolar polarizability	3	Using the results from [19]
Second-order Stark	2	Assuming 1% voltage-source stability
Statistical	3	Blackbody radiation at 4 K
Instrumental	< 5	Using GPS-synchronized atomic clock

Table 8.1: Summary of dominant relative-uncertainty sources ($\delta\nu/\nu > 10^{-12}$) anticipated in the circular-state Rydberg constant measurement.

8.2 Experimental design

As motivated by the preceding discussion, this ultra-high vacuum system must be designed with sensitive control over DC electric fields, magnetic fields, RF fields, and blackbody radiation. This section describes the design of the in-vacuum components that provide this control.

8.2.1 Blackbody radiation shielding motivation

The light shift derived in Chapter I was for monochromatic light. A related concept is the shift and, in the case of Rydberg atoms, population redistribution, due to the spectrum of light from a blackbody at a temperature T. Rydberg atoms and Rydberg-Rydberg transitions have strong resonances in the microwave regime. Therefore, Rydberg atoms are especially sensitive to blackbody radiation, the distribution of which peaks in the microwave regime at room temperature. For example, the Planck radiation law for energy density $\rho(\nu)$ goes as [20]

$$\rho(\nu) = \frac{8\pi h\nu^3}{c^3(e^{h\nu/k_{\mathrm{B}}T} - 1)}, \tag{8.1}$$

where ν is the radiation frequency, k_{B} is Boltzmann's constant, and T is the temperature of the blackbody.

Homogeneous population redistribution involves blackbody-induced dipole transitions to nearby states, and includes photoionization (coupling to the continuum). Altogether, these form a total blackbody decay rate of $1/\tau_{\mathrm{bb}}$, which can increase the linewidth of a measured spectral line. The linewidth of a transition between two states with roughly the same decay rate goes as $\nu_{\mathrm{LW}} \approx 2/(2\pi\tau_{\mathrm{bb}})$. (Once again, the factor of 2 in the numerator arises from the addition of the decay rates of the upper and lower transitions).

The full expression for $1/\tau_{\mathrm{bb}}$ can be found in References [20, 67]. Approximations

to the expression depend on the ratio $(h\nu)/(k_{\mathrm{B}}T)$, where ν is the transition frequency between dipole-coupled states. For example, an approximation that assumes $h\nu \ll k_{\mathrm{B}}T$ (typically valid for large n and $T \approx 300$ K) sets the temperature-scaling at $1/\tau_{\mathrm{bb}} \propto T/n^{*2}$, where n^* is the principal quantum number including the quantum defect. It can be seen that the decay rate (and thus the linewidth) in this approximation increases linearly with T. Therefore, we expect to utilize cryogenics (liquid helium at a boiling point of 4 K) to lower the radiation temperature of the region surrounding the atoms. At $T = 4$ K, a full calculation [68] of the decay rate predicts $1/\tau_{\mathrm{bb}} \sim 100$ Hz for circular-state Rydberg atoms at $n \approx 50$, which translates to a linewidth of $\nu_{\mathrm{LW}} \approx 30$ Hz. Assuming we can determine the center of the spectral line to within 1/100 of the linewidth (a standard assumption), the resulting statistical relative uncertainty for the transition proposed in this chapter is estimated to be $\sim 3 \times 10^{-12}$. This uncertainty is already on the same order as the uncertainty of the currently-accepted value of the Rydberg constant (and does not yet include contributions from instrumental and systematic uncertainties). Therefore, it is evident that this experiment should be performed at a radiation temperature of no higher than $T \approx 4$ K in order to achieve adequate measurement uncertainties.

A secondary reason to perform the experiment at $T = 4$ K is to minimize the possible level shifts due to the off-resonant portion of the blackbody spectrum. A shift on level $|n, l\rangle$ is given by [20, 67]

$$V_{bb} = \frac{e^2}{\hbar} \sum_{n',l'} \int_0^\infty \frac{|\langle n'l'|r|nl\rangle|^2 E^2_{\omega_b} \omega(n, l; n'l')}{2(\omega(n, l; n'l')^2 - \omega_b^2)}. \tag{8.2}$$

Here, $\omega(n, l; n'l') = 2\pi\nu(n, l; n'l')$ is the angular transition frequency difference between a final state $|n', l'\rangle$ and an initial state $|n, l\rangle$. The electric-field amplitude E_{ω_b} is the amplitude of the radiation per spectral unit (i.e. in a bandwidth $\delta\omega_b$ around ω_b). This amplitude is dependent on the characteristic of the waves emitted from the

blackbody source. For example, waves in the far field can be approximated by plane waves, separated mathematically into an incoherent sum of monochromatic components. Then, the energy density per spectral unit $\rho(\nu)$ from Equation 8.1 can be equated to the time-averaged spectral density $\epsilon_0|E_{\omega_b}|^2/2$ per spectral unit, yielding a value for $|E_{\omega_b}|^2$ to be used in Equation 8.2.

To calculate the effects of a potential blackbody shift on the measurement, I used the numerical methods of Reference [67] to evaluate Equation 8.2 for our Rydberg levels of interest. Using this code, it was shown that, because both levels have very similar shifts, the total shift of the transition frequency at 4 K is fairly negligible at < -100 mHz. This result removed an initial concern about the experiment (that the measurement would be susceptible to a strong blackbody shift). Therefore, our main motivation for performing the experiment at cryogenic temperatures is to decrease line broadening.

8.2.2 Blackbody radiation shielding design

Because we need to perform the measurement at cryogenic temperatures, the experiment takes place inside an ultra-high vacuum chamber mounted to the bottom of a dual-envelope cryostat (Figures 8.1a and e). The cryostat controls the temperature of the in-vacuum enclosure inside which we produce a cold-atom sample, and it thereby alters the blackbody spectrum in that region. The inner envelope of the cryostat can hold liquid helium (LHe; $T = 4$ K) or liquid nitrogen (LN_2; $T = 77$ K) and is in thermal contact with an in-vacuum cold plate, onto which is mounted an electrode package (next section), as well as a copper bucket that surrounds the aluminum enclosure for additional shielding. The outer envelope of the cryostat is intended to hold liquid nitrogen to prevent rapid boil-off of the liquid helium in the inner envelope and is likewise in thermal contact with a second copper bucket that encompasses the first. Around all of these is mounted a stainless steel vacuum chamber at room

temperature. This nesting arrangement is displayed in Figure 8.1b.

I designed the electrode package, as well as the custom radiation shields and custom vacuum chamber. Important design considerations included preventing thermal contact between shield layers and providing optical access while minimizing exposure to room-temperature blackbody radiation. This was achieved by extending 2-cm-long tubes from the 1-cm-diameter optical access ports in the aluminum enclosure (Figure 8.1c), which decrease the solid angle of radiation admitted from outside the enclosure to about six degrees per port.

It should be noted that there is an additional optical access port through the center of the cryostat to the cold-atom region to provide optical access along the vertical direction. I otherwise provided twelve access ports through the radiation shields and vacuum chamber along the azimuthal direction at thirty-degree intervals, requiring critical measurement and alignment, as well as consideration of any material contraction due to cryogenic temperatures. Finally, I provided a second row of six feedthrough ports on the vacuum chamber below the optical access ports for vacuum pumps and electrical access.

8.2.3 In-vacuum electrode package

Similar to the design presented in Chapter VI, the ability to control electric fields in three dimensions is critical in precision spectroscopy. Here I present my design for the in-vacuum electrode package used for electric-field control and RF-field generation.

The geometry of this electrode package is somewhat less constrained than the package I designed in Chapter VI. The primary constraint is the 6-inch ($\sim$ 15-cm) diameter of the in-vacuum cold plate, onto which is affixed the aluminum enclosure of the electrode package. The copper plates of the electrode package are mounted to the inside of the aluminum enclosure using vacuum-compatible ceramic hardware for electrical insulation. The plates of the package need to permit adequate optical

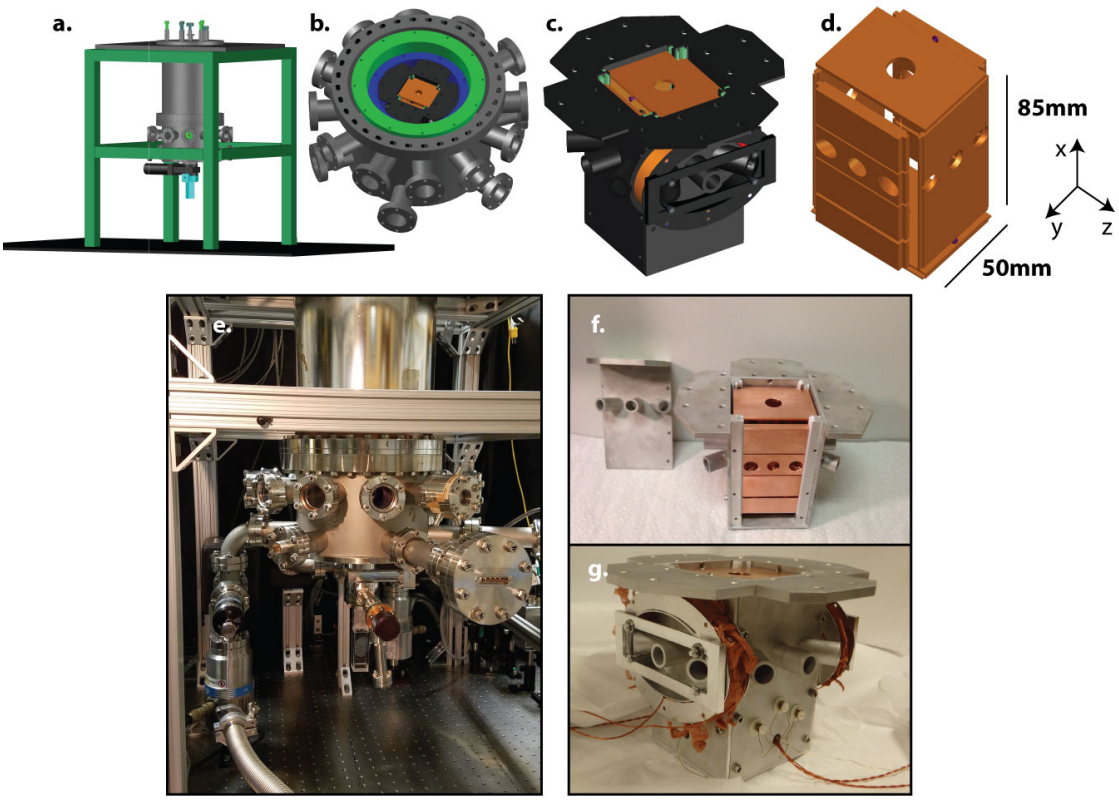

Figure 8.1: **Rydberg constant measurement vacuum system design.** (a)-(d) AutoCAD designs for the vacuum system. (e)-(g) Photos of the finished system. (a),(e) Assembled system, displaying glass MOT cell (bottom), custom vacuum chamber (middle), and cryostat (top). (b) Top view of the vacuum chamber detached from the cryostat. Green (blue) indicates the LN_2 (LHe) radiation shield. Black indicates the aluminum electrode enclosure, electrically isolated from the individual electrode plates (orange). (c),(g) Elliptical in-vacuum magnetic coils mounted to the outside of the aluminum enclosure. (d),(f) Copper electrodes, featuring separated plates for simultaneous DC voltage and RF field application.

access to the cold-atom sample for cooling light, optical Rydberg-state preparation, and the three-dimensional orthogonal lattice. The plates also require an aperture to permit the passage of electrons from the probe region to the MCP for detection. Due to orthogonality requirements of fields in the experiment, the MCP is mounted on a thirty-degree angle with respect to a plate normal.

This electrode package was designed to introduce RF fields (100-MHz-range) to the cold-atom sample in-vacuum, for use in the circularization process. Here, I followed the design of Reference [66]. As shown in Figures 8.1d and f, two opposite-facing

copper plates in the electrode package have been split into four segments along the y-axis. The three upper segments are used for RF generation. Prior to entering the vacuum chamber, the RF signal is split into four channels. Two of the channels are phase-inverted. In this way, we can apply signals with like phase to opposite-facing plate segments. This configuration is shown in Figure 8.2, which displays the results of a finite-element analysis of the RF potential applied across the plate segments (at a single time instance). This configuration produces a RF field linearly polarized along the x-direction, which is perpendicular to the stabilizing electric and magnetic fields (applied along z).

In addition to generating RF fields, a DC voltage can be independently applied to each plate in the electrode package for electric-field zeroing (see Chapter II), circularization, and Rydberg-atom detection.

8.2.4 Magnetic-field control

The system presented here uses a two-stage cooling and trapping scheme, as in the system presented in Chapter VI. A primary MOT is generated in a custom glass spectroscopy cell, mounted below the vacuum chamber. Atoms are transversely cooled and confined in a 2D+ MOT configuration [26] and directed upward via radiation pressure into the spectroscopy region (~ 25 cm away). In the spectroscopy region, atoms are either trapped in a secondary MOT using in-vacuum magnetic coils (done during the preliminary set-up) or else cooled into a (magnetic-gradient-free) optical molasses and trapped via a ponderomotive lattice (done while performing the precision measurement).

To draw as little power as possible while maintaining a 10-20 Gauss/cm field gradient (when used in an anti-Helmholtz configuration), the magnetic coils were mounted in-vacuum against the internal aluminum enclosure (Figures 8.1c and g). Due to the geometry of the system, these coils were restricted to an elliptical shape,

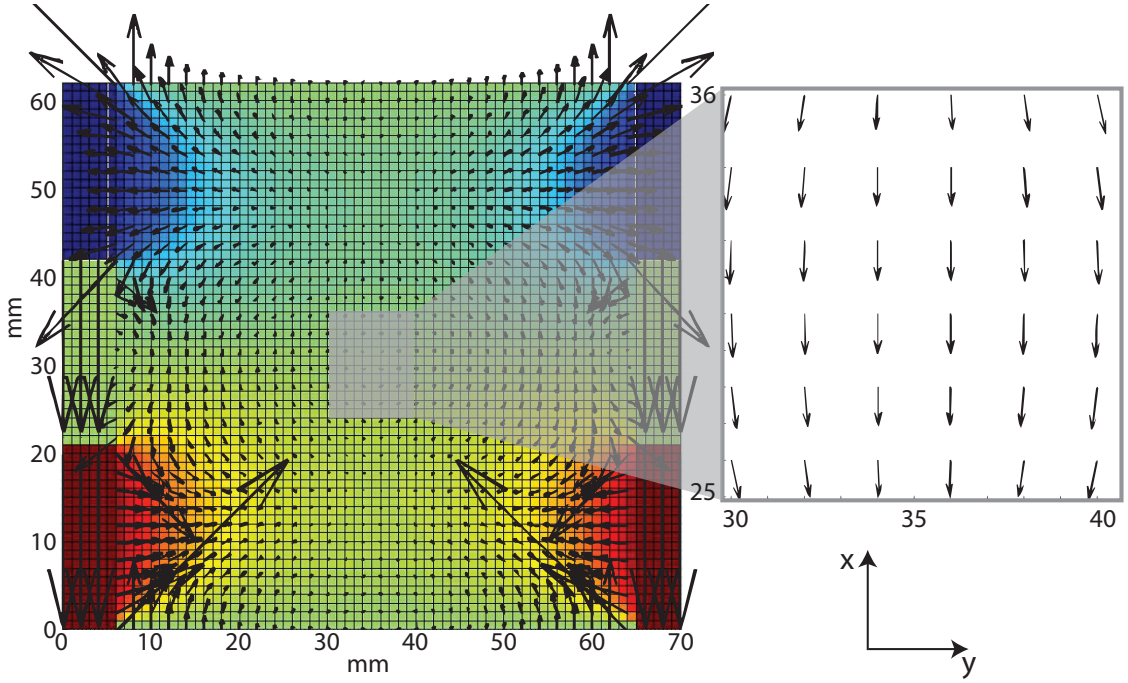

Figure 8.2: **Simulations showing linearity of the RF field at the center of the electrode package.** The colored region displays RF potential. Left and right boundaries (red, green, and blue rectangles) recreate electrode plate segments, set at an instantaneous RF voltage. Other boundaries are set at 0 V (represented by green). Red and blue represent voltages of equal magnitude but opposite phase. The overlaid arrows display RF-field magnitude and direction vectors. The inset demonstrates that the field is approximately linear (along the x-direction) within the center cm^2 of the enclosure, which encompasses the atom interaction region.

the details of which I determined using the procedure outlined in Chapter II. During a measurement, the coils will be used in a Helmholtz-like configuration to generate the necessary stabilization magnetic fields at the location of the atoms.

CHAPTER IX

Future Directions

This Rydberg constant measurement experiment is ongoing. Future collaborations may allow this design to be adapted for a micro-gravity-based cold-atom lab. A micro-gravity environment would allow for less trap light to be used during the experiment, a significant source of uncertainty in the anticipated measurement. Reducing that uncertainty would allow us to perform a precision measurement of the Rydberg constant that is competitive with the currently-accepted value but free from nuclear charge overlap, a crucial distinction needed to help solve the proton radius puzzle.

Throughout this dissertation, I have described three major topics of study using precision spectroscopy of Rydberg-Rydberg transitions, which together lay the groundwork for a future precision measurement of the Rydberg constant. Along the way, I have attempted to push the boundaries of measurement science by both demonstrating a novel atom-field interaction and improving upon a previous measurement of an atomic characteristic.

One major discovery I have pioneered is the first-ever demonstration of driving atomic transitions using an inelastic ponderomotive interaction (via an amplitude-modulated lattice). High-precision spectroscopy using the ponderomotive interaction promises at least two unique advantages over spectroscopy using the usual multipole-field interaction: flexible transition rules and vastly improved spatial addressability

of the quantum system. The selection rules for allowed transitions between electronic or magnetic states in an atom or molecule are greatly relaxed for ponderomotive spectroscopy, allowing unsurpassed access to previously forbidden transitions. Future experiments could use this ability to measure frequencies of previously inaccessible transitions, making it possible to characterize atoms and molecules more thoroughly than ever before, as well as investigate fundamental physics.

Another distinctive feature of ponderomotive spectroscopy is that its spatial resolution is orders of magnitude better than the transition frequency would suggest, promising single-site addressability in a dense particle array. This single-site addressability could be used to streamline certain quantum computing schemes.

In addition to these advantages, the ponderomotive interaction can also be used to simultaneously trap and probe atoms, leading to Fourier-limited spectral lines and the existence of magic-lattice conditions. These features will be especially important in utilizing ponderomotive spectroscopy for the planned Rydberg constant measurement.

Another achievement I have demonstrated has been to increase the known precision of a high-angular-momentum quantum defect of Rb by one order of magnitude. I have established a microwave-spectroscopy technique that may be replicated in future experiments to precisely measure the quantum defects of other high-angular-momentum states of Rb, thereby extracting an improved value of the Rb core polarizability. The Rb core polarizability is one leading uncertainty in the Rydberg constant measurement, thereby meriting further study.

Finally, I have made key design contributions to a future precision measurement of the Rydberg constant. This measurement has been planned with the goal of contributing toward the solution of the proton radius puzzle by performing a high-precision measurement of the Rydberg constant independent of effects due to nuclear charge overlap. One future direction would be to perform the measurement in a micro-gravity environment, thereby reducing the uncertainty contribution in that

measurement due to lattice-light fluctuations.

With these future possibilities, I anticipate that the work reported in this dissertation will be used as a stepping stone for further developments in precision spectroscopy.

APPENDICES

APPENDIX A

Rabi frequency due to the ponderomotive interaction

In this Appendix, I derive an expression for the Rabi frequency as a consequence of the inelastic ponderomotive atom-field interaction ("ponderomotive spectroscopy"). I use experimental parameters and related variables adopted from Chapter III. It is assumed that the reader has read the experimental set-up described in that chapter.

A.1 Amplitude modulation

In this section, I outline the derivation leading to a mathematical description of the dynamic amplitude-modulation of the ponderomotive optical lattice. The standing-wave lattice is a coherent sum of the optical fields of a time-dependent (dynamically amplitude-modulated) component and a fixed (unmodulated) component. First, I derive an intensity expression for the time-dependent component at the location of the atoms. Next, I write an intensity expression for the fixed component. Finally, I write the total intensity at the location of the atoms as a coherent sum of the two components, demonstrating a desirable parametric amplification of the time-dependent component.

A.1.1 Intensity contribution of the time-dependent (amplitude-modulated) component of the standing wave

The power of the 1064-nm laser beam transmitted through the fiber electro-optic modulator is

$$P_{\mathrm{T}} = P_{\mathrm{dyn}} \sin^2 \left(\frac{\pi}{2} \frac{V_{\mathrm{total}}}{V_\pi} \right), \tag{A.1}$$

where P_{dyn} is the maximum possible output of the fiber modulator, and V_π is the voltage difference between adjacent power transmission maxima and minima (a fixed property of the fiber modulator). V_{total}, the total voltage applied to the fiber modulator, is

$$V_{\mathrm{total}} = V_{\mathrm{DC}}(t) + V_\mu \sin(\Omega t) + V_{\mathrm{drift}}(t). \tag{A.2}$$

Here, $V_{\mathrm{DC}}(t)$ is the applied DC bias voltage, and V_μ is the amplitude of a microwave voltage signal with frequency Ω. Bias drifts due to thermal and environmental effects are accounted for via a slowly-varying effective drift voltage $V_{\mathrm{drift}}(t)$.

Experimentally, $V_{\mathrm{DC}}(t)$ is actively regulated such that $V_{\mathrm{DC}}(t) + V_{\mathrm{drift}}(t)$ is locked to the inflection point $V_\pi/2$ of the transmission curve given by Equation A.1. With the fiber modulator locked, the laser power transmission curve is

$$P_{\mathrm{T}} = P_{\mathrm{dyn}} \left(\frac{1}{2} + \frac{1}{2} \sin \left(\frac{\pi V_\mu}{V_\pi} \sin(\Omega t) \right) \right). \tag{A.3}$$

Experiments using the fundamental frequency Ω of the modulation are performed at $V_\mu = V_\pi/2$ (see Chapter III). This value of V_μ, as set at the microwave synthesizer, is dependent on the gain of the amplifier between the synthesizer and fiber modulator and is also slightly frequency-dependent. Therefore, V_μ is set experimentally using the procedure explained fully in Reference [69]. Experiments utilizing harmonics of the

fundamental modulation frequency are performed in Chapter IV using $V_\mu > V_\pi/2$, such that the nonlinearity of the fiber-modulator transmission function is engaged to produce odd harmonics in the modulation. Optimal values of V_μ for select odd harmonics are listed in Chapter IV. In principle, even harmonics in the modulation may also be produced if the lock point of $V_{\rm DC}\,(t) + V_{\rm drift}\,(t)$ is set to a maximum or minimum of the fiber-modulator transmission curve rather than the inflection point.

At the location of the atoms, the intensity is determined by the incident $(1/e^2)$ radial beam waist $w_{\rm inc} = 11$ μm and the incident beam power, which is measured (in the absence of modulation) to be $P_{0\,\rm dyn}$ =5-10 mW. (This value is much less than $P_{\rm dyn}$ in Equation A.1 due to inefficiencies in the intervening optical system.) Therefore, the maximum intensity of the dynamically amplitude-modulated running-wave beam incident at the location of the atoms is

$$I_{0\,\rm inc}^{\rm dyn} = \frac{2\,P_{0\,\rm dyn}}{\pi w_{\rm inc}^2}. \tag{A.4}$$

The time-dependence of this beam, determined using Equation A.3 and Equation A.4, is expressed by

$$I_{\rm rw}^{\rm dyn} = I_{0\,\rm inc}^{\rm dyn}\left(\frac{1}{2} + \sum_{q=1,3,5\ldots}^{\infty} \mathrm{J_q}\left(\frac{\pi V_\mu}{V_\pi}\right)\sin\left(q\Omega t\right)\right). \tag{A.5}$$

Here, the sum over q has arisen from expanding Equation A.3 using the Jacobi-Anger relation. Throughout the dissertation, q represents a harmonic order in the lattice modulation.

This incident beam is retro-reflected to form an amplitude-modulated, standing-wave optical lattice. The power transmission efficiency of the optics in the lattice return beam path has been determined to be 56%. Optical aberrations and a displacement of the retro-reflector position from the optical axis have been estimated to yield an effective return beam waist radius of $w_{\rm ret} = 37$ μm. Therefore, the ratio

of the return intensity to the incident intensity on the optical axis is $\varepsilon = 9\%$. After adding the fields of the incident and return beams coherently, the intensity of the dynamically amplitude-modulated standing-wave beam is

$$I_{\rm sw}^{\rm mod} = I_{0\,\rm inc}^{\rm dyn} \left(\frac{1}{2} + \sum_{q=1,3,5\ldots}^{\infty} \mathrm{J_q}\left(\frac{\pi V_\mu}{V_\pi} \right) \sin\left(q\Omega t\right) \right) \times \Big(1 + \varepsilon + 2\sqrt{\varepsilon}\cos\left(2kz\right) \Big), \tag{A.6}$$

where k is the optical wavenumber $k = 2\pi/\lambda$.

A.1.2 Intensity contribution of the fixed (unmodulated) portion of the standing wave

Similar to Equation A.4, the intensity of the fixed (unmodulated) running-wave beam at the location of the atoms is

$$I_{0\,\rm inc}^{\rm fixed} = \frac{2\, P_{0\,\rm fixed}}{\pi w_{\rm inc}^2}, \tag{A.7}$$

where beam power $P_{0\,\rm fixed}$ is measured to be 900 mW. When retro-reflected, this beam forms a standing wave. The corresponding expression is

$$I_{\rm sw}^{\rm fixed} = I_{0\,\rm inc}^{\rm fixed} \left(1 + \varepsilon + 2\sqrt{\varepsilon}\cos\left(2kz\right) \right). \tag{A.8}$$

A.1.3 Total standing-wave intensity

The fields of the fixed and time-dependent standing waves are summed coherently to yield an intensity,

$$I_{\mathrm{sw}}^{\mathrm{dyn+fixed}} = \Bigg[I_{0\,\mathrm{inc}}^{\mathrm{dyn}} \left(\frac{1}{2} + \sum_{q=1,3,5\ldots}^{\infty} \mathrm{J_q}\left(\frac{\pi V_\mu}{V_\pi}\right) \sin\left(q\Omega t\right) \right) + 2\sqrt{ I_{0\,\mathrm{inc}}^{\mathrm{dyn}}\, I_{0\,\mathrm{inc}}^{\mathrm{fixed}} \left(\frac{1}{2} + \sum_{q=1,3,5\ldots}^{\infty} \mathrm{J_q}\left(\frac{\pi V_\mu}{V_\pi}\right) \sin\left(q\Omega t\right) \right) } + I_{0\,\mathrm{inc}}^{\mathrm{fixed}} \Bigg] \times \Big(1 + \varepsilon + 2\sqrt{\varepsilon}\cos\left(2kz\right) \Big). \tag{A.9}$$

This expression for the total, time-dependent standing-wave intensity at the location of the atoms includes odd harmonics of the microwave frequency Ω.

A.2 Rabi frequency in the ponderomotive interaction

For simplicity, I consider a two-level atomic system that has a transition resonant with the fundamental modulation frequency Ω ($q = 1$) and that is insensitive to higher harmonics. As explained in Chapter III, the light intensity must also be spatially-varying within the volume of the atom to couple Rydberg states. After a spectral analysis of Equation A.9 to separate different frequency components, the q=1 spatially-varying, time-dependent component of the total standing-wave intensity is

$$\begin{aligned} I_{\Omega\,\mathrm{sw}}^{\mathrm{dyn+fixed}} &\approx 2\sqrt{\varepsilon}\, I_{0\,\mathrm{inc}}^{\mathrm{dyn}}\, \mathrm{J}_1\left(\frac{\pi V_\mu}{V_\pi}\right) \left(1 + \sqrt{\frac{2\, I_{0\,\mathrm{inc}}^{\mathrm{fixed}}}{I_{0\,\mathrm{inc}}^{\mathrm{dyn}}}} \right) \sin\left(\Omega t\right)\cos\left(2kz\right) \\ &=: B_\Omega \sin\left(\Omega t\right)\cos\left(2kz\right). \end{aligned} \tag{A.10}$$

This component of the intensity leads to the $|A|^2$ term in the atom-field interaction Hamiltonian that is important in lattice modulation spectroscopy,

$$A_\Omega^2\left(z,t\right) = \frac{I_{\Omega\,\mathrm{sw}}^{\mathrm{dyn+fixed}}}{c\epsilon_0\omega^2} = \frac{B_\Omega}{c\epsilon_0\omega^2}\sin\left(\Omega t\right)\cos\left(2kz\right). \tag{A.11}$$

In the atom-field interaction Hamiltonian, the corresponding term is

$$V_\Omega = \frac{e^2 B_\Omega}{2 m_e c \epsilon_0 \omega^2} \sin(\Omega t) \cos(2kz) \,. \tag{A.12}$$

Following Reference [43], V_Ω is the driving term in the interaction potential, and the corresponding Rabi frequency for an atomic transition is therefore given by

$$\chi \approx \sqrt{\varepsilon} \frac{e^2}{\hbar m_e c \epsilon_0 \omega^2} \, I_{0\,\mathrm{inc}}^{\,\mathrm{dyn}} \, \mathrm{J}_1 \left(\frac{\pi V_\mu}{V_\pi} \right) \left(1 + \sqrt{\frac{2 \, I_{0\,\mathrm{inc}}^{\,\mathrm{fixed}}}{I_{0\,\mathrm{inc}}^{\,\mathrm{dyn}}}} \right) D_{n,l,m}^{n',l',m'}(\tilde{z}). \tag{A.13}$$

Here, $D_{n,l,m}^{n',l',m'}(\tilde{z})$ is the (unitless) transition matrix element between electronic states $|n,l,m\rangle \rightarrow |n',l',m'\rangle$ that are resonantly coupled by frequency Ω. For atoms located at lattice intensity minima (or maxima), this matrix element includes a $\cos(2k\tilde{z})$ dependence, where $\tilde{z}$ is the center-of-mass position of the Rydberg atom relative to the nearest optical-lattice intensity maximum. In this case, the spatial coupling has a leading term proportional to $\tilde{z}^2$. This spatial coupling yields a large matrix element for $\Delta l = 0, 2$ transitions in first order (in the interaction). For example, in the experiment presented in Chapter III, the interrogated transition $|58S_{1/2}\rangle \rightarrow |59S_{1/2}\rangle$ is normally dipole-forbidden. Numerical, first-order calculations [43] show $D_{58S}^{59S} = 0.215$ at lattice minima. Using the experimental parameters given in the above sections, we find a Rabi-frequency estimate of $2\pi \times 100$ kHz and a population inversion time of 5 μs.

Notice that in the above derivation, ε is a factor used to account for inefficiencies in the lattice optics system. Likewise, the parametric amplification due to $I_{0\,\mathrm{inc}}^{\,\mathrm{fixed}}$ in not an intrinsic requirement of this atom-field interaction. Therefore, when modeling the dynamics of this interaction (as in Chapter V), it is suitable to set $\varepsilon = 1$ and $I_{0\,\mathrm{inc}}^{\,\mathrm{fixed}} = 0$.

APPENDIX B

Magic conditions in ponderomotive spectroscopy

In this Appendix, I derive expressions for the state-dependent, ponderomotive-induced light shift on Rydberg-Rydberg transitions driven via ponderomotive spectroscopy. This concept is specifically important in identifying magic-wavelength conditions, as in Chapter IV, and is generally important in using ponderomotive spectroscopy for precision-measurement applications.

B.1 Lattice light shifts of Rydberg-Rydberg transitions

As introduced in Chapter I, the light shift (potential) for a Rydberg atom in an optical lattice is determined by a weighted average of the free-electron ponderomotive potential with respect to the Rydberg-electron wavefunction density. For an ideal one-dimensional lattice aligned along the z-direction, the lattice-induced shift of an unperturbed energy level $E_{n,l}$ of a non-degenerate low-angular-momentum Rydberg atom with quantum numbers n, l, and m is given by [43]

$$V_{n,l,m}(\tilde{z}) - E_{n,l} = \frac{e^2|E_0|^2}{4m_e\omega_L^2} \sum_{p=0}^{\infty} C_p (r_e^p)_{n,l}^{n,l} (\cos^p \theta_e)_{l,m}^{l,m}, \tag{B.1}$$

where

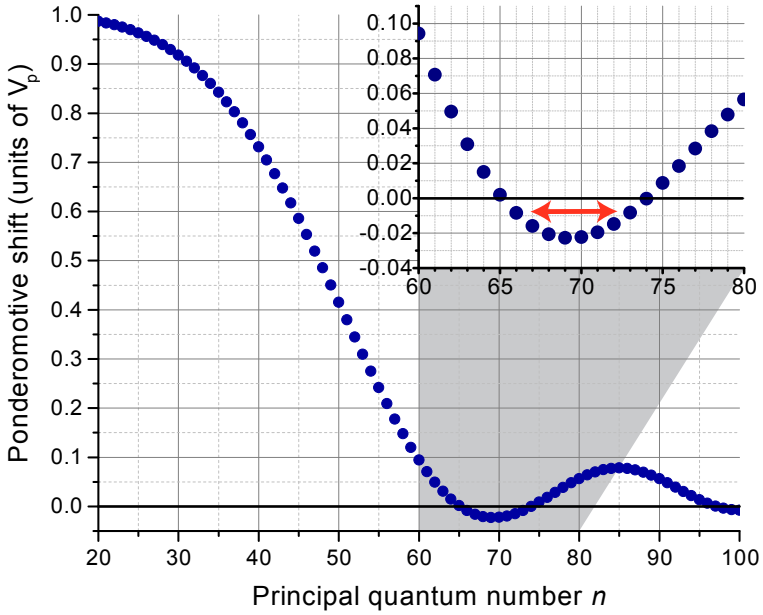

Figure B.1: **Rydberg energy-level shifts in a ponderomotive optical lattice versus principal quantum number n.** Plotted for S-state Rydberg atoms trapped at 1064-nm lattice intensity minima. Units, free-electron ponderomotive potential V_p. Notice flips in polarizability at $n \sim 65$, $n \sim 74$, etc. The arrow indicates an example of a magic-wavelength transition.

$$C_p = \frac{(2k)^p}{p!} \begin{cases} (-1)^{p/2} \cos(2k\tilde{z}) + \delta_{p,0} & p \text{ even} \\ (-1)^{(p+1)/2} \sin(2k\tilde{z}) & p \text{ odd} \end{cases} . \tag{B.2}$$

Here, E_0 is the peak electric-field amplitude within the optical standing wave, $k = \omega_L/c$ is the wavenumber of the 1064-nm beam, $\tilde{z}$ is the center-of-mass z-coordinate of the Rydberg atom (origin coincident with a lattice intensity maximum), and r_e and θ_e are the radial and polar relative coordinates, respectively, of the Rydberg electron (with respect to the atomic core). The energy shift of Equation B.1 is plotted in Figure B.1, which demonstrates the state-dependence of the lattice-shifted energy levels in units of the free-electron ponderomotive potential $V_p = \frac{e^2|E_0|^2}{4m_e\omega_L^2}$ (see Chapter I).

A Rydberg-Rydberg transition $|n, l, m\rangle \rightarrow |n', l', m'\rangle$ has an unperturbed transition energy $E_{n',l'} - E_{n,l}$. This transition energy has a perturbation due to the lattice,

$\Delta V(\tilde{z})$, given by

$$\Delta V(\tilde{z}) = \frac{e^2|E_0|^2}{4m_e\omega_L^2}\sum_{p=0}^{\infty} C_p(\tilde{z})[(r_e^p)_{n',l'}^{n',l'}(\cos^p\theta_e)_{l',m'}^{l',m'} - (r_e^p)_{n,l}^{n,l}(\cos^p\theta_e)_{l,m}^{l,m}]. \tag{B.3}$$

In the work presented in this dissertation, $m = m'$. Additionally, it can be seen that for odd p, the matrix elements vanish due to parity restrictions. For the special case of $p = 0$, the matrix elements are unity for either state and cancel regardless of location within the lattice. (The effect of the Rydberg angular wavefunction in a ponderomotive optical lattice has been investigated in Reference [40]).

For the transitions driven in the experiments in Chapter III and Chapter IV, $l = l' = 0$. Upon simplifying $\Delta V(\tilde{z})$ and reorganizing terms, the role of the ratio of the radial electron coordinate r_e to the lattice light wavelength λ in the overall state-dependence of the transition-energy shift becomes evident:

$$\Delta V(\tilde{z}) = \frac{e^2|E_0|^2}{4m_e\omega_L^2}\cos(2k\tilde{z})\sum_{p=2,4\ldots}^{\infty}\frac{(4\pi)^p(-1)^{p/2}}{p!}(\cos^p\theta_e)_{l,m}^{l,m}\Big[\Big(\Big(\frac{r_e}{\lambda}\Big)^p\Big)_{n',l}^{n',l} - \Big(\Big(\frac{r_e}{\lambda}\Big)^p\Big)_{n,l}^{n,l}\Big]. \tag{B.4}$$

The light intensity maxima [minima] are located at $\tilde{z} = m\lambda/2$ [$\tilde{z} = (2m+1)\lambda/4$], where m is an integer. When these values are inserted into Equation B.4, it can be seen that the shifts of the Rydberg-Rydberg transition energy for atoms located at lattice intensity maxima or minima are equal in magnitude but opposite in sign.

For Rydberg atoms considerably smaller than the lattice period, the p=2 term dominates the series. In that case, trapping potential minima [maxima] are co-located with light intensity minima [maxima]. Furthermore, it can be seen in Equation B.4 that the terms under the sum have alternating signs. The resultant partial cancellations lead to shallower potentials as $r_e \to \lambda$. This case is represented in Figure B.2,

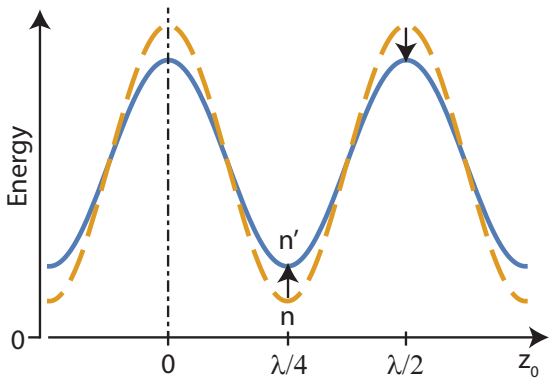

Figure B.2: **Potential landscape of Rydberg levels in a ponderomotive optical lattice versus Rydberg atom position $\tilde{z}$.** The lattice electric field amplitude has a maximum at $\tilde{z} = 0$. For $r_e < \lambda$ and $n' > n$, the dashed curve indicates the lower-level Rydberg state and the solid curve indicates the upper-level state. A Rydberg-Rydberg transition between the two states at a lattice potential minimum is blue-shifted relative to the unperturbed value. A transition at a lattice potential maximum is red-shifted. As derived in the text, these shifts are equal in magnitude.

where the upper-state Rydberg level n' has a shallower potential than the lower-state Rydberg level n. The lattice-induced shifts in the Rydberg-Rydberg transition, indicated by arrows in the figure, are positive (blue-shifted) at the trapping potential minima and negative (red-shifted) at the trapping potential maxima.

For $r_e/\lambda \approx 1$ it can be further shown that the aforementioned cancellation of terms in Equation B.4 becomes near-perfect, leading to very shallow lattice potentials with spatial modulation depths that are $\lesssim 2\%$ of the free-electron ponderomotive potential (see inset in Figure B.1). For experiments with $\lambda = 1064$ nm, this occurs for principal quantum numbers near $n \approx 70$. Incidentally, this is also the principal quantum number range conducive to magic-lattice spectroscopy, i.e. where nearby levels have the same ponderomotive shift.

BIBLIOGRAPHY

BIBLIOGRAPHY

[1] J. Ye, H. J. Kimble, and H. Katori. Quantum-state engineering and precision metrology using state-insensitive light traps. *Science*, 320(5884):1734–1738, 2008.

[2] H. Katori. Optical lattice clocks and quantum metrology. *Nat. Phot.*, 5(4):203–210, 2011.

[3] A. Peters, K. Y. Chung, and S. Chu. High-precision gravity measurements using atom interferometry. *Metrologia*, 38(1):25, 2001.

[4] Z-T. Lu and P. Mueller. Atom-trap trace analysis of rare noble gas isotopes. *Adv. in AMO Phys.*, 58:173–205, 2010.

[5] A. Schliesser, M. Brehm, F. Keilmann, and D. W. van der Weide. Frequency-comb infrared spectrometer for rapid, remote chemical sensing. *Opt. Expr.*, 13(22):9029–9038, 2005.

[6] P. R. Berman and V. S. Malinovsky. *Principles of Laser Spectroscopy and Quantum Optics*. Princeton University Press, 2010.

[7] D. Jaksch, J. I. Cirac, P. Zoller, S. L. Rolston, R. Côté, and M. D. Lukin. Fast quantum gates for neutral atoms. *Phys. Rev. Lett.*, 85(10):2208, 2000.

[8] M. S. Safronova, C. J. Williams, and C. W. Clark. Optimizing the fast Rydberg quantum gate. *Phys. Rev. A*, 67(4):040303, 2003.

[9] M. Saffman, T. G Walker, and K. Mølmer. Quantum information with Rydberg atoms. *Rev. Mod. Phys.*, 82(3):2313, 2010.

[10] J. C. Bernauer and R. Pohl. The proton radius problem. *Sci. Amer.*, 310(2):32–39, 2014.

[11] R. Pohl, A. Antognini, F. Nez, F. D. Amaro, F. Biraben, J. M. R. Cardoso, D. S. Covita, A. Dax, S. Dhawan, L. M. P. Fernandes, et al. The size of the proton. *Nature*, 466(7303):213–216, 2010.

[12] A. Antognini, F. Nez, K. Schuhmann, F. D. Amaro, F. Biraben, J. M. R. Cardoso, D.S. Covita, A. Dax, S. Dhawan, M. Diepold, et al. Proton structure from the measurement of 2S-2P transition frequencies of muonic hydrogen. *Science*, 339(6118):417–420, 2013.

[13] J. C. Bernauer, A. Hosaka, K. Khemchandani, H. Nagahiro, and K. Nawa. High-precision determination of the electric and magnetic form factors of the proton. In *AIP Conf. Proc.*, volume 1388, pages 128–134. AIP, 2011.

[14] R. Pohl, R. Gilman, G. A. Miller, and K. Pachucki. Muonic hydrogen and the proton radius puzzle. *Ann. Rev. Nucl. Part. Sci.*, 63:175–204, 2013.

[15] C. E. Carlson. The proton radius puzzle. *Prog. Part. Nucl. Phys.*, 82:59–77, 2015.

[16] V. Barger, C-W. Chiang, W-Y. Keung, and D. Marfatia. Proton size anomaly. *Phys. Rev. Lett.*, 106(15):153001, 2011.

[17] C. E. Carlson and M. Vanderhaeghen. Higher-order proton structure corrections to the Lamb shift in muonic hydrogen. *Phys. Rev. A*, 84(2):020102, 2011.

[18] A. Antognini, F. Kottmann, F. Biraben, P. Indelicato, F. Nez, and R. Pohl. Theory of the 2S-2P Lamb shift and 2S hyperfine splitting in muonic hydrogen. *Ann. Phys.*, 331:127–145, 2013.

[19] J. Lee, J. Nunkaew, and T. F. Gallagher. Microwave spectroscopy of the cold Rb $(n+1)D_{5/2} \rightarrow nG$ and nH transitions. *Phys. Rev. A*, 94(2):022505, 2016.

[20] T. F. Gallagher. *Rydberg Atoms*. Cambridge University Press, 2005.

[21] J. C. De Vries. *A Precision Millimeter-wave Measurement of the Rydberg Frequency*. Massachusetts Institute of Technology, 2009.

[22] P. J. Mohr, D. B. Newell, and B. N. Taylor. CODATA recommended values of the fundamental physical constants: 2014. *Journ. Phys. Chem. Ref. Data*, 45(4):043102, 2016.

[23] J. Hare, A. Nussenzweig, C. Gabbanini, M. Weidemuller, P. Goy, M. Gross, and S. Haroche. Toward a Rydberg-constant measurement on circular atoms. *IEEE Trans. Instr. Meas.*, 42(2):331–334, 1993.

[24] J. N. Tan and P. J. Mohr. Tests of theory in Rydberg states of one-electron ions. In *Fundamental Physics in Particle Traps*, pages 375–404. Springer, 2014.

[25] D. J. Griffiths. *Introduction to Quantum Mechanics*. Cambridge University Press, 2016.

[26] H. J. Metcalf and P. Van der Straten. *Laser Cooling and Trapping*. Springer Science & Business Media, 2012.

[27] S. E. Anderson, K. C. Younge, and G. Raithel. Trapping Rydberg atoms in an optical lattice. *Phys. Rev. Lett.*, 107(26):263001, 2011.

[28] J. Han, Y. Jamil, D. V. L. Norum, P. J. Tanner, and T. F. Gallagher. Rb nF quantum defects from millimeter-wave spectroscopy of cold ^{85}Rb Rydberg atoms. *Phys. Rev. A*, 74(5):054502, 2006.

[29] H. A. Bethe and E. E. Salpeter. *Quantum Mechanics of One-and Two-Electron Atoms*. Springer Science & Business Media, 2012.

[30] K. C. Younge, S. E. Anderson, and G. Raithel. Rydberg-atom trajectories in a ponderomotive optical lattice. *New Journ. Phys.*, 12(11):113036, 2010.

[31] Kelly C. Y. and Georg R. Rotary echo tests of coherence in Rydberg-atom excitation. *New Journ. Phys.*, 11(4):043006, 2009.

[32] W. H. Wing. Electrostatic trapping of neutral atomic particles. *Phys. Rev. Lett.*, 45(8):631, 1980.

[33] T. Breeden and H. Metcalf. Stark acceleration of Rydberg atoms in inhomogeneous electric fields. *Phys. Rev. Lett.*, 47(24):1726, 1981.

[34] S. D. Hogan and F. Merkt. Demonstration of three-dimensional electrostatic trapping of state-selected Rydberg atoms. *Phys. Rev. Lett.*, 100(4):043001, 2008.

[35] J. R. Guest, J-H. Choi, E. Hansis, A. P. Povilus, and G. Raithel. Laser cooling and magnetic trapping at several Tesla. *Phys. Rev. Lett.*, 94(7):073003, 2005.

[36] I. Lesanovsky and P. Schmelcher. Magnetic trapping of ultracold Rydberg atoms. *Phys. Rev. Lett.*, 95(5):053001, 2005.

[37] S. K. Dutta, J. R. Guest, D. Feldbaum, A. Walz-Flannigan, and G. Raithel. Ponderomotive optical lattice for Rydberg atoms. *Phys. Rev. Lett.*, 85(26):5551, 2000.

[38] S. Zhang, F. Robicheaux, and M. Saffman. Magic-wavelength optical traps for Rydberg atoms. *Phys. Rev. A*, 84(4):043408, 2011.

[39] K. C. Younge, B. Knuffman, S. E. Anderson, and G. Raithel. State-dependent energy shifts of Rydberg atoms in a ponderomotive optical lattice. *Phys. Rev. Lett.*, 104(17):173001, 2010.

[40] S. E. Anderson and G. Raithel. Dependence of Rydberg-atom optical lattices on the angular wave function. *Phys. Rev. Lett.*, 109:023001, 2012.

[41] K.C. Younge, S. E. Anderson, and G. Raithel. Adiabatic potentials for Rydberg atoms in a ponderomotive optical lattice. *New Journ. Phys.*, 12, 2010.

[42] H. Friedrich. *Theoretical Atomic Physics*. Springer, 2006.

[43] B. Knuffman and G. Raithel. Multipole transitions of Rydberg atoms in modulated ponderomotive potentials. *Phys. Rev. A*, 75(5):053401, 2007.

[44] T. Meyrath. Electromagnet design basics for cold atom experiments. `hank.uoregon.edu/experiments/atom-trap/electromagnets.pdf`, 2004. Accessed April 3, 2017.

[45] D. A. Steck. Rubidium 85 D line data. 2008.

[46] C. J. Hawthorn, K. P. Weber, and R. E. Scholten. Littrow-configuration tunable external cavity diode laser with fixed-direction output beam. *Rev. Sci. Instr.*, 72(12):4477–4479, 2001.

[47] C. J. Foot. *Atomic Physics*. Oxford University Press, 2005.

[48] E. Hansis, T. Cubel, J-H. Choi, J. R. Guest, and G. Raithel. Simple pressure-tuned Fabry-Pérot interferometer. *Rev. Sci. Instr.*, 76(3):033105, 2005.

[49] D. P. Fahey and M. W. Noel. Excitation of Rydberg states in Rb with near-infrared diode lasers. *Opt. Expr.*, 19(18):17002–17012, 2011.

[50] L. A. M. Johnson, H. O. Majeed, B. Sanguinetti, T. Becker, and B. T. H. Varcoe. Absolute frequency measurements of ^{85}Rb $nF_{7/2}$ Rydberg states using purely optical detection. *New Journ. Phys.*, 12(6):063028, 2010.

[51] B. Sanguinetti, H. O. Majeed, M. L. Jones, and B. T. H. Varcoe. Precision measurements of quantum defects in the $nP_{3/2}$ Rydberg states of ^{85}Rb. *Journ. Phys. B*, 42(16):165004, 2009.

[52] J. Yata, M. Hori, H. Kawakatsu, and T. Minamiyama. Measurements of the refractive index of alternative refrigerants. *Intern. Journ. Thermophys.*, 17(1):65–74, 1996.

[53] S. E. Anderson. *Trapping Rydberg Atoms in Ponderomotive Optical Lattices*. University of Michigan, 2014.

[54] J. J. Sakurai. *Advanced Quantum Mechanics*. Addison-Weseley Publishing Company. Reading, Massachusetts, 1967.

[55] M. Mack, F. Karlewski, H. Hattermann, S. Höckh, F. Jessen, D. Cano, and J. Fortágh. Measurement of absolute transition frequencies of ^{87}Rb of nS and nD Rydberg states by means of electromagnetically induced transparency. *Phys. Rev. A*, 83:052515, 2011.

[56] C. F. Roos, M. Chwalla, K. Kim, M. Riebe, and R. Blatt. Designer atoms for quantum metrology. *Nature*, 443(7109):316–319, 2006.

[57] D. Paredes-Barato and C. S. Adams. All-optical quantum information processing using Rydberg gates. *Phys. Rev. Lett.*, 112(4):040501, 2014.

[58] H. Weimer, M. Müller, I. Lesanovsky, P. Zoller, and H. P. Büchler. A Rydberg quantum simulator. *Nat. Phys.*, 6(5):382–388, 2010.

[59] R. Lutwak, J. Holley, P. P. Chang, S. Paine, D. Kleppner, and T. Ducas. Circular states of atomic hydrogen. *Phys. Rev. A*, 56:1443–1452, 1997.

[60] B. J. Bloom, T. L. Nicholson, J. R. Williams, S. L. Campbell, M. Bishof, X. Zhang, W. Zhang, S. L. Bromley, and J. Ye. An optical lattice clock with accuracy and stability at the 10^{-18} level. *Nature*, 506(7486):71–75, 2014.

[61] C. W. Chou, D. B. Hume, T. Rosenband, and D. J. Wineland. Optical clocks and relativity. *Science*, 329(5999):1630–1633, 2010.

[62] K. R. Moore, S. E. Anderson, and G. Raithel. Forbidden atomic transitions driven by an intensity-modulated laser trap. *Nat. Comm.*, 6, 2015.

[63] Z. T. Lu, K. L. Corwin, M. J. Renn, M. H. Anderson, E. A. Cornell, and C. E. Wieman. Low-velocity intense source of atoms from a magneto-optical trap. *Phys. Rev. Lett.*, 77(16):3331, 1996.

[64] N. Thaicharoen, A. Schwarzkopf, and G. Raithel. Measurement of the Van der Waals interaction by atom-trajectory imaging. *Phys. Rev. A*, 92(4):040701, 2015.

[65] W. Li, I. Mourachko, M. W. Noel, and T. F. Gallagher. Millimeter-wave spectroscopy of cold Rb Rydberg atoms in a magneto-optical trap: Quantum defects of the nS, nP, and nD series. *Phys. Rev. A*, 67(5):052502, 2003.

[66] P. Nussenzveig, F. Bernardot, M. Brune, J. Hare, J. M. Raimond, S. Haroche, and W. Gawlik. Preparation of high-principal-quantum-number circular states of Rb. *Phys. Rev. A*, 48(5):3991, 1993.

[67] J. W. Farley and W. H. Wing. Accurate calculation of dynamic Stark shifts and depopulation rates of Rydberg energy levels induced by blackbody radiation in hydrogen, helium, and alkali-metal atoms. *Phys. Rev. A*, 23(5):2397, 1981.

[68] G. Raithel and V. Malinovsky. High-precision microwave spectroscopy of long-lived circular-state Rydberg atoms in microgravity. Grant proposal accepted under NASA NNH13ZTT002N: "Research Opportunities in Fundamental Physics", 2013. Copy received via private communication.

[69] B. J. Knuffman. *Rydberg Atoms in Ponderomotive Potentials*. University of Michigan, 2009.